

Pedro Monroy Pérez



Universitat
de les Illes Balears

DOCTORAL THESIS
2019

LAGRANGIAN STUDIES OF
SEDIMENTATION AND TRANSPORT.
IMPACT ON MARINE ECOSYSTEMS.

b



Universitat
de les Illes Balears

DOCTORAL THESIS
2019

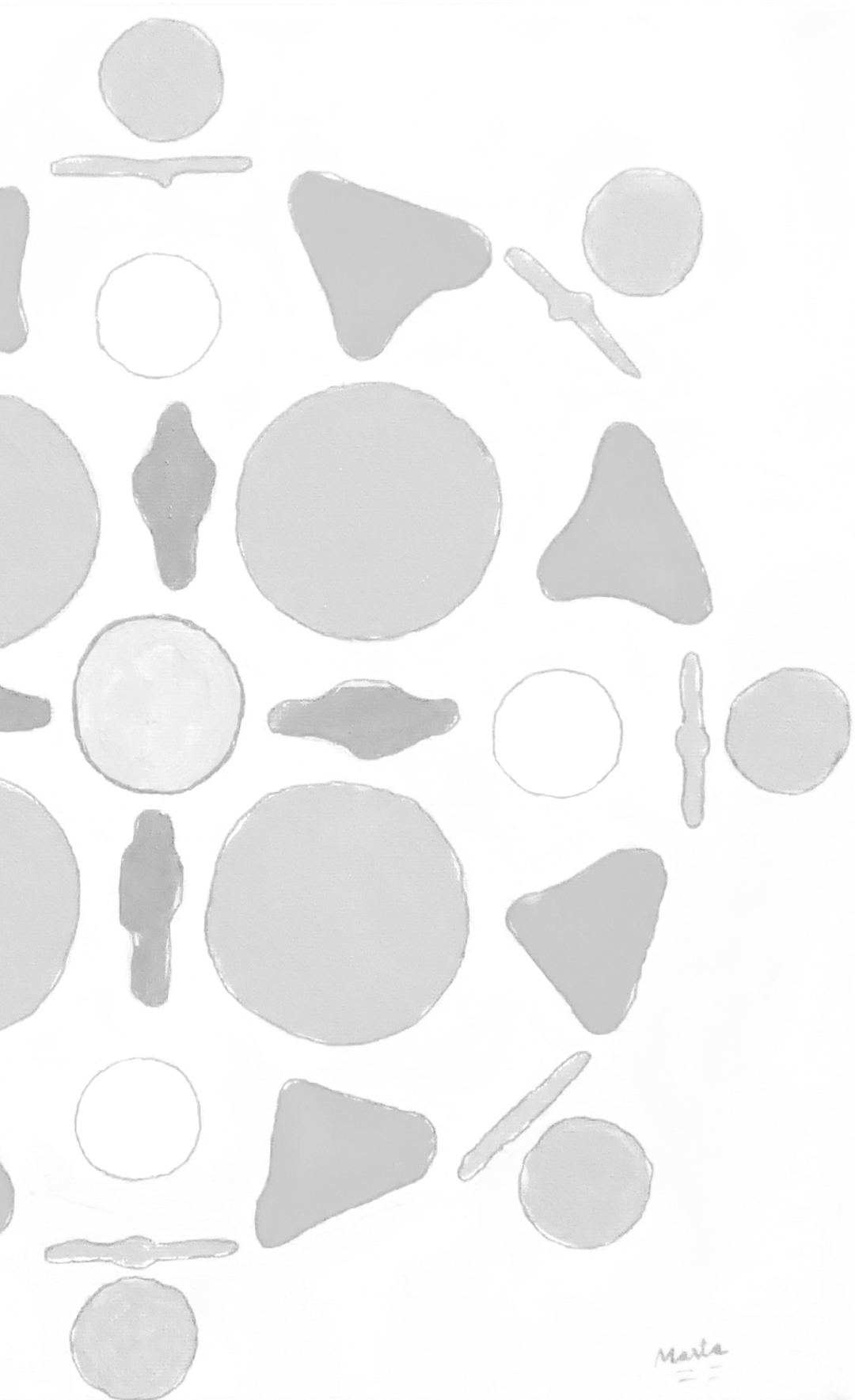
Doctoral Programme of Physics RD99/2011

**LAGRANGIAN STUDIES OF SEDIMENTATION AND
TRANSPORT. IMPACT ON MARINE ECOSYSTEMS.**

Pedro Monroy Pérez

Thesis Supervisors: Emilio Hernández-García and

Cristóbal López Sánchez



Marta

Tesis doctoral presentada por Pedro Monroy Pérez para optar al título de Doctor, en el Programa de Física de la Universitat de les Illes Balears, realizada en el Instituto de Física Interdisciplinar y Sistemas Complejos (IFISC, CSIC-Universitat de les Illes Balears) bajo la dirección de Cristóbal López y Emilio Hernández García.

Con el visto bueno de los directores de tesis.



Dr. Cristóbal López Sánchez



Dr. Emilio Hernández-García

Palma de Mallorca, 5 Junio, 2019



Doctorando Pedro Monroy Pérez

Abstract

In the last decades there has been an increasing availability of ocean velocity data from satellite measurements, drifters and computer models that has produced important advances in the Lagrangian description of ocean transport. A variety of tools for this purpose have emerged, most of them have been borrowed from dynamical systems theory and adapted to the finite time and resolution. These techniques can be divided into two main categories. One group is focused on geometric objects and they are based on the non-asymptotic version of Lyapunov exponents. On the other hand, there is a probabilistic approach focussing on the moving fluid regions themselves, the so-called set-oriented methods. They are based on the discretization of the Perron-Frobenius operator.

Ocean biology is an area where Lagrangian processes are undoubtedly important. Although we can consider marine organisms as active particles, in the case of larvae, due to their small size, they can be considered as passive tracers. This and the fact that some species are rather territorial in their adult stage, allows to study the population connectivity computing their Lagrangian trajectories. The Lagrangian Flow Network (LFN) technique has demonstrated great effectiveness in studying the structure of marine populations which are commonly organized as discrete subpopulations. It is a modeling framework in which geographical sub-areas of the ocean are represented as nodes in a network interconnected by links representing the transport of propagules (eggs and larvae) by currents. While this approach has been already applied in different contexts, the global robustness and sensitivity of metrics derived from LFNs have not been quantitatively assessed yet. Here we assess in chapter 3 the sensitivity and robustness of four connectivity metrics derived from LFN that measure retention and exchange processes, thus providing a systematic characterization of propagule dispersal. The most relevant parameters are tested over large ranges: the density of released particles, the node size (spatial-scales of discretization), the Pelagic Larval Duration (PLD) and the modality of spawning. Our results have important implications to design properly connectivity experiments with particle-tracking models and to evaluate the reliability of their results.

Another important biological process in the ocean that can be studied by a Lagrangian approach is the downward flux of carbon-rich biogenic particles from the marine surface into the deep ocean. It is a key process of the biological carbon pump, responsible (together with the solubility and the physical carbon pumps) of much of the oceans' role in the Earth carbon cycle. The problem of sinking particles is studied (chapter 4) in a realistic oceanic flow, with major energetic structures in the mesoscale, focussing on the range of particle sizes and densities appropriate for marine biogenic particles. Our results show that the finite-size corrections are negligible compared to the most

important terms, which are passive motion with the velocity of the flow, and a constant added vertical velocity due to gravity. Nevertheless, we show that two-dimensional cuts or projections of evolving three-dimensional particle clouds display horizontal clustering.

The spatial distribution of sinking particles in the seafloor is also studied (chapter 5). This was made considering a horizontal sheet of falling particles immersed in an oceanic flow, and determining how they spatially distribute when the particles sediment on the seabed (or are collected at a layer at a given depth). This is performed from a Lagrangian viewpoint attending to the oceanic flow properties and the physical characteristics (size and density) of typical biogenic sinking particles. Two main processes determine the distribution, the stretching of the sheet caused by the flow and its projection on the surface where particles accumulate. These mechanisms are checked, besides an analysis of their relative importance to produce inhomogeneities, with numerical experiments in the Benguela region. We show that faster (heavier or larger) sinking particles distribute more homogeneously than slower ones.

Resumen

En las últimas décadas ha habido un incremento en la disponibilidad de datos oceánicos obtenidos desde medidas satelitales, *drifters* y modelos computacionales que han producido importantes avances en la descripción Lagrangiana del transporte oceánico. Diversas herramientas han surgido para este propósito, muchas de ellas prestadas de la teoría de sistemas dinámicos y adaptadas para tiempo y resolución finitas. Estas técnicas pueden ser divididas en dos grandes grupos. Un grupo está enfocado en objetos geométricos que se basan en versión no asintótica de los exponentes de Lyapunov. Por otro lado, hay una aproximación probabilística centrada en regiones del fluido en movimiento, los llamados métodos orientados a conjuntos. Estos se basan en la discretización del operador de Perron Frobenius.

La Biología marina es un área donde los procesos Lagrangianos indudablemente tienen importancia. Aunque los organismos marinos se consideran partículas activas, en el caso de larvas, debido a su pequeño tamaño, pueden ser tratadas como trazadores pasivos. Esto unido al hecho de que algunas especies son bastante territoriales en su fase adulta, permite estudiar su conectividad a nivel de población calculando sus trayectorias Lagrangianas. La técnica de *red de flujo* ha demostrado gran eficacia en el estudio de la estructura de las poblaciones marinas, las cuales están organizadas como subpoblaciones. Esta técnica es un marco de modelado donde áreas geográficas del océano son representadas como nodos en una red conectados por enlaces que representan el transporte de propágulos (huevos y larvas) por las corrientes. Aunque esta técnica ha sido empleada en diferentes contextos, la robustez y sensibilidad global de las métricas derivadas de las redes de flujo no han sido evaluadas cuantitativamente todavía. Aquí evaluamos en el capítulo 3 la sensibilidad y robustez de cuatro métricas derivadas de la red flujo que miden procesos de retención e intercambio, las cuales aportan una caracterización sistemática de la dispersión de propágulos. Los parámetros más relevantes son examinados en un extenso rango de valores: densidad de partículas depositadas, duración del período larvario y la modalidad de la fase de desove. Nuestros resultados muestran importantes implicaciones a la hora de diseñar adecuadamente experimentos de conectividad usando modelos de seguimiento de partículas y para evaluar la confianza de los resultados.

Otro importante proceso biológico en el océano que puede ser estudiado mediante el enfoque Lagrangiano es el flujo descendente de partículas biogénicas marinas ricas en carbono desde la superficie marina hasta el fondo marino. Este es un proceso clave de la bomba biológica de carbono, principal causante (junto a la bomba de solubilidad y bombeo físico del carbono) del papel que desempeña el océano en el ciclo global del carbono. Se estudia el problema del hundimiento de partículas (capítulo 4) en un flujo realista del océano, cuyas estructuras más energéticas se encuentran en la mesoscala,

centrándonos en el intervalos de tamaños y densidades de las partículas apropiados para las partículas biogénicas marinas. Nuestros resultados muestran que las correcciones debidas a tamaño finito son despreciables comparadas con los términos más importantes, que son el transporte pasivo por la corriente y la velocidad constante vertical debida a la gravedad. Sin embargo, demostramos que cortes bidimensionales o proyecciones de la nube de partículas tridimensional muestran inhomogeneidades horizontales.

La distribución espacial de partículas que sedimentan es también estudiada (capítulo 5). Esto fue llevado a cabo considerando una lámina horizontal de partículas descendentes sujetas al flujo oceánico, y determinando cómo se distribuyen espacialmente cuando sedimentan en el fondo oceánico (o cuando son recogidas a una determinada profundidad). Esto se desarrolla desde una perspectiva oceánica centrándonos en las propiedades del flujo oceánico y las propiedades físicas (tamaño y densidad) de las típicas partículas biogénicas en hundimiento. Principalmente los procesos determinan la distribución, la elongación de la lámina causada por el flujo y su proyección en la superficie donde se acumulan las partículas. Estos mecanismos son examinados, aparte del análisis de su relativa importancia para producir inhomogeneidades, con experimentos numéricos en la región de Benguela. Mostramos que las partículas que descienden más rápido (pesadas o grandes) se distribuyen más homogéneamente que las lentas.

Resum

En les últimes dècades hi ha hagut un increment en la disponibilitat de dades oceàniques obtingudes a partir de mesures de satèl·lit, *drifters* i models computacionals que han produït importants avenços en la descripció Lagrangiana del transport oceànic. Diverses eines han sorgit per aquest propòsit, moltes d'elles prestades de la teoria de sistemes dinàmics i adaptades per a temps i resolució finites. Aquestes tècniques poden ser dividides en dos grans grups. Un grup està enfocat en objectes geomètrics que es basen en la versió no asimptòtica dels exponents de Lyapunov. D'altra banda, hi ha una aproximació probabilística centrada en regions del fluid en moviment, els anomenats mètodes orientats a conjunts. Aquests es basen en la discretització de l'operador de Perron Frobenius.

La Biologia marina és una àrea on els processos Lagrangians indubtablement tenen importància. Tot i que els organismes marins es consideren partícules actives, en el cas de larves, per la seva mida petita, poden ser tractades com a traçadors passius. Això unit al fet que algunes espècies són bastant territorials en la seva fase adulta, permet estudiar la seva connectivitat poblacional calculant les seves trajectòries Lagrangianes. La tècnica de *xarxa de flux* ha demostrat gran eficàcia en l'estudi de l'estructura de les poblacions marines, les quals estan organitzades com subpoblacions. Aquesta tècnica és un marc de modelatge on àrees geogràfiques de l'oceà són representades com a nodes en una xarxa connectats per enllaços que representen el transport de propàguls (ous i larves) per les corrents. Tot i que aquesta tècnica ha estat emprada en diferents contextos, la robustesa i sensibilitat global de mesures derivades de les xarxes de flux no han estat avaluades quantitativament encara. Aquí avaluem en el capítol 3 la sensibilitat i robustesa de quatre mesures derivades de la xarxa flux que mesuren processos de retenció i intercanvi, les quals aporten una caracterització sistemàtica de la dispersió de propàguls. Els paràmetres més rellevants són examinats en un extens rang de valors: densitat de partícules dipositades, durada del període larvari i la modalitat de la fase de fresa. Els nostres resultats mostren importants implicacions a l'hora de dissenyar adequadament experiments de connectivitat usant models de seguiment de partícules i per avaluar la confiança dels resultats.

Un altre procés biològic important en l'oceà que pot ser estudiat mitjançant l'enfocament Lagrangianà és el flux descendent de partícules biogèniques marines riques en carboni des de les superfícies marines fins al fons marí. Aquest és un procés clau de la bomba biològica de carboni, principal causant (al costat de la bomba de solubilitat i el bombeig físic del carboni) del paper que exerceix l'oceà en el cicle global del carboni. S'estudia el problema de l'enfonsament de partícules (capítol 4) en un flux realista de l'oceà, les estructures més energètiques del qual es troben en la mesoscala, centrant-nos en inter-

vals de grandàries i densitats de les partícules apropiats per a les partícules biogèniques marines. Els nostres resultats mostren que les correccions degudes a grandària finita són menyspreables comparades amb els termes més importants, que són el transport passiu pel corrent i la velocitat constant vertical deguda a la gravetat. No obstant això, vam demostrar que talls bidimensionals o projeccions del núvol de partícules tridimensional mostren inhomogeneïtats horitzontals.

La distribució espacial de partícules enfonsades és també estudiada (capítol 5). Això va ser dut a terme considerant una làmina horitzontal de partícules descendents subjectes al flux oceànic, i determinant com es distribueixen espacialment quan sedimenten en el fons oceànic (o quan són recollides a una determinada profunditat). Això es desenvolupa des d'una perspectiva oceànica centrant-nos en les propietats del flux oceànic i les propietats físiques (grandària i densitat) de les típiques partícules biogèniques que sedimenten. Principalment dos processos determinen la distribució, l'elongació de la làmina causada pel flux i la seva projecció en la superfície on s'acumulen les partícules. Aquests mecanismes són examinats, a part de l'anàlisi de la seva relativa importància per a produir inhomogeneïtats, amb experiments numèrics a la regió de Benguela. Vam mostrar que les partícules que descendeixen més ràpid (pesades o grans) es distribueixen més homogèniament que les lentes.

P. Monroy list of publications

- V. Rossi, M. Dubois, E. Ser-Giacomi, P. Monroy, E. Hernández-García and C. López. "*Lagrangian Flow Network: a new tool to evaluate connectivity and understand the structural complexity of marine populations*". In: *CIESM Workshop Monograph 48: Marine connectivity - migration and larval dispersal*, edited by F. Briand, CIESM Publisher, Monaco, 39-51 (2016)
- R. Cuerno, R. Gallardo Caballero, A. Gordillo-Guerrero, P. Monroy and J. J. Ruiz-Lorenzo. "*Universal behavior of crystalline membranes: Crumpling transition and Poisson ratio of the flat phase*". *Phys. Rev. E* 93(2016), p. 022111.
- P. Monroy, V. Rossi, E. Ser-Giacomi, E. Hernández-García and C. López. "*Sensitivity and robustness of larval connectivity diagnostics obtained from Lagrangian Flow Networks*". *ICES Journal of Marine Science* 74.6 (2017), pp. 1763–1779.
- P. Monroy, E. Hernández-García, V. Rossi and C. López. "*Modeling the dynamical sinking of biogenic particles in oceanic flow*". *Nonlin. Processes Geophys.* 24 (2017), pp. 293–305.
- G. Drótos, P. Monroy, E. Hernández-García and C. López. "*Inhomogeneities and caustics in passive particle sedimentation in incompressible flows*". *Chaos* 29.1 (2019), 013115 (1–25).
- P. Monroy, G. Drótos, E. Hernández-García and C. López. "*Spatial inhomogeneities in the sedimentation of biogenic particles in ocean flows: analysis in the Benguela region*". To appear in *Journal of Geophysical Research - Oceans* (2019).
- M. Hidalgo, V. Rossi, P. Monroy, E. Ser-Giacomi, E. Hernández-García, B. Guisjarro, E. Massutí, F. Alemany, A. Jadaud, J. L. Pérez and P. Reglero. "*Accounting for ocean connectivity and hydroclimate in fish recruitment fluctuations within transboundary metapopulations*". To appear in *Ecological Applications* (2019).

Contents

	i
Abstract	iii
Resumen	v
Resum	vii
P. Monroy list of publications	ix
Contents	xi
1 Introduction	1
1.1 Plan of the thesis	1
1.2 Oceanic fluid motion	1
1.3 Ocean Modelling	9
1.4 Coastal Upwelling	11
1.5 Biological carbon pump	12
1.6 Dynamical systems approach to transport in ocean flows	14
1.7 Dynamics of finite size tracers	19
2 Lagrangian Flow Networks to study the multi-scale connectivity of marine populations	25
2.1 Introduction	26
2.2 Metapopulations and subpopulations in marine seascapes	26
2.3 Lagrangian Flow networks applied to larval dispersal	28
2.4 Local network measures as proxies of larval connectivity	30
2.5 Case study: connectivity within the metapopulation of a harvested species	31
3 Sensitivity and robustness of larval connectivity diagnostics obtained from Lagrangian Flow Networks	37
3.1 Introduction	37
3.2 Data and methods	39
3.3 Numerical parameters	42
3.4 Biological parameters	49
3.5 Other factors not considered	58
4 Modeling the dynamical sinking of biogenic particles in oceanic flow	61

4.1	Introduction	61
4.2	Characteristics of marine biogenic particles	63
4.3	Equations of motion for small spherical rigid particles	66
4.4	Numerical simulations	69
4.5	Geometric clustering of particles	74
5	Inhomogeneities of sinking particles in ocean flows	79
5.1	Introduction	79
5.2	Data and methods	81
5.3	Numerical results	89
5.4	Discussion	93
6	Conclusions	99
A	Coriolis Theorem and acceleration in non-inertial frames	103
B	Velocity and acceleration in spherical coordinates	105
C	Density factor, geometrical approach	109
C.1	Stretching factor	109
C.2	Numerical computation of the geometrical density factor	111
C.3	Coarse-graining of the geometrical density factor	113
	Bibliography	115

CHAPTER 1

Introduction

1.1 Plan of the thesis

In the remaining of this Chapter 1 we introduce general notions and concepts of dynamical systems theory, geophysical fluids and marine biology that form the theoretical basis of this work. Chapter 2 is devoted to the introduction of the concept of flow networks in geophysical flows applied to the study of larvae connectivity in the Mediterranean Sea. After describing the method, we focus on study the robustness and sensitivity of four LFN-derived connectivity metrics measuring retention and exchange. In chapter 3 we address the problem of sinking particles in a realistic oceanic flow, with major energetic structures in the mesoscale, focussing in the range of particle sizes and densities appropriate for marine biogenic particles. The chapter 4 focusses on the role of the transport processes, in particular on how a homogeneous layer of particles stretches and folds due to the oceanic currents while it is sinking, to finally form inhomogeneous and clustering when they are trapped. Finally In chapter 5 we draw general conclusions.

1.2 Oceanic fluid motion

The basic concepts and fundamental laws describing oceanic fluid flows are revised in this section. To describe the fluid dynamics applying Newton's second law to every constitutive molecule is practically impossible due to the high number of molecules in fluids (even in a small fluid volume). However, the length of smallest eddies η fall in millimeter scale and molecular free path in water λ is about $2.5 \times 10^{-10} m$ [118]. Therefore the length scale over which ocean flows change are much larger than the length scale of molecular motions. This justifies the application of the continuum approximation. Fluid dynamics is described by macroscopic fluid magnitudes which represent averages over sufficiently small volumes. The fundamental equation for the *averaged* fluid velocity $\mathbf{u}(\mathbf{r}, t)$ resulting from the conservation of momentum in a infinitesimal fluid volume is

$$\rho \frac{d\mathbf{u}}{dt} = \mathcal{F}_{ext} + \nabla \cdot \boldsymbol{\sigma}, \quad (1.1)$$

where ρ corresponds to the fluid density and $\frac{d\mathbf{u}}{dt}$ is the acceleration of an infinitesimal fluid particle (or equivalently fluid parcel) caused by the external forces \mathcal{F}_{ext} and the interacting forces between fluid elements expressed as the divergence of a stress tensor $\boldsymbol{\sigma}$.

The derivative $\frac{d\mathbf{u}}{dt}$ is called material or Lagrangian derivative. It can be related to *Eulerian* derivatives, taken at fixed position and time, differentiating $\mathbf{u}(\mathbf{r}(t), t)$ along the fluid trajectory $\mathbf{r}(t)$

$$\frac{d\mathbf{u}}{dt} = \frac{\partial\mathbf{u}}{\partial t} + (\mathbf{u} \cdot \nabla)\mathbf{u}. \quad (1.2)$$

The stress tensor $\boldsymbol{\sigma}$ can be expressed as the sum of an isotropic diagonal part described by a scalar pressure P and the remainder component or shear stress $\boldsymbol{\tau}$. Kinetic theory[153] allows to find for an incompressible fluid $\nabla \cdot \mathbf{u} = 0$ a linear relation between the shear stress $\boldsymbol{\tau}$ and the first derivatives $\frac{\partial u_i}{\partial x_j}$

$$\sigma_{ij} = -P\delta_{ij} + \mu \left(\frac{\partial u_i}{\partial x_j} + \frac{\partial u_j}{\partial x_i} \right) \quad \text{with} \quad \nabla \cdot \mathbf{u} = 0 \quad (\text{Incompressible fluid}), \quad (1.3)$$

where μ is the dynamic viscosity and can be estimated by molecular properties. Most fluids, concretely the seawater, are not compressed much in a flow because the typical flow velocity is much smaller than the speed of sound in the medium[178].

Substituting equation (1.3) in (1.1), we obtain the Navier-Stokes equations

$$\rho \left(\frac{\partial\mathbf{u}}{\partial t} + (\mathbf{u} \cdot \nabla)\mathbf{u} \right) = \mathcal{F}_{ext} - \nabla P + \mu \nabla^2 \mathbf{u}, \quad (1.4)$$

where we have used the equation (1.2). The momentum equations (1.4) together with the additional constraint of incompressibility $\nabla \cdot \mathbf{u} = 0$ fully define the motion of an incompressible fluid.

1.2.1 Turbulent flow

The oceans are forced by tides, storms, and differential heating and cooling at scales of many hundreds of kilometers. This is represented in the Navier-Stokes equations (1.4) by the forcing term \mathcal{F}_{ext} which inputs energy on the fluid at length scale L . However, the ocean does not continue increasing its kinetic energy infinitely. The only way to be dissipated is through the viscous term $\mu \nabla^2 \mathbf{u}$ because the inertial $(\mathbf{u} \cdot \nabla)\mathbf{u}$ and pressure ∇P terms are only able to redistribute the energy among the different scales. And energy dissipation occurs at length scale $\eta \ll L$ where viscosity becomes important.

The relative contribution of inertia (the tendency for a fluid or any body to continue moving) and dissipation can be estimated by the ratio of the terms representing inertia and viscosity dissipation

$$Re = \frac{\rho U(U/L)}{\mu U/L^2} = \frac{UL}{\nu}. \quad (1.5)$$

Re is called Reynolds Number [143] and U is taken as the characteristic fluid velocity, L is the length scale over which the motion is organized and $\nu = \mu/\rho$ is the kinematic viscosity of the fluid ($\nu \sim 10^{-6} m^2/s$ for seawater). The Reynolds number plays an

important role on flow properties. Indeed, defining the dimensionless variables

$$\mathbf{u}^* = \frac{\mathbf{u}}{U}, \quad \mathbf{r}^* = \frac{\mathbf{r}}{L}, \quad t^* = \frac{Ut}{L}, \quad (1.6)$$

$$\mathcal{F}_{ext}^* = \frac{\mathcal{F}_{ext}L}{U}, \quad P^* = \frac{P}{\rho U^2}, \quad (1.7)$$

we obtain the dimensionless Navier Stokes equations

$$\frac{\partial \mathbf{u}^*}{\partial t^*} + (\mathbf{u}^* \cdot \nabla^*) \mathbf{u}^* = \mathcal{F}_{ext}^* - \nabla^* P^* + \frac{1}{Re} \nabla^{*2} \mathbf{u}^*. \quad (1.8)$$

Eq. (1.8) reveals that the only control parameter is the Reynolds number. When Re is small, the flow is dominated by viscosity where any induced perturbation is rapidly dissipated producing a smooth and laminar flow. For $Re \gg 1$, inertia dominates and the flow is turbulent with irregular and complex structure. The ocean velocity at $100km$ is of the order of $1m/s$ (e.g. a tidal current or the speed of the Gulf stream). Thus, at this scale Re is huge, 10^8 or higher; the ocean at this scale is turbulent.

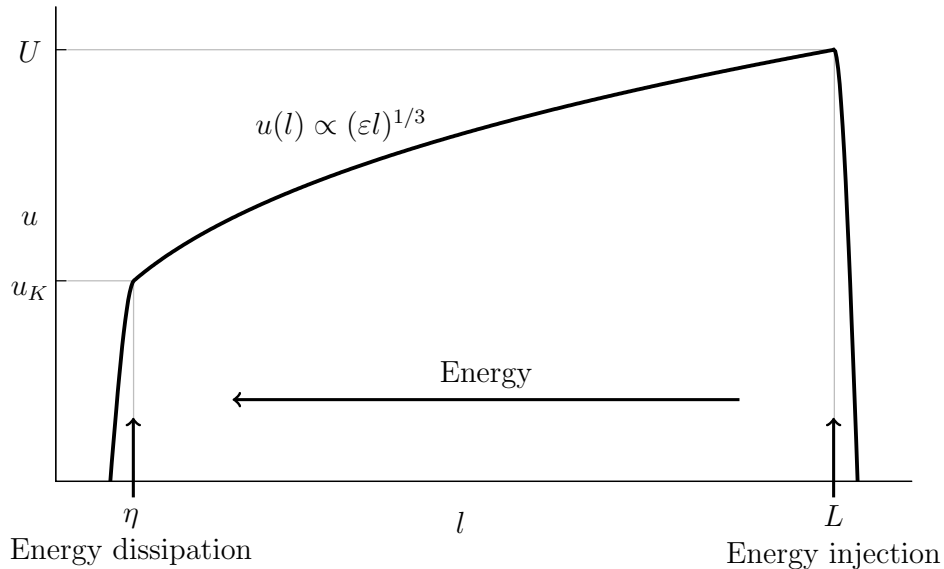


Figure 1.1: Velocity spectrum of turbulence: u versus eddie size. The inertial subrange are delimited by the dissipation length scale η and the length scale of energy injection L . The direction of energy is indicated by arrows.

One could be tempted to approximate Navier Stokes equations for high Re neglecting the dissipative term, obtaining the so-called Euler equation. However, a statistically stationary state is always reached where energy dissipation balances its injection by the external forces. This means that the rate of energy dissipation by viscosity ε is always non zero even for $Re \rightarrow \infty$ and Navier-Stokes equations at $Re \gg 1$ are different from Euler equations (with $\mu = 0$). This fact and the broad difference among the length

scales of input and dissipation of energy at $Re \gg 1$ suggest the turbulent cascade of energy [145]. In this description, the forcing produces large scale eddies (i.e. coherent structures of the fluid flow correlated over a distance L), which become unstable due to the inertial term and break in smaller and smaller eddies. This eddy breaking process generates a cascade of kinetic energy from large scales where they are injected (by wind driven currents, tides or waves) to the small scale η where they are dissipated at rate ε by the fluid viscosity.

The range of scales $\eta \ll l \ll L$ is called the inertial range because it is controlled by the inertial terms and neither injection nor dissipation play any role. Hence, at the inertial range the only relevant quantity is the dissipation rate ε which is equal to the rate at which energy is transferred from large eddies to smaller ones [83, 84]. Therefore, the statistical properties of the velocity field should only depend on ε and the length scale l . The characteristic time scale of an eddy of size l and kinetic energy $u(l)^2$, is $\tau_l \simeq l/u(l)$. Considering that eddies lose their kinetic energy to smaller ones in this time τ_l , the energy dissipation rate ε can be estimated as $\varepsilon \simeq u(l)^3/l$ and we found the following scaling law[27]

$$\delta u(l) \sim (\varepsilon l)^{1/3} \sim U(l/L)^{1/3}. \quad (1.9)$$

Assuming that the scaling (1.9) is still satisfied at the dissipative length scale η and setting to order unity the "local Reynolds numbers" $\frac{\eta u(\eta)}{\varepsilon} = \mathcal{O}(1)$, we can estimate how η changes with Re

$$\eta \sim LRe^{-3/4}. \quad (1.10)$$

This is termed the Kolmogorov length scale, and is generally taken as the lower limit of the inertial range. The expression (1.10) shows also that Re is directly related to the ratio of the largest to smallest scales in the flow. Other relevant quantities at the dissipative scale are the Kolmogorov time scale $\tau_K = \varepsilon^{-1/3}\eta^{2/3}$ and velocity scale $u_K = u_\eta = (\nu^2/\varepsilon)^{1/3}$. Taking the typical scales of the mesoscale ocean eddies $U = 0.1m/s$ and $L = 100km$ [28] we obtain that $\eta \sim 1mm$ and $\tau_k \sim 10s$ which are not far away from the observed values in the ocean [81].

1.2.2 Geophysical Flow equations

The fluid equations necessary for understanding large-scale ocean motions corresponds to a modified version of the previous fundamental equations (1.4). First, we have to include the gravity force \mathbf{g} and also they have to be adapted to the spherical shape and rotation of the Earth. To do this it is only needed to transform the accelerations terms in equation (1.4) to the rotating spherical coordinates (see appendix A and B), resulting in

$$\rho \left(\frac{\partial \mathbf{u}}{\partial t} + \overbrace{(\mathbf{u} \cdot \nabla) \mathbf{u}}^{\text{Advection}} + \overbrace{\mathbf{\Gamma} \times \mathbf{u}}^{\text{Curvature}} + \overbrace{2\mathbf{\Omega} \times \mathbf{u}}^{\text{Coriolis}} + \overbrace{\mathbf{\Omega} \times (\mathbf{\Omega} \times \mathbf{r})}^{\text{Centrifugal}} \right) = \quad (1.11)$$

$$- \overbrace{\nabla P}^{\text{Pressure}} + \overbrace{\rho \mathbf{g}}^{\text{Gravity}} + \overbrace{\mu \nabla^2 \mathbf{u}}^{\text{Dissipation}} .$$

Where $\Omega = 7.2921 \cdot 10^{-5} s^{-1}$ corresponds to the earth's angular frequency and $\mathbf{\Gamma}$ is the angular velocity of the spherical vector basis (see appendix B for details). The effect of rotation adds the Coriolis and centrifugal forces. The spherical shape induces the curvilinear terms. In principle, incorporating gravitational and other terms makes more difficult to study of ocean flows than simple fluids. However, all the new forces (gravity, Coriolis force, ...) tend to organize and shape the turbulence, promoting eddies of a particular structure and size at the expense of others. Also, the particular scales of the ocean allows to simplify the equations. The traditional approximations and assumptions commonly used in geophysical fluid dynamics are:

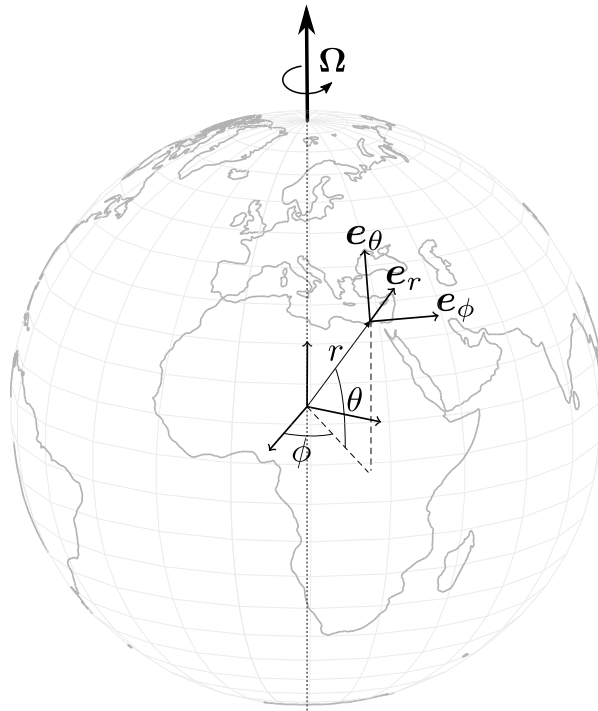


Figure 1.2: Local Cartesian coordinate system with the origin situated at a specific point on the earth's surface. The Cartesian coordinates (x, y, z) are defined by the direction of the vector basis (e_θ, e_ϕ, e_r) . The coordinates θ and ϕ are the latitude and longitude respectively.

- The centrifugal terms are usually combined with gravity by defining the apparent gravity \mathbf{g}^* such that

$$\mathbf{g}^* = \mathbf{g} - \Omega \times (\Omega \times \mathbf{r}). \quad (1.12)$$

The direction of effective gravity will in general have a component in the horizontal plane, that is the plane perpendicular to the radial direction. However the Earth has oblateness to compensate the centrifugal force, so that the effective gravity acts in a direction virtually normal to the earth's surface. Therefore, we use

the direction of effective gravity to define the vertical direction, and then for all purposes we regard the Earth as if it was a true sphere (the oblateness is very small) and we only have to modify the magnitude of \mathbf{g} due to the centripetal force. In order to simplify notation we will omit the star on effective gravity.

- Usually, we are interested on length scales substantially shorter than the global scale. This allows to neglect the curvature terms in (1.11) and the use of local Cartesian coordinates (x, y, z) where the origin is shifted to a position on the earth's surface. The directions of the local Cartesian coordinates correspond to the spherical $(\mathbf{e}_\phi, \mathbf{e}_\theta, \mathbf{e}_r)$ at its origin as depicted in figure 1.2. The vertical direction coincides with apparent gravity direction and transforms accordingly to $z = r - R$, where R is the earth's radius.
- We consider a density profile ρ_H in hydrostatic balance with a reference pressure P_H

$$\nabla P_H = \rho_H \mathbf{g}, \quad (1.13)$$

that is, the pressure at any point is equal to the weight of a unit cross-section water column above that point. The equation (1.11) can be rewritten in terms of the perturbed density $\rho' = \rho - \rho_H$ and pressure $P' = P - P_H$. Due to density variations in the ocean ρ' is small compared with the background reference profile, it is possible to employ *Boussinesq* approximation neglecting density differences except when combined with gravity (e.g. in the calculation of weight). At this point, since the original variables ρ and P no longer appear in the equations, it is customary to drop the primes from ρ' and P' without risk of ambiguity.

- Navier-Stokes equations are applied to fields in which only the molecular fluctuations have been removed by averaging. But another averaging is necessary in order to filter out the rapid fluctuations produced by small-scale eddies. First, we assume that the velocity and pressure are composed of time-averaged (denoted by a bar) and a fluctuation components (primed)

$$\mathbf{u} = \bar{\mathbf{u}} + \mathbf{u}', \quad (1.14)$$

$$P = \bar{P} + P'. \quad (1.15)$$

The mean values are taken over a long enough time to ensure that the mean fluctuation values satisfy $\overline{\mathbf{u}'} = \overline{P'} = 0$. Substituting in the Navier Stokes equations and averaging over an interval of time long enough, we obtain the representative field variables of the large-scale flow. The fluctuations disappear from all linear terms except for a contribution to the dynamics of the mean flow through the non linear term [144]

$$\nabla \cdot \boldsymbol{\sigma}', \quad \text{with} \quad \sigma'_{ij} = \overline{u'_i u'_j}. \quad (1.16)$$

This term is called Reynolds stress [144]. It represents the net transfer of momentum by turbulent eddies. It is possible to derive an equation for $\overline{u'_i u'_j}$. However

the resulting equation will have terms like $\overline{u'_i u'_j u'_k}$ and so on. The traditional approach to this closure problem is to assume that turbulent eddies act in a manner analogous to molecular diffusion so that it is possible to assume

$$\frac{1}{\rho} \nabla \cdot \boldsymbol{\sigma}' = \nu_E \nabla^2 \bar{\mathbf{u}}, \quad (1.17)$$

where ν_E is the eddy viscosity and, unlike molecular dynamic viscosity ν , depends on the flow instead of the physical properties of the fluid and must be determined empirically for each situation. Additionally eddy viscosities depend on the direction. Ocean flows are different in the horizontal and vertical directions because, among other reasons, Coriolis force tends to organize and shape the fluid motion promoting columnar eddies along the vertical direction. Hence, at least eddy viscosities must be spitted in horizontal and vertical coefficients

$$\frac{1}{\rho} \nabla \cdot \boldsymbol{\sigma}' \simeq \nu_h \left(\frac{\partial^2 \mathbf{u}}{\partial x^2} + \frac{\partial^2 \mathbf{u}}{\partial y^2} \right) + \nu_z \frac{\partial^2 \mathbf{u}}{\partial z^2} \quad (1.18)$$

where ν_h and ν_z are the horizontal and the vertical eddy viscosity coefficients, respectively.

- The vertical velocities in the ocean are considerably smaller than horizontal ones (see Section 1.2.3). It allows to neglect the vertical component of Coriolis force in the Navier-Stokes equation.

After applying the above approximations and assumptions, (1.11) transforms into the following set of equations

$$\frac{du}{dt} - fv = -\frac{1}{\rho_0} \frac{\partial P}{\partial x} + \nu_h \left(\frac{\partial^2 u}{\partial x^2} + \frac{\partial^2 u}{\partial y^2} \right) + \nu_z \frac{\partial^2 u}{\partial z^2}, \quad (1.19)$$

$$\frac{dv}{dt} + fu = -\frac{1}{\rho_0} \frac{\partial P}{\partial y} + \nu_h \left(\frac{\partial^2 v}{\partial x^2} + \frac{\partial^2 v}{\partial y^2} \right) + \nu_z \frac{\partial^2 v}{\partial z^2}, \quad (1.20)$$

$$0 = -\frac{\partial P}{\partial z} - \rho g, \quad (1.21)$$

These equations correspond to the primitive equations in local Cartesian coordinates and they are the starting point of most of ocean studies. The factor $f = \Omega \sin \theta$ is the Coriolis frequency and ρ_0 is a reference constant density of the dynamic density ρ and $(u, v, w) = \mathbf{u}$ are the Cartesian components for the velocity field.

1.2.3 Influence of rotation and stratification on ocean motion scales

Vertical ocean motions are practically in hydrostatic balance where the gravitational force balances pressure forces. In the horizontal motions a similar nearly balanced situation exists. The ratio of the relative acceleration to the Coriolis acceleration is measured

by the Rossby number

$$Ro = \frac{U}{f_0 L}. \quad (1.22)$$

Large scale ocean flows are characterized by small Rossby number. This means that they are in geostrophic balance where Coriolis and the pressure forces are practically in equilibrium [146]. Assuming homogenous density and in the absence of strong pressure variations above the fluid surface, the dynamic pressure is given by $P = \rho_0 g h$, where h is the height of the sea surface (SSH) above a level surface. At the geostrophic balance the horizontal primitive equations (1.19) can be related to horizontal differences in surface height h :

$$u = -\frac{g}{f} \frac{\partial h}{\partial x}, \quad (1.23)$$

$$v = \frac{g}{f} \frac{\partial h}{\partial y}. \quad (1.24)$$

The geostrophic currents are driven by horizontal differences on dynamic pressure which can be inferred from the SSH data obtained by altimetry satellites.

The geostrophic approximation and the hydrostatic balance implies that large-scale ocean flows are nearly two dimensional, where variations along the eddy rotation axis are inhibited. This is justified by the Taylor-Proudman theorem [90]. Hence, small values for the vertical velocity are expected. Computing the vertical component of vorticity $\nabla \times \mathbf{v}$ from (1.19) we find that the typical vertical velocity is given by

$$W = Ro \frac{H}{L} U. \quad (1.25)$$

Therefore, vertical velocities can be ignored in flows with sufficiently small Rossby number and scale factor H/L . However, there are serious restrictions in applying equation (1.25) to the real ocean. The reason is that ocean density has been assumed homogenous in the vertical direction. Actually, vertical variations of the ocean density is one of the key factors in oceanographic flows and cannot be easily neglected. This stratification restricts the spatial scale required for geostrophic balance to be smaller than the internal radius of deformation

$$L_d = \frac{Ro}{Fr} L, \quad (1.26)$$

where Fr is the Froude number, that evaluates the importance of stratification as Ro of rotation [178]. The combined effect of stratification and rotation modifies the expression (1.25) for the typical vertical velocity by [35]

$$W = \frac{Fr^2}{Ro} \frac{H}{L} U. \quad (1.27)$$

The ocean currents observed at length scales of the order of the deformation radius are referred by oceanographers by mesoscale. The patterns at these scales are at or near geostrophic equilibrium and can thus persist for a long time. So Ro is small and

$Fr \sim Ro$. According to Eq. (1.27) and taking into account that $H/L \ll 1$, we have that $W \ll U$ at these scales. The features of interest in such flows are typically $10 - 100\text{km}$ in horizontal, occur over depths of orders 1000m and have characteristic horizontal velocities of $0.1 - 1\text{m/s}$. The earth's rotation has a dominant influence at such scales, and the Rossby number of these flows is of the order $0.1 - 0.01$ [102]. This is the scale of eddies and frontal meander and they are in hydrostatic and geostrophic balance and the Rossby number and aspect ratio are typically $\ll 1$. But they approach to 1 for horizontal scales of a kilometer or less. This is the submesoscale with $Ro \sim Fr \sim 1$, which is intermediate to the mesoscale and the fully three-dimensional motions at small scales with $Ro, Fr > 1$ (figure 1.3).

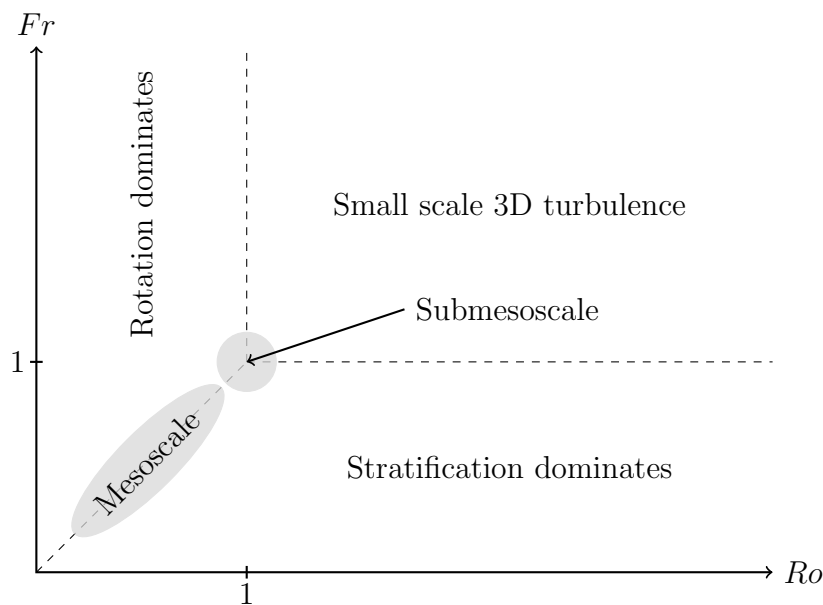


Figure 1.3: Regimes of ocean dynamics as a function of the Rossby and Froude number, which measure the effect of earth's rotation and ocean stratification, respectively.

1.3 Ocean Modelling

The equations governing geophysical fluid motions, even with the approximations made in the last section, are not solvable analytically except in rare instances and after further simplifications. Hence, numerical simulations are needed. However, trying to solve directly the equations has a expensive computational cost, particularly for high Reynolds number due to the wide range of scales involved. Therefore, different numerical approaches have been developed compromising the computational resources and precise simulation of certain scales in the problem. The main approaches are summarized below [4]:

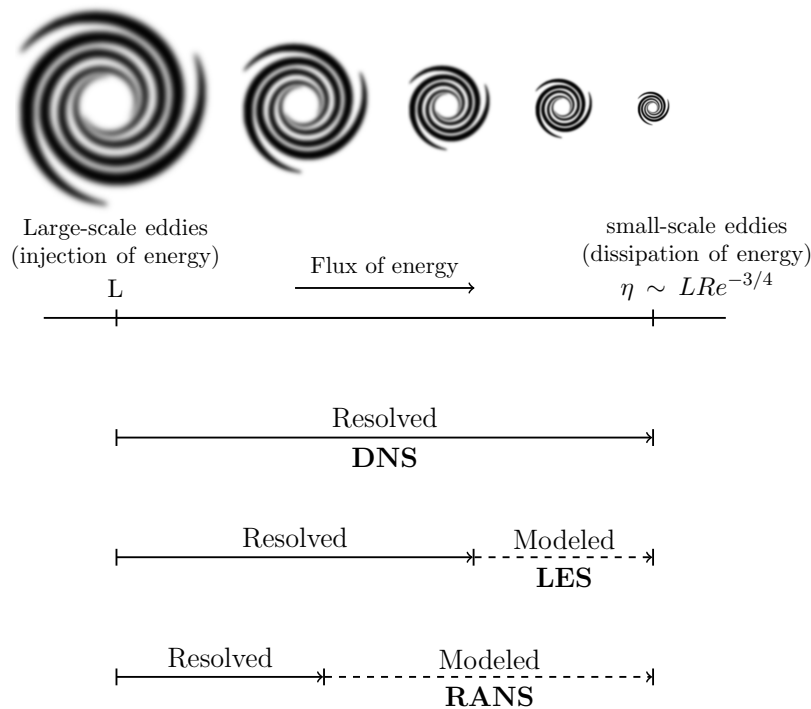


Figure 1.4: Length scale resolved in the main types of turbulence modeling strategies.

- **Direct numerical simulation (DNS):** it is the numerical solution of the full three-dimensional and time-dependent Navier–Stokes equations. The higher the Reynolds number, the finer the mesh should be. Hence, the cell size in each direction of the computational domain should decrease with $Re^{-3/4}$. DNS is indeed useful for the investigation of turbulence mechanisms and the improvement and development of turbulence closure models.
- **Large-eddy simulation (LES):** it solves a suitably filtered version of the governing equations. The small scaled filtered out are represented by subgrid-scale (SGS) stresses, which have to be modeled in terms of the resolved field. This constitutes an analogous problem as the closure problem in Reynolds averaging. It is not closed because the SGS stresses depend on the original (unfiltered) velocity field.
- **Reynolds-averaged Navier Stokes (RANS):** In this approach only the mean flow is explicitly calculated using the mean flow equations (section 1.2.2). Turbulent fluctuations are considered through the estimation of the Reynolds stress term by a variety of methods. In the most widespread of these, the Reynolds stress term is equated to a diffusive term proportional to the mean rate of strain and a turbulent viscosity.

Turbulence modeling strategies range from DNS, where all physics of spatial and temporal scales are resolved and no modeling is involved, to Reynolds averaged Navier–

Stokes (RANS) with the largest range of modeled flow scales. This model hierarchy is illustrated in figure 1.4, with the top represented by the most physics-resolving and computationally expensive approach (DNS) and the bottom by the most empirical and computationally affordable approach (RANS).

The numerical velocity used in chapter 3 for the Mediterranean sea is based on primitive equations [110], hence it is RANS approach. It is the physical reanalysis component of the Mediterranean Forecasting System, available through the Copernicus Marine Environment Monitoring Service (CMEMS). The model domain extends into the Atlantic to properly simulate the exchange of water masses at the Gibraltar Strait. The domain is nested in the Atlantic within monthly mean climatological fields that are computed from ten years of daily output from the global model, as provided by MERCATOR [41]. The horizontal eddy viscosity is constant and the vertical viscosity and diffusivities are a function of the Richardson number [125]. The reanalysis system includes a 3D variational data assimilation scheme. The assimilated data include along-track satellite sea level anomalies and in situ temperature and salinity profiles.

In chapters 4 and 5 the oceanic velocity data used are obtained from simulations of the regional ocean circulation model ROMS [162]. The ROMS model also belongs to the group of models that solve the RANS equations. The ROMS model solves the primitive equations in 3d curvilinear, terrain following grid with a free-surface [62] and additional equations for transported tracers. The Reynolds stress and turbulent fluxes at non resolved scales are parametrized in the RANS fashion with eddy viscosity and diffusivity.

1.4 Coastal Upwelling

There is an Ekman layer in the upper ocean. The Ekman layer is defined as the surface boundary layer in which the frictional force is balanced by Coriolis force. Within the Ekman layer, the wind stress is transformed downward through eddy-induced horizontal momentum flux [178]. A major uncertain part of the Ekman layer theory is the vertical eddy viscosity ν_z . The classical theory of Ekman layer assumes that ν_z is isotropic and has a constant value over the whole depth of the layer. Under such an assumption, the horizontal velocity for the Ekman layer in a steady state appears in the form of a spiral. The horizontal volume transport integrated over the depth of the Ekman layer is independent of the vertical eddy viscosity; and it is perpendicular to the wind stress. It can be written in the form $\mathbf{u}_{Ekman} = -\mathbf{k} \times \boldsymbol{\tau} / f \rho_0$, where $\boldsymbol{\tau}$ is the wind stress, f is the Coriolis parameter, ρ_0 is the fluid density.

Coastal upwelling/downwelling is induced by long-shore wind. If wind blows along the coast, off-shore (or on-shore) Ekman transport must be compensated by upwelling (downwelling) along the coast. Coastal upwelling can bring nutrient-rich water from depth to the surface; thus, high productivity and good fishing grounds along some of the coastlines are closely linked to strong along-shore wind.

There are four important sites where this coastal upwelling is induced by wind, they

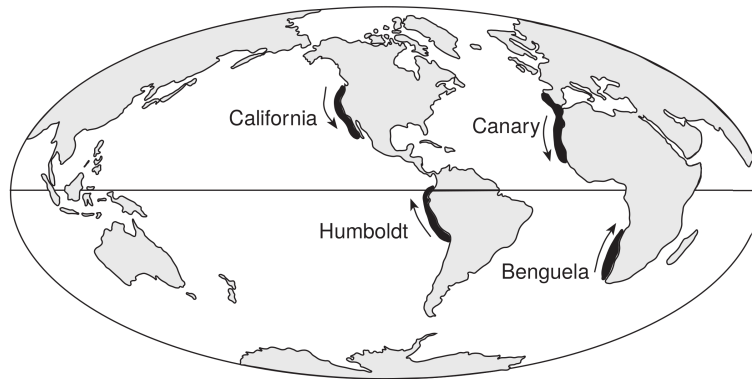


Figure 1.5: Eastern Boundary Upwelling Systems (EBUS). Arrows indicate prevailing winds.

are called Eastern Boundary Upwelling Systems (see Figure 1.5): the California Current (off Oregon and California), the Humboldt Current (off Chile and Peru), the Canary Current (off northwest Africa) and the Benguela Current (off southern Africa) Figure 1.5. They are narrow strips of the ocean that extend latitudinally over several thousands of kilometres and longitudinally to beyond the continental shelves whose widths range from 20 to 200 km. In these regions, intense trade winds combined with the earth's rotation generate coastal upwelling, bringing cold, nutrient-rich water from the deep ocean. Despite representing less than 1% of the world ocean area, their primary production accounts for about 10% of oceanic new production, and support up to 20% of the global fish catch [131].

1.5 Biological carbon pump

The Global Carbon Cycle (Figure 1.6) is the circulation through nature of carbon (in various forms, mainly as carbon dioxide). All models used in the studying of the global climate coupling the carbon cycle with climate indicate a positive feedback effect with warming, in other words, non linear interactions between climate and carbon cycle amplifying the disturbance by human activities. The carbon of fossil fuels, removed from the cycle in prehistoric times, is being returned in vast quantities as CO_2 via industrial and agricultural processes, some accumulating in the oceans as dissolved carbonates and some staying in the atmosphere which is now rapidly increasing its CO_2 content.

The oceans plays a important role in the carbon cycle, it contains 50 times more carbon than the atmosphere and uptake about 30% of human emissions of carbon dioxide[30]. The main reason is that CO_2 reacts with water to make soluble species of ions, like carbonate. This corresponds to the chemical solubility pump in which cold water holds more CO_2 in solution than warm water. This cold carbon dioxide rich water is then pumped down by vertical mixing to lower depths, then it moves horizontally by the

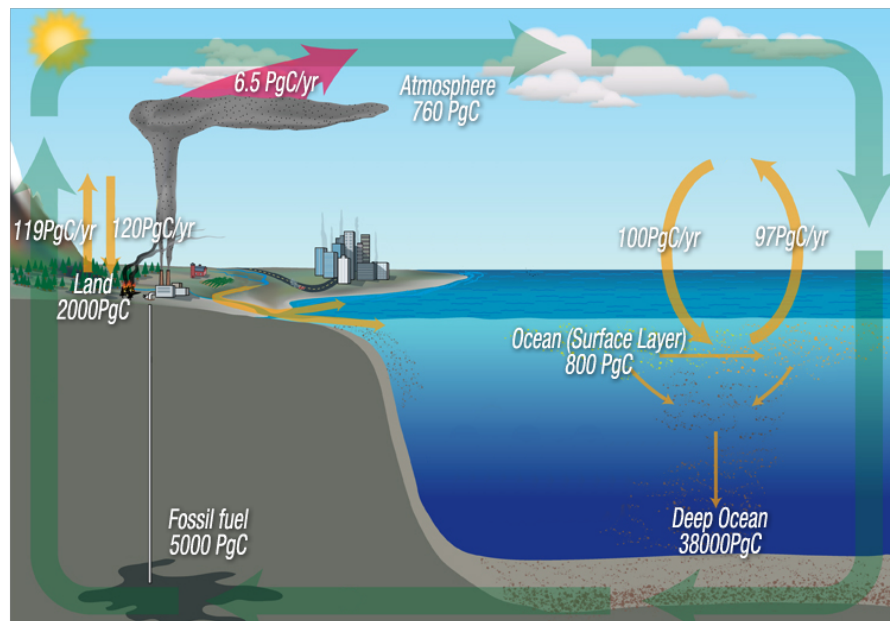


Figure 1.6: Global Carbon cycle (adapted from [30]).

thermohaline circulation. Another important mechanism of carbon sequestration by the ocean is the Biological carbon pump (Figure 1.7). It consists on photosynthetic fixation of carbon in the upper ocean followed by the downward flux of some of this material due to gravitational settling [75].

Only a small fraction of the carbon exported by biological processes (both soft-tissue and carbonate pumps) from the surface reaches the sea floor where it can be stored in sediments for millennia and longer. The residence time of remineralized and dissolved CO_2 depends on depth; it can be only an instant at the surface and as long as centuries in the deep ocean. The small portion of organic material that is not metabolized also sinks and is eventually recycled to CO_2 , but the deep ocean's slow rate of ventilation allows dissolved CO_2 to reside in the oceanic interior for as long as a millennium (see figure 1.7). Moreover during the process of sinking, bacterial degradation and grazing by zooplankton reduce the amount of organic matter that sinks. The export flux of organic material are highly influenced by the particle sizes. Single phytoplankton cells sinks very slowly $1m/day$, the formation of aggregates (marine snow) from phytoplankton, detritus, fecal pellets and minerals is essential for high sedimentation rates, about $100m/day$ or more. Therefore, organic carbon produced on euphotic layer is transported to the oceanic interior by the complex interplay of Earth's gravity and the deep-ocean ecosystem.

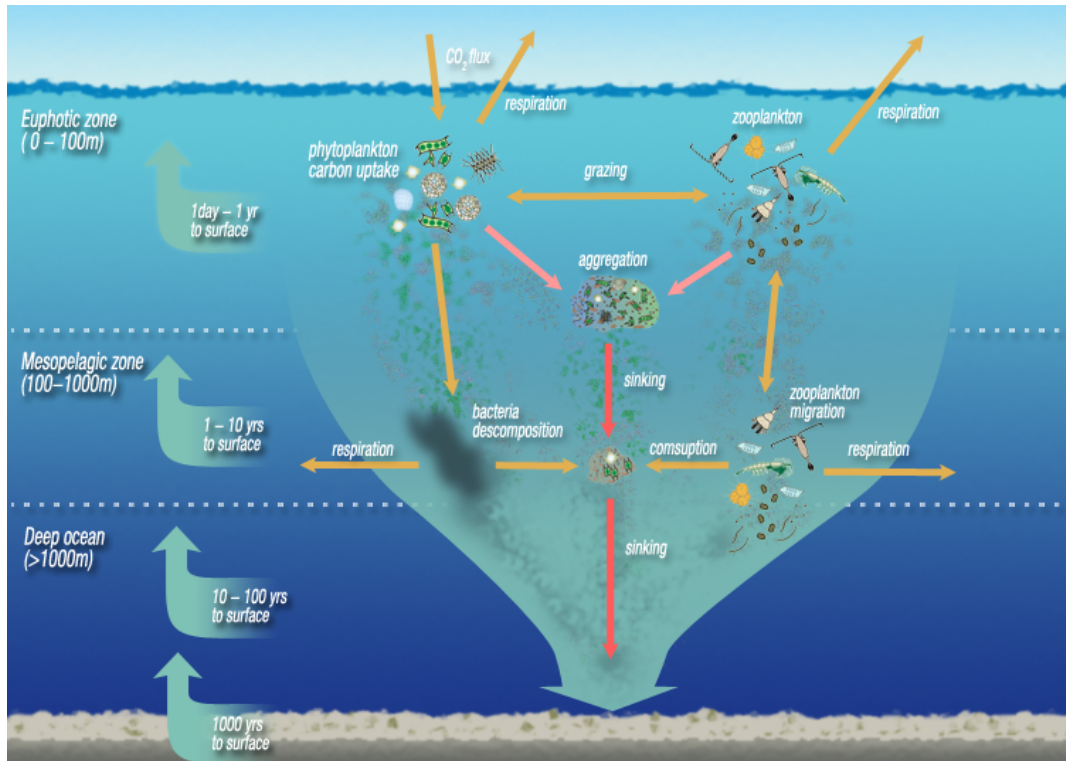


Figure 1.7: Biological Carbon Pump (adapted from [29]).

1.6 Dynamical systems approach to transport in ocean flows

The ocean flow is turbulent, it has a wide range of motion scales from a few millimeters to thousand of kilometers continuously interacting. The non linear turbulent interactions transfer energy and momentum from the largest forcing scales to the smallest dissipation scales. This flux does not only happen from large to small scales, but also from locations where forcing acts (at sea surface) to regions where dissipation is most intense (the surface and bottom boundary layer and coastal areas) [48]. Besides energy and momentum fluxes, turbulence also increases mixing and transport rates of matter or fluid properties. There are important theoretical and practical applications to how water carries tracers such as salt, nutrients, heat, as well as particulate matter such as plankton and marine debris.

The particles or properties of the flow can be described by a concentration field $C(\mathbf{r}, t)$ which depends on position \mathbf{r} and time t . The evolution of the concentration $C(\mathbf{r}, t)$ is affected by the flow and molecular diffusion. Considering an incompressible fluid $\mathbf{v}(\mathbf{r}, t)$, it is given by the following advection-diffusion equation

$$\frac{\partial C}{\partial t} + \mathbf{v} \cdot \nabla C = D \nabla^2 C, \quad (1.28)$$

where D is the molecular diffusion coefficient. At ocean large scale, diffusion time scale is very small compared to the time scale of large scale ocean flow, or equivalently, the Peclet number $Pe = \frac{UL}{D}$ is small. Hence, advection described by the term $\mathbf{v} \cdot \nabla c$ dominates, and diffusion can be neglected when studying the transport properties by oceanic currents. In this limit $Pe \ll 1$, equation (1.28) is equivalent to the motion of infinitesimal fluid elements characterized by a constant value of concentration $\frac{dC}{dt} = 0$, that rapidly adjust their own velocity to that of a background flow and do not affect the flow properties

$$\frac{d\mathbf{r}}{dt} = \mathbf{v}(\mathbf{r}, t). \quad (1.29)$$

This transport of passive scalars can be studied from the point of view of dynamical systems theory. In this context, the dynamical system is given by the equation (1.29) and the fluid trajectories are considered as the evolution in time of the state system. In this situation the *phase space* is actually the physical space in which the fluid is flowing, and geometrical structures such as invariant manifolds have an important impact on transport and mixing of the fluid [182]. However, mathematical issues arise when attempting to analyze ocean transport in the dynamical systems framework. In general we would not expect the flow to be steady or periodic in time and additionally, the velocity field is only available for a finite time. This poses some severe problems which applying dynamical systems-type ideas because typical results are found for the *long time behavior* of a system. However, a variety of methods have been developed to study transport at finite time. They have demonstrated an effective ability to find robust transport features (Lagrangian coherent structures) that organizes transport. These methods can be divided into two main categories [1], the geometric and the probabilistic or set-oriented ones. Most of the geometric methods are based on the finite version of Lyapunov exponents and set-oriented methods on the discretization of the Perron-Frobenius operator.

1.6.1 Geometrical methods: Finite Lyapunov exponents

Geometric approaches search and identify key material lines in two-dimensional flows (or material surfaces in three-dimensional flows). All material lines advected by the flow are barriers to material transported but those material lines that strongly attract or repel the neighboring material define Lagrangian Coherent Structures (LCS)[65, 63]. They form the skeleton of transport and allow a simplified understanding of the overall flow geometry.

Therefore we need to define a way of measuring distances since the focus of geometrical methods is on the rate of separation of neighboring trajectories. The trajectories correspond to the solutions of advection equation (1.29) and are given by the flow map

$$\Phi_{t_0}^\tau(\mathbf{r}_0) = \mathbf{r} \quad (1.30)$$

which maps a fluid element from its initial position \mathbf{r}_0 at time t_0 to its final position \mathbf{r} at time $t_0 + \tau$. The initial positions \mathbf{r}_0 can be considered as a set of coordinates, the

Lagrangian coordinates, in addition to the usual fixed space coordinates \mathbf{r} , designated by the Eulerian perspective. Hence, the equation (1.29) is the connection between Lagrangian and Eulerian descriptions whose solution, the flow map defined by eq. (1.30), corresponds to the transformation between both set of coordinates.

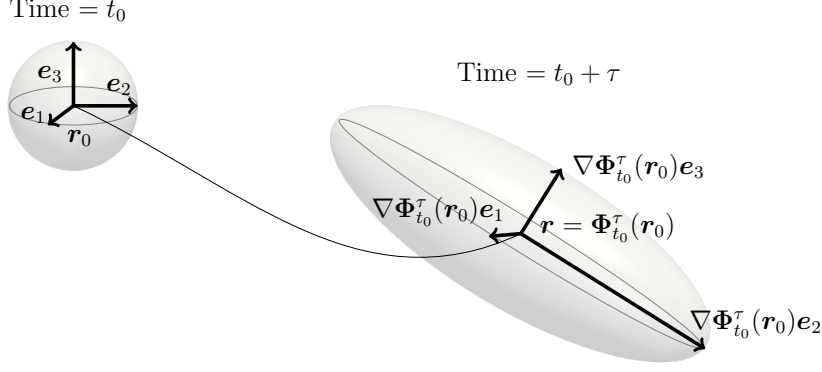


Figure 1.8: An infinitesimally small sphere initialized at position \mathbf{r}_0 is carried by the flow along the trajectory $\Phi_{t_0}^\tau(\mathbf{r}_0) = \mathbf{r}$ into a small ellipsoid at time $t = \tau + t_0$, whose principal axes are aligned with the vectors $\nabla\Phi_{t_0}^\tau(\mathbf{r}_0)\mathbf{e}_i$, where $\{\mathbf{e}_i\}$ are the eigenvectors of the Cauchy-Green tensor. The length of the i -th principal axis is $\sqrt{\Lambda_i(\mathbf{r}_0, t)}$ times the radius of the initial sphere.

The distance $\delta l(t)$ at time t between two fluid particles which were initially at \mathbf{r}_0 and $\mathbf{r}_0 + d\mathbf{r}_0$ is given by

$$\delta l(t)^2 = \sum_{i,j} C_{ij}(\mathbf{r}_0; t_0, \tau) dr_0^i dr_0^j \quad (1.31)$$

where $\mathbf{C}(\mathbf{r}_0; t_0, \tau)$ is the Cauchy-Green tensor

$$\mathbf{C}(\mathbf{r}_0; t_0, \tau) = \nabla\Phi_{t_0}^\tau(\mathbf{r}_0)^T \nabla\Phi_{t_0}^\tau(\mathbf{r}_0), \quad (1.32)$$

and the gradient of the flow map $\nabla\Phi_{t_0}^\tau(\mathbf{r}_0) = \partial\mathbf{r}/\partial\mathbf{r}_0$ corresponds to the Jacobian matrix of Eulerian-Lagrangian coordinate transformation. The Cauchy-Green tensor measures the strain of the fluid and induces a metric that tell us the distance of two infinitesimally points in Lagrangian space. This metric is symmetric and positive-definite, therefore it has positive real eigenvalues, which we denote by $\Lambda_i(\mathbf{r}_0, t)$, with corresponding orthonormal eigenvectors $\mathbf{e}_i(\mathbf{r}_0, t)$. We assume without loss of generality that $\Lambda_i \geq \Lambda_{i+1}$. The eigenvectors \mathbf{e}_i define the directions of initial separations for which neighboring fluid elements are converging or diverging, with $\sqrt{\Lambda_i(\mathbf{r}_0, t)}$ the distance separating them[63]. Considering an infinitesimal circle released at location \mathbf{r}_0 at time t_0 , it will deform into an ellipsoid when advected by the flow. The principal axes of the ellipsoid correspond to the vectors $\nabla\Phi_{t_0}^\tau(\mathbf{r}_0)\mathbf{e}_i$ (see figure 1.8). The eigenvectors and eigenvalues of the Cauchy-Green tensor are the basis for most of the geometrical approaches for identifying key coherent structures.

The finite-time Lyapunov exponents (FTLE) are the rate of exponential growth of the eigenvalues $\Lambda_i(\mathbf{r}_0, t)$

$$FTLE_i(\mathbf{r}_0, t) = \frac{1}{2t} \log \Lambda_i(\mathbf{r}_0, t), \quad (1.33)$$

In the limit $t \rightarrow \infty$, the finite-time Lyapunov exponents converge to the true Lyapunov exponents λ_i^∞ . The theorem of Oseledec [124] asserts that for ergodic measure-preserving systems this limit exists for almost all initial conditions. A flow is said to be chaotic if at least one of its Lyapunov exponents converges to a positive value. The FTLE considers infinitesimal perturbations so it still has an asymptotic character. In order to study non-asymptotic dispersion processes such as stretching at finite scales and bounded domains, the finite size Lyapunov Exponent (FSLE) was introduced. It is defined as:

$$FSLE(d_0, d_f; \mathbf{r}, t) = \frac{1}{\tau} \log \frac{d_f}{d_0} \quad (1.34)$$

where τ is the time it takes for the separation between two trajectories, initially at d_0 to reach a value d_f . In addition to the dependence on the values of d_0 and d_f , the FSLE depends also on the initial position of the particles and on the time of deployment, as was the case with the FTLE. However, by construction, for vanishing perturbations, the FSLE should coincide with the largest Lyapunov exponent [92]

$$\lim_{r \rightarrow \infty} \lim_{d_0 \rightarrow 0} FSLE(d_0, d_f; \mathbf{r}, t) = \lambda_1^\infty, \quad (1.35)$$

where $r = d_f/d_0$ is the amplification ratio.

To compute the LCS as the most repelling or attracting material surfaces, the fluid domain is discretized with a dense grid of material points where the Lagrangian expansion rate is measured (by FSLE or FTLE). The LCS corresponds to the ridges of the spatial distribution [160]. From a geophysical point of view, it is important to select properly the time for FTLE or the length scale for FSLE, based on the flow dynamics. A meaningful scale should be long enough to cover the life span of the longest dynamics in the flow dynamics, ensuring that all the influences of eddies are fully captured in the calculation of LCS. This is related to the internal radius of deformation and the duration of eddies in mesoscales in the ocean.

1.6.2 Set-oriented methods: Transfer operator

A second approach identifies regions of the flow domain for which there is a high probability of starting in one region and ending in another instead of measuring the local rate of separation of trajectories. In this case objects of interest are invariant and almost-invariant sets: collections of sets that behave in a very predictable way, in spite of the fact that individual trajectories are entirely unpredictable. These methods are based on the transfer (or Perron-Frobenius) operator, and we refer to this as the probabilistic approach or set-oriented methods.

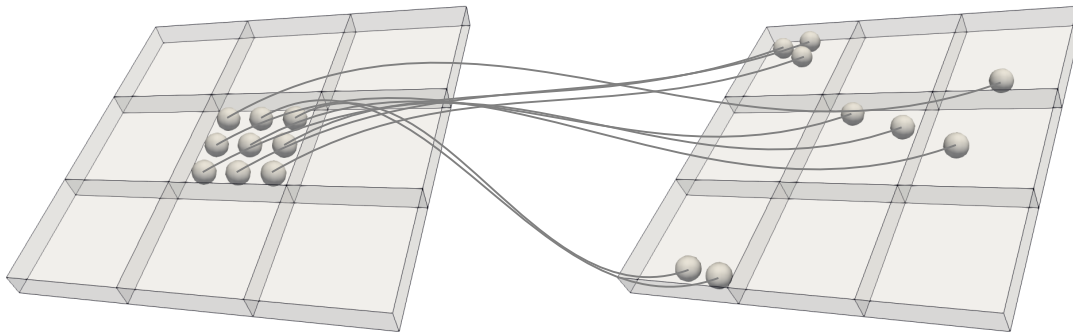
The transfer operator maps a density distribution forward from the initial to final time. First, we consider the action of the flow map (1.30) on all the points contained in a fluid region A to define the action of $\Phi_{t_0}^\tau$ on whole sets: $A(t_0 + \tau) = \Phi_{t_0}^\tau(A(t_0))$. The domain under study is partitioned into a collection of boxes $\{B_i, i = 1, \dots, N\}$ (figure 1.9). The transport between them is described using a modification of Ulam's method, a finite-dimensional representation of the transfer operator given by

$$P(t_0, \tau)_{ij} = \frac{m(B_i \cap \Phi_{t_0}^{-\tau}(B_j))}{m(B_i)} \quad (1.36)$$

where m is the fluid volume transported. As a standard way to evaluate numerically the transfer operator we apply the flow map to a large number of particles released uniformly inside each of the boxes $\{B_i, i = 1, \dots, N\}$ (see Fig. 1.9). The initial number of particles N_i in each box, a proxy of the amount of fluid it contains, should be proportional to its measure $m(B_i)$. If we chose boxes of equal area or volume, this results in seeding the same number of particles in each box. The number of particles transported from box B_i to box B_j gives an estimation of the flow among these boxes, and a numerical approximation to eq. (1.36) is then:

$$P(t_0, \tau)_{ij} \approx \frac{\text{number of particles from starting box } i \text{ to ending box } j}{N_i}. \quad (1.37)$$

Because of the time-dependence of the velocity field, the results of the Lagrangian simulations will depend on both the initial time t_0 and the duration of the simulation τ . With the calculation of this row stochastic matrix, it is possible to estimate a probabilistic analogy of the FTLE field [159].



Starting boxes at time t_0

Ending boxes at time $t + \tau$

Figure 1.9: Transport matrix construction from tracer's advection, following eq. (2.3).

The primary use of the transfer operator for dynamical systems is to find sets of coherent pairs. If coherent regions A are understood as almost-invariant areas of fluid, this means that they are mapped by the flow nearly into themselves after a time τ :

$$\Phi_{t_0}^\tau(A) \simeq A. \quad (1.38)$$

However, for time dependent systems it is necessary to introduce the concept of coherence. Sets are now transported and deformed by the flow and hence it is needed to understand how much they remain coherent under the temporal evolution. These regions, called coherent sets, are robust to perturbation and are carried along by the flow with little transport between the coherent sets and the rest of state space [50, 157].

1.7 Dynamics of finite size tracers

In the previous section, particles or tracers have been considered as passive, they move always with fluid velocity. But in the case of finite size particles with density significantly different to fluid, they do not follow instantly the fluid velocity. This section corresponds to the derivation and analysis of the dynamical equation for such finite size particles.

Let us consider a small particle of radius a and mass m_p at position \mathbf{r} at time t in an incompressible fluid flow whose velocity is $\mathbf{u}(\mathbf{r}, t)$ in the absence of the particle. The motion of the particle will modify the flow locally and leads to a new flow field $\mathbf{u}'(\mathbf{r}, t)$, which as well as $\mathbf{u}(\mathbf{r}, t)$ obeys the Navier-Stokes equations

$$\rho \left(\frac{\partial \mathbf{u}'}{\partial t} + (\mathbf{u}' \cdot \nabla) \mathbf{u}' \right) = \rho \mathbf{g} - \nabla P' + \mu \nabla^2 \mathbf{u}' \quad \text{and} \quad \nabla \cdot \mathbf{u}' = 0. \quad (1.39)$$

Additionally, the flow \mathbf{u}' must be equal to the particle velocity \mathbf{v} on the surface of the sphere $\mathbf{u}'(a, t) = \mathbf{v}(a, t)$ (no-slip condition) and at large distances from the particle position the undisturbed flow \mathbf{u} is recovered.

Knowing \mathbf{u}' the equation of motion of the particle can be obtained by

$$m_p \frac{d\mathbf{v}}{dt} = m_p \mathbf{g} + \mathbf{F}, \quad (1.40)$$

where the force \mathbf{F} exerted by the flow on the particle is given by

$$F_i = \oint_S \sigma_{ij} n_j ds \quad \text{with} \quad \sigma_{ij} = -P' \delta_{ij} + \mu \left(\frac{\partial u'_i}{\partial r_j} + \frac{\partial u'_j}{\partial r_i} \right). \quad (1.41)$$

Solving Eq. (1.41) is convenient to split the velocity \mathbf{u}' and pressure P into two contributions:

$$\mathbf{u}' = \mathbf{u} + \delta \mathbf{u}, \quad (1.42)$$

$$P' = P + \delta P, \quad (1.43)$$

where $\delta \mathbf{u}$ and δP are the flow and pressure perturbations due to the presence of the particle, respectively, and P denotes the undisturbed pressure. Consequently the fluid force is also split $\mathbf{F} = \mathbf{F}^u + \mathbf{F}^p$, being \mathbf{F}^u and \mathbf{F}^p the force due to the undisturbed and perturbation flow, respectively. The force exerted by the undisturbed flow \mathbf{u} is expressed by

$$F_i^u = \oint_S \left[-P\delta_{ij} + \mu \left(\frac{\partial u_i}{\partial r_j} + \frac{\partial u_j}{\partial r_i} \right) \right] n_j ds. \quad (1.44)$$

Eq. (1.44) may be converted to a volume integral, and considering that the typical length scale L of the flow \mathbf{u} is large compared with particle size $a \ll L$, it can be approximated by [106]

$$F_i^u \simeq \frac{4}{3}\pi a^3 \left(-\frac{\partial P}{\partial r_i} + \mu \frac{\partial^2 u_i}{\partial r_j \partial r_j} \right) \Rightarrow \mathbf{F}^u = -m_f \mathbf{g} + m_f \frac{D\mathbf{u}}{Dt}, \quad (1.45)$$

where in the last equation the Navier-Stokes for \mathbf{u} has been applied. This force corresponds to the sum of hydrostatic pressure and fluid acceleration acting on the particle. Before continuing with the derivation, it is worth noting the difference of the time derivative operators $\frac{d}{dt} = \frac{\partial}{\partial t} + \mathbf{v} \cdot \nabla$ and $\frac{D}{Dt} = \frac{\partial}{\partial t} + \mathbf{u} \cdot \nabla$ on equations (1.45) and (1.40), which denote, respectively, the time rate of change following the particle itself and the time rate of change following a fluid element in the undisturbed flow field \mathbf{u} .

Let's continue estimating the value of the force \mathbf{F}^p . To do this, it is necessary to assume that the particle Reynolds number is small

$$Re_p = \frac{aW}{\nu} \ll 1, \quad (1.46)$$

where W is the typical scale of the velocity difference $|\mathbf{v} - \mathbf{u}|$. It is also needed to assume that gradients of the flow \mathbf{u} are not too large

$$\frac{a^2 U}{\nu L} \ll 1, \quad (1.47)$$

where L and U are the characteristic length and velocity scales of the flow \mathbf{u} , respectively. Conditions (1.46) and (1.47) guarantee that the perturbed flow around the sphere (see figure 1.10) is on creeping flow regime [93]. The inertial term in the equation for the perturbed flow is small compared to the viscous term and the flow is approximated by the following unsteady Stokes equation

$$\rho \frac{\partial \delta \mathbf{u}}{\partial t} = -\nabla \delta P + \mu \nabla^2 \delta \mathbf{u}. \quad (1.48)$$

The perturbed force \mathbf{F}^p derived from the last equation (1.48) applying the boundary conditions [106, 5, 47] results in the following expression

$$\begin{aligned} \mathbf{F}^p = & -6\pi a \mu (\mathbf{v} - \mathbf{u} - \frac{a^2}{6} \nabla^2 \mathbf{u}) \\ & - \frac{m_f}{2} \left(\frac{d\mathbf{v}}{dt} - \frac{D}{Dt} (\mathbf{u} + \frac{a^2}{10} \nabla^2 \mathbf{u}) \right) \\ & - 6a^2 \rho_f \sqrt{\pi \nu} \int_0^t dt' \frac{\frac{d}{dt'} (\mathbf{v} - \mathbf{u} - \frac{a^2}{6} \nabla^2 \mathbf{u})}{\sqrt{(t-t')}}. \end{aligned} \quad (1.49)$$

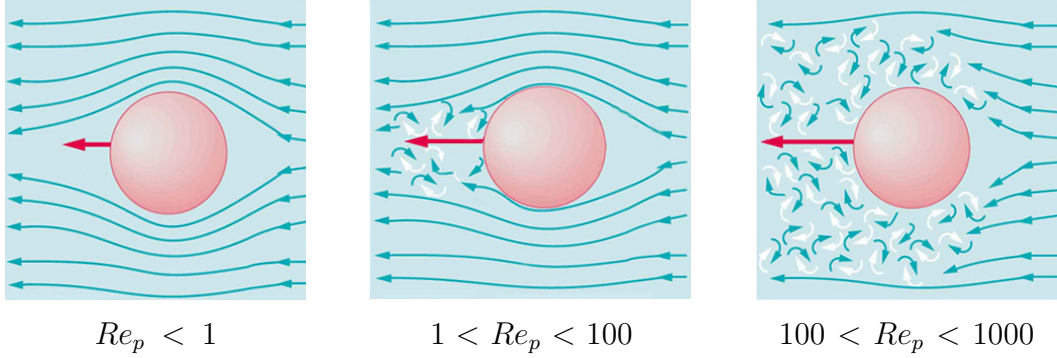


Figure 1.10: Flow regimes around sphere as function of its particle Reynolds number Re_p .

The first term of the above expression, called Stokes drag, is essentially due to viscous forces and velocity differences between the particle and the fluid. The second term is the added mass force. It corresponds to the motion of part of the surrounding fluid as the particle moves through it [5]. The added mass is half the mass of the displaced fluid. The third term is the Basset-Boussinesq history force, which is related to the diffusion of the vorticity around the spherical particle. This arises due to time variations in the drag force exerted by the particle on the fluid. It is proportional to a^2/ν which corresponds to the time scale for the transmission of drag variations into changes in the fluid's inertia in the viscous boundary layer. The terms with $a^2\nabla^2\mathbf{u}$ are the Faxén corrections [47].

Finally substituting the force expressions (1.45) and (1.49) in equation (1.40) we obtain

$$\begin{aligned}
m_p \frac{d\mathbf{V}}{dt} = & (m_p - m_f)\mathbf{g} \\
& + m_f \frac{D\mathbf{u}}{Dt} \\
& - 6\pi a\mu(\mathbf{v} - \mathbf{u} - \frac{a^2}{6}\nabla^2\mathbf{u}) \\
& - \frac{m}{2} \left(\frac{d\mathbf{v}}{dt'} - \frac{D}{Dt}(\mathbf{u} + \frac{a^2}{10}\nabla^2\mathbf{u}) \right) \\
& - 6\pi a^2\mu \int_0^t dt' \frac{\frac{d}{dt'}(\mathbf{v} - \mathbf{u} - \frac{a^2}{6}\nabla^2\mathbf{u})}{\sqrt{\pi\nu(t-t')}}.
\end{aligned} \tag{1.50}$$

These equations are termed the Maxey-Riley-Gatignol [107, 54, 111, 26] equation (MRG in the following).

The full MRG is very complicated to manage. A further simplification is usually performed based on the single assumption of very small particles (what this exactly means will be discussed later on). With this, the Faxén corrections and the history term (since $a/\sqrt{\nu} \ll 1$) can be neglected [107, 111, 64]. Note however that the history term

can be relevant under some conditions, as for example larger particle size [36, 59, 58, 123]. Thus we obtain the standard form of the MRG equations [107]:

$$\frac{d\mathbf{v}}{dt} = \beta \frac{D\mathbf{u}}{Dt} + \frac{\mathbf{u} - \mathbf{v} + \mathbf{v}_s}{\tau_p}, \quad (1.51)$$

where $\beta = \frac{3\rho_f}{2\rho_p + \rho_f}$, the Stokes time is $\tau_p = \frac{a^2}{3\beta\nu}$, and $\mathbf{v}_s = (1 - \beta)\tau_p\mathbf{g}$ is the settling velocity in quiescent fluid. For heavy particles ($\rho_p \gg \rho_f$), $\beta \rightarrow 0$, while for light particles ($\rho_p \ll \rho_f$), $\beta \rightarrow 3$. For neutrally buoyant particles ($\rho_p = \rho_f$), $\beta = 1$ Equation (1.51) is the starting point for most inertial particle studies [111, 9, 26].

Using the typical length L , velocity U and time $T = U/L$ of the flow, we get the following dimensionless form of equation (1.51)

$$\frac{d\mathbf{v}^*}{dt^*} = \beta \frac{D\mathbf{u}^*}{Dt^*} + \frac{\mathbf{u}^* - \mathbf{v}^* + \mathbf{v}_s^*}{St}, \quad (1.52)$$

the dynamics is strongly controlled by the parameter $St = T/\tau_p$ the Stokes number, the dimensionless decay time in the velocity difference between particle and fluid. The limit $St \rightarrow 0$ (irrespective of β) corresponds to the passive tracer limit. Particles with $St \ll 1$ respond instantaneously to fluid variations. In the other hand, for $St \gg 1$ the particles' inertia is so large that the particle is essentially insensitive to the flow. For these particles the dynamics is nearly ballistic.

1.7.1 General Features of the Dynamics of inertial particles

Inertial particles are characterized by a finite-size and/or density different from that of the surrounding fluid. Due to their inertia, they have their own velocity dynamics in contrast to passive particles which follow the same dynamics as fluid parcels. The inertial particle dynamic is governed by the second-order differential equation (1.51), at difference of passive tracer equation (1.29) which is of first order. An immediate consequence of this is that phase-space of the finite-size dynamics is double than phase-space of passive particles. And the dynamics in this phase space spanned by (\mathbf{r}, \mathbf{v}) is dissipative. The divergence of the right hand sides of (1.52) with respect to (\mathbf{r}, \mathbf{v}) is strictly negative and equal to d/St where d is the space dimension, i.e. phase-space volumes are uniformly contracted at a rate d/St . Then, since the particle velocity \mathbf{v} has a non-zero divergence even in an incompressible fluid, this inertial effect leads to the appearance of strongly inhomogeneous distributions (*preferential clustering*) (Balkovsky et al., 2001a).

The fluid mechanical origin of this *preferential clustering* can be understood studying

the perturbative expansion of equation (1.52) for $St \rightarrow 0$, the passive tracer limit [64]

$$\mathbf{v}(\mathbf{r}, t) = \mathbf{u}(\mathbf{r}, t) + St\mathbf{u}^1(\mathbf{r}, t) + St^2\mathbf{u}^2(\mathbf{r}, t) + \dots \quad (1.53)$$

$$\text{with} \quad (1.54)$$

$$\mathbf{u}^1(\mathbf{r}, t) = (\beta - 1) \frac{D\mathbf{u}}{Dt} \quad (1.55)$$

$$\mathbf{u}^k(\mathbf{r}, t) = - \left(\frac{D\mathbf{u}^{k-1}}{Dt} + (\mathbf{u}^{k-1} \cdot \nabla)\mathbf{u} + \sum_{l=1}^{k-2} (\mathbf{u}^l \cdot \nabla)\mathbf{u}^{k-l-1} \right), k > 1. \quad (1.56)$$

The first order in St , results in a finite compressibility for the particles velocity field [27]

$$\nabla \cdot \mathbf{v} = -St(1 - \beta)(\omega^2 - s^2) \quad \text{with} \quad s^2 = s_{ij}s_{ij} \quad \text{and} \quad \omega^2 = \omega_{ij}\omega_{ij}, \quad (1.57)$$

where s_{ij} and ω_{ij} are the symmetric (strain) and the antisymmetric (vorticity) parts of the velocity gradient $\nabla\mathbf{v} = s + \omega$. The field $\omega^2 - s^2$ is positive in regions dominated by vorticity and negative in regions dominated by the strain. From Navier Stokes equation, $\omega^2 - s^2 = \nabla^2 p$ [49]. Therefore particles of density higher than the fluid (aerosols, with $\beta < 1$), tend to move away from regions of high vorticity, such as the centers of eddies. This effect can be intuitively understood as the result of a centrifugal force acting on the particle and pushing it away from a highly-rotating region. Conversely, particles with lower density than the fluid (bubbles, with $\beta > 1$) tend to move towards high-vorticity regions. So bubbles tend to agglomerate in the centres of vortices. Therefore, at least for $St \ll 1$, we can trace back the origin of particle clustering to the preferential concentration of particles in or out of high vorticity regions depending on their density.

CHAPTER 2

Lagrangian Flow Networks to study the multi-scale connectivity of marine populations

Assessing the spatial structure and dynamics of marine populations, especially considering the various and interlocked scales typical of oceanic systems, is still a major challenge in Ecology. The framework based on the construction and analysis of Lagrangian Flow Networks (LFN) results in a systematic characterization of dispersal and connectivity of early life history stages of marine organisms. The network is constructed by subdividing the basin into an ensemble of sub-regions which are interconnected through the transport of propagules by ocean currents. The analysis of such networks allows the identification of hydrodynamical provinces and the computation of connectivity proxies measuring retention and exchange of larvae at multiple scales. Due to our spatial discretization and subsequent network representation, as well as our Lagrangian approach, further methodological improvements are handily accessible. It permits a better characterization of population connectivity and allows improving the management and protection of marine ecosystems. We present here a modelling framework to characterize larval dispersal and connectivity in the marine realm. After briefly presenting the Lagrangian Flow Network methodology, we highlighted one case-study focused on different scales and we examine the effects of larval dispersal for population ecology.¹

¹This chapter is based on: V. Rossi, M. Dubois, E. Ser-Giacomi, P. Monroy, E. Hernández-García and C. López. *"Lagrangian Flow Network: a new tool to evaluate connectivity and understand the structural complexity of marine populations"*. *CIESM Workshop Monograph 48: Marine connectivity - migration and larval dispersal*, edited by F. Briand, CIESM Publisher, Monaco, 39-51 (2016). And also the article: M. Hidalgo, V. Rossi, P. Monroy, E. Ser-Giacomi, E. Hernández-García, B. Guijarro, E. Massutí, F. Alemany, A. Jadaud, J. L. Pérez and P. Reglero. *"Accounting for ocean connectivity and hydroclimate in fish recruitment fluctuations within transboundary metapopulations"*. To appear in *Ecological Applications* (2019).

2.1 Introduction

Dispersal, the tendency for organisms to move, settle and ultimately reproduce away from their native habitats and parents, influences many evolutionary and ecological processes, from speciation and species persistence (long-term survival) to biological invasions and the resilience of ecosystems to external perturbations [43]. Dispersal and the tightly related concept of *connectivity* have been shown to favour the access to feeding and nursery grounds [108], to influence demographic rates of subpopulations [127], to control the coexistence of genotypes within species [97], to affect population structures and dynamics [33], to regulate biodiversity [31, 82] and to plan conservation strategies [57, 53, 148, 42].

Studying connectivity in marine ecosystems, as in terrestrial ones [25], is thus crucial. Yet, the highly variable properties of seawater and its dynamical character have profound effects on the connectivity of marine systems. Indeed, because the life cycle of most marine organisms encompass an embryo phase (eggs and larvae), and considering that juveniles and adults tend to be rather territorial, one of the most important process of dispersion is the transport of propagules by ocean currents over large distances [33]. The marine realm is an heterogeneous medium in perpetual movement with non-linear processes occurring at various scales, from diffusive dynamics, eddy-driven mixing, up to basin-scale advective currents [149, 31]. Over the last decades, oceanographers recognized the prominence of mesoscale and sub-mesoscale structures (whose scales span approximatively over 1-100 km and 1 day to several months) in oceanic flows [147, 24, 103, 101]. These studies revealed the presence of barriers (which prevent the dispersion of propagules) and of preferential corridors of transport (favouring efficient connections), having important consequences for the dispersal and retention of non-swimming larval stages [66, 179, 148, 42]. Even for life-stages that are actively mobile, the oceanic circulation governs the spatial distribution of environmental variables and planktonic food [185], thus playing a crucial role in controlling the location, timing and success of spawning, dispersal and settlements [104, 142].

2.2 Metapopulations and subpopulations in marine seascapes

Marine populations are structured as a large "metapopulation" in which discrete "subpopulations" are linked to each other via the exchanges of individuals, occurring essentially during the embryo phase (eggs and larvae) for most marine organisms [33]. This population connectivity (i.e. exchange of individuals among subpopulations) is difficult to observe and quantify [23]. Nevertheless, it can be inferred from different approaches as it influences other biological processes. In particular, it is related to the concepts of genetic connectivity (defined as the degree to which gene flows affect evolutionary processes within subpopulations) and of demographic connectivity (which takes into account

the impact of dispersal processes on the growth and mortality rates of a subpopulation). Indeed, the magnitude and modality of larval dispersal by ocean currents are theoretically expected to affect both genetic and demographic connectivities. Consequently, studying the transport of larvae with biophysical models and discussing its managerial and genetic implications have received growing interests [112, 88, 57, 177, 3, 183, 148].

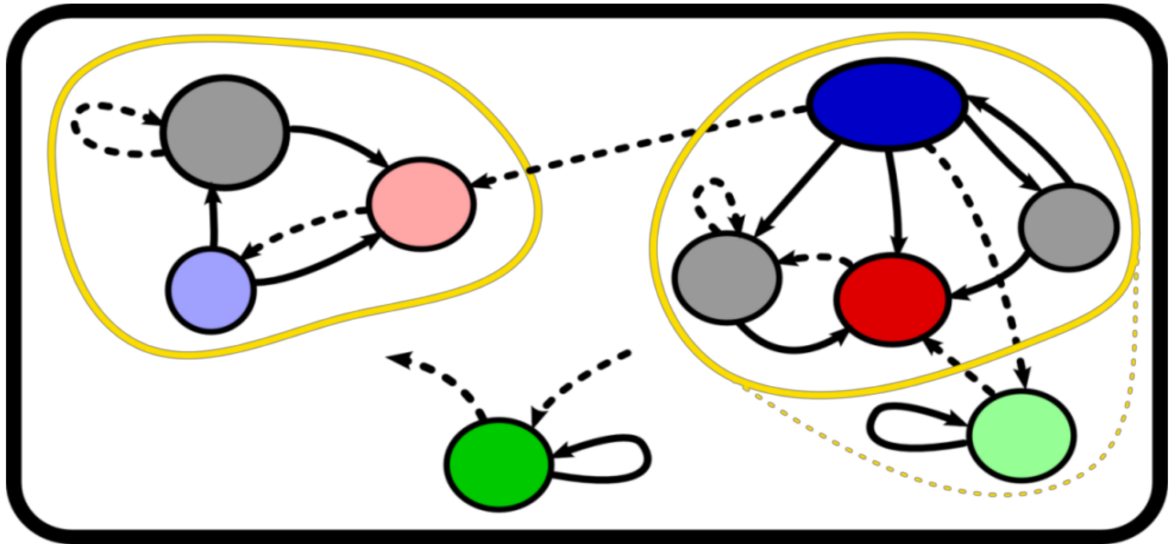


Figure 2.1: Schematic meta-population (black rectangle) composed of several subpopulations (black-outlined ellipses) with different connectivity behaviors (intensity is proportional to the darkness of the coloring). Green ellipses represent relatively “closed” subpopulations while the rests are “open” subpopulations. The latter group is further distinguished: blue ellipses illustrate “source” subpopulations while “sink” ones are red. Yellow contours identify “communities” within the meta-population system. Black arrows symbolize exchange of individuals, here assumed to be mainly due to larval transport (dotted arrows exemplify smaller larval fluxes than plain ones).

The contrasting connectivity occurring in the real ocean has been simplified by distinguishing, according to the specific migration rates, open subpopulations that receive/export individuals from/to other subpopulations and closed subpopulations that do not exchange individuals to an appreciable extent (Figure 2.1) [73, 132]. This implies that open subpopulations are primarily maintained through network persistence while closed subpopulations survive through self-persistence. Another distinction was introduced by [136] with the concept of source/sink dynamics. Habitat heterogeneity and variable dispersal ability lead to different demographic and exchange rates in each subpopulation, so that a source population is characterized by a net export of individuals greater than the net import; the reverse is a sink [33]. Characterizing the connectivity of marine subpopulations led to the definition of various local connectivity metrics related to lar-

val transport: Self-Recruitment (SR) measures the proportion of all local larval recruits that originated from the source population [133]; Local Retention (LR) is defined as the proportion of local larval production retained on a site [74, 21].

Understanding the connectivity of these complex subpopulations has crucial ecological and managerial implications [42]. The need to manage marine resources from a large-scale perspective and considering the whole ecosystem is now accepted. The adequacy of such strategies requires a global view encompassing the large dimensions of oceanic systems and a characterization of connectivity processes relevant for organisms with contrasting life histories within a given ecosystem (instead of mono-specific focus). However, the absence of appropriate tools to face these challenges limits the implementation of globally pertinent conservation plans.

2.3 Lagrangian Flow networks applied to larval dispersal

The Lagrangian Flow Network (LFN) framework has demonstrated great effectiveness in studying larval dispersal [148, 158]. It is based on discretization of the system region and allow to use tools from graph theory. It is a modeling framework that allows characterizing larval dispersal and its impacts on the spatial structures and dynamics of marine populations from a large-scale perspective [42]. Specifically, LFN represents fluid transport among different oceanic regions as a network of nodes interconnected by directed and weighted links. Each node corresponds to a geographical sub-area of the oceanic surface and can be seen as a discrete habitat patch. Each link symbolizes an effective mass transport driven by ocean currents between any two of these sub-areas during a given time interval, representing larval transport pathways. This framework is ideal to study the structure of marine populations which are commonly organized as discrete subpopulations whose respective persistence depends on self-replenishment and asymmetric exchanges of individuals (here assumed to be mainly mediated by larval transport) among fragmented habitats (nodes) [86, 42].

The construction of LFNs consists in four steps or modules (see figure 2.2):

1. Divide the region in oceanic boxes which are the nodes of the network (the size of these boxes is in general larger than the grid used by the hydrodynamic model to compute velocities) and then initialize evenly the particles inside each node.
2. Compute the Lagrangian trajectories for all particles in each node and record the node of their final positions.
3. Calculate the connectivity matrix or adjacency matrix² \mathbf{P} of the LFN and its binary equivalent \mathbf{L} . The element $P_{i,j}$ of the connectivity matrix is defined as the

²The adjacency and connectivity matrix are used in Network theory and marine connectivity, respectively, to call the transfer operator, already described in sec. 1.6.2

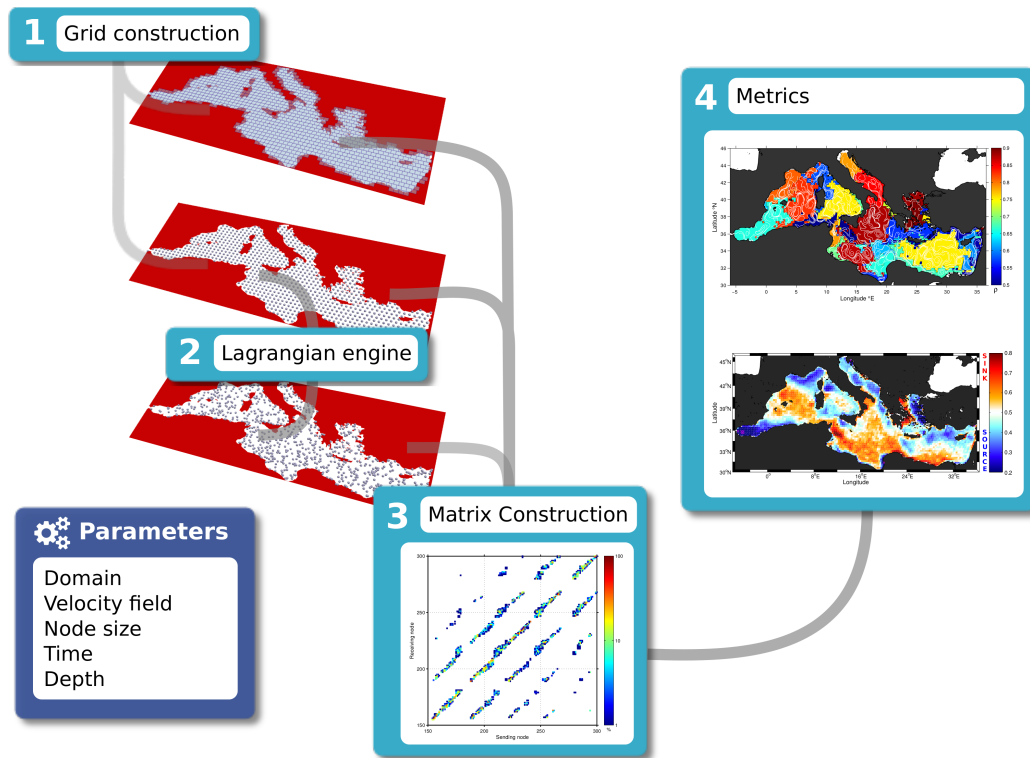


Figure 2.2: Simplified diagram of the Lagrangian Flow Networks set-up with 4 modules (light blue boxes). Key parameters (dark blue box) are the domain of interest, the velocity field (from any ocean model), the node size, the starting dates (spawning events), the vertical layer of the model (depth of dispersion) and the tracking time (Pelagic Larval Duration).

probability that a particle released in node i settles at node j after the tracking time (PLD). It can be estimated by the number of particles exchanged from node i to node j divided by initial number of particles in node i . The elements of the binary connectivity matrix are $L_{i,j} = 0$ if $P_{i,j} = 0$ (i.e. no larval flow) and $L_{i,j} = 1$ when $P_{i,j} \neq 0$ [158].

4. Perform various and complementary post-processing of both matrices (P and L) to obtain relevant metrics and study connectivity.

The framework is tunable to any target species through the use of specific parameters that match the traits of this organism. For instance, the dispersal of hake's larvae are being studied with the LFN by simulating successive spawning events during autumn using a PLD of 40 days and the currents at $\sim 100m$

2.4 Local network measures as proxies of larval connectivity

Network Theory tools permit the examination of both local and global properties of such network [119] [159]. Detecting communities is an important application of the studying of the global properties of the network. The Infomap algorithm can be applied to the connectivity matrix allowing to divide the oceanic surface in hydrodynamical provinces, which are well connected internally but with minimal exchanges of larvae between them [148]. Focusing on local (node-scale) features and inspired from concepts of Population Dynamics, we also describe larval transport and exchange by computing indices of retention and source-sink proxies at basin-scale [42]. The connectivity matrix is manipulated to examine, for each node, the number and fluxes of all links emanating from it and entering it. Through a combination of these basic variables, and by assuming that local larval release, larval mortality and success of recruitment are homogeneous,[42] we computed four complementary connectivity metrics. These metrics estimate the extent to which subpopulations are open/closed or source/sink and are computed using the formulae reported in [42].

- Local Retention LR_i is the ratio of locally produced settlement to local larval release in node i . Since local larval release and the success of recruitment are here assumed to be homogeneous in space, LR_i can be approximated for each node by the proportion of locally retained particles (i.e. diagonal elements of \mathbf{P}):

$$LR_i = P_{ii} \in [0, 1]. \quad (2.1)$$

- Self-Recruitment SR_i is the ratio of locally produced settlement to the overall settlement in node i . With our assumptions, corresponds to the ratio of retained particles in each box to the total incoming particles from all origins (including those produced locally):

$$SR_i = \frac{P_{ii}}{\sum_{k=1}^N P_{ki}} \in [0, 1]. \quad (2.2)$$

- Source-Sink strength SS_i^s evaluates the source/sink character in terms of the total fluxes of larvae (relative importance of larval export versus import) in node i and it is defined by

$$SS_i^s = \frac{IN_i^s}{IN_i^s + OUT_i^s} \in [0, 1] \quad (2.3)$$

where the local OUT-strength OUT_i^s and IN-strength IN_i^s are given by

$$OUT_i^s = \left(\sum_{k=1}^N P_{ik} \right) - P_{ii}, \quad (2.4)$$

$$IN_i^s = \left(\sum_{k=1}^N P_{ki} \right) - P_{ii}, \quad (2.5)$$

which measures the proportion of particles released (arriving) locally that were transported (originated from, respectively) elsewhere.

- Source-Sink degree SS_i^d evaluates the source/sink character in terms of the diversity of origin and destination sites:

$$SS_i^d = \frac{IN_i^d}{IN_i^d + OUT_i^d} \in [0, 1] \quad (2.6)$$

where the local OUT-degree OUT_i^d and IN-degree IN_i^d are given by

$$OUT_i^d = \left(\sum_{k=1}^N L_{ik} \right) - P_{ii}, \quad (2.7)$$

$$IN_i^d = \left(\sum_{k=1}^N L_{ki} \right) - L_{ii}. \quad (2.8)$$

These node-scale metrics are all restricted to values between 0 and 1. Elevated retention is represented by LR and SR approaching 1. The negative (positive) deviations of SS_d and SS_s from 0.5 allow the quick appraisal of sources (sinks).

2.5 Case study: connectivity within the metapopulation of a harvested species

In this case study, we adapted the LFN methodology to the European hake (*Merluccius merluccius*). It is a demersal fish largely distributed across continental shelves of the Mediterranean with important landings in all countries. Its spawning occurs during autumn, its PLD is about 40 days and its larvae are supposedly drifting at the subsurface. We aim at addressing the following objectives: the potential larval connectivity within and among six discrete subpopulations of hake in the Western Mediterranean and whether the connectivity estimates help to explain the temporal dynamics of recruitment and survival. This was made by combining ocean circulation models and time-series of regional climate and biological variables, which allow to model the spatiotemporal dynamics of hake recruitment.

The study region is structured by recognized physical and environmental boundaries, and the phenology of key ecological processes such as spawning and recruitment. Accordingly to recent studies we simplify our metapopulation to six distinct eco-regions: Gulf of Lions, Catalan coast, Ebro delta, Valencia gulf, northern and southern Balearic Islands (figure 2.3). This structure of the metapopulation system implies that all larvae ending their dispersal phase outside of these regions are considered lost. Similarly, it presupposes that the potential arrival of dispersed larvae from other hake metapopulations is very unlikely and the effect minimal.

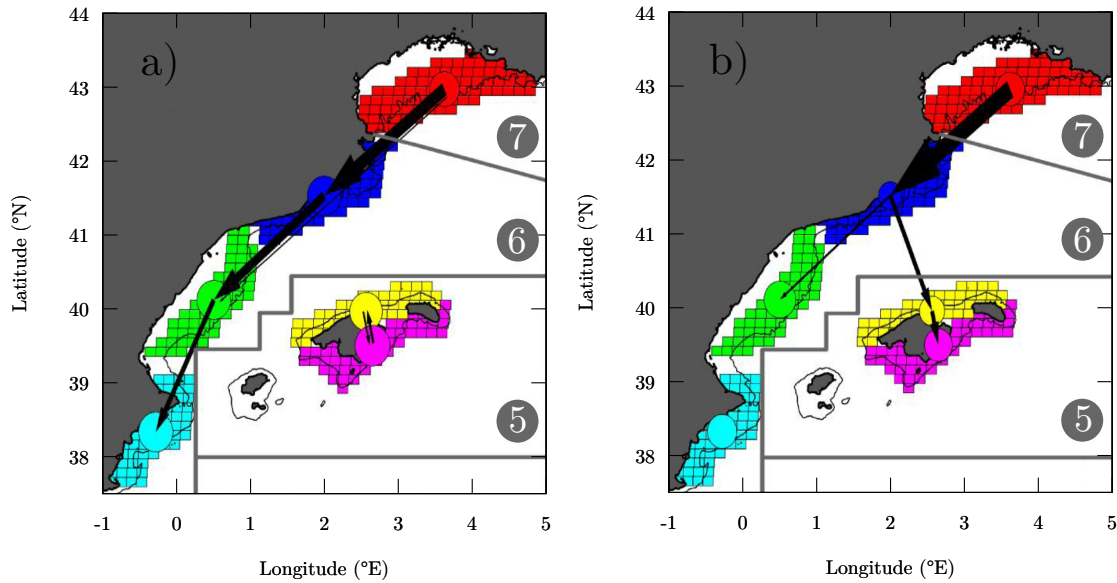


Figure 2.3: Normalized estimates of larval exchanges (arrows) and retention (circles) among the different sub-populations of hake. Only fluxes greater or equal than 5% of the total annual exchanges are displayed. The two panels are examples illustrating the two contrasting scenarios of connectivity. (a) Year 1989 shows the main south-westward transport pattern along the mainland with almost no import into the Balearic archipelago. (b) Year 2005 exhibits a reduced southwestward transport and stronger connections with the Balearic Islands. Different sub-areas (representative of Hake’s subpopulations) are: Gulf of Lion (red), Catalan coast (dark blue), Ebro delta (green), Ibiza channel (light blue), north Balearic Islands (yellow) and south Balearic Islands (magenta). Widths of arrows (diameters of circles) are proportional to the strength of connection (larval retention, respectively). Grey thick lines represent the three Geographical Subareas (GSAs) that correspond with management units used by the General Fisheries Commission of the Mediterranean: Gulf of Lion (GSA-7), Iberian Peninsula (GSA-6) and Balearic Archipelago (GSA-5). Black contours show the 200 m isobaths. Black contours show the 200 m isobaths.

The LFN model provided the inter-annual variability of connectivity proxies among the different areas of the Western Mediterranean Sea. The oceanic surface is subdivided in thousands of equal-area rectangular sub-regions that serve as nodes (small boxes in figure 2.3) in our transport network. These nodes, equivalent of discrete habitat patches, are interconnected by weighted and directed links that represent passive transport of hake’s propagules (eggs and larvae) by ocean currents. Those links are orientated by the oceanic flow and are weighted proportionally to the normalized larval fluxes occurring

over the entire period of the pelagic phase. Particles were seeded evenly in each node (100 particles per node) at a fixed subsurface layer. We retained here the layer at 90 m depth, where hake larvae have been mostly observed [122]. The Pelagic Larval Duration (PLD) simulated is 40 days [71]. We considered repeated spawning events each year during the main autumnal spawning period of the species with seven starting times (15 days apart) from September, 1st to November, 30th [71]. The three complementary connectivity metrics exploited here are: Import, Local Retention and Self-Recruitment (see section 2.4). Import (Imp) is the total number of incoming larvae from all origins.

We use time-series of hake recruitment over 1980-2014 from assessment groups to assess the potential influence of connectivity in the population dynamics of hake, in combination with additional hydro-climatic drivers such as the Regional Hydrodynamic Index (RHI) [115]. The RHI index corresponds to the standardized winter (December-March) air surface temperature anomalies [115]. This provides the simplest and best index for late spring Mediterranean Intermediate Water (WIW) presence in the Balearic Channels and therefore for the corresponding ocean circulation (figure 2.4). Negative values of this index are associated to higher formation rate of winter intermediate water mass, which influences the seasonal surface circulation patterns. During cold winters, cool water is formed at intermediate layers (100–300 m) in the Gulf of Lions. This Western WIW usually moves southward reaching the Balearic Channels, deflecting the warmer Levantine Intermediate Water (LIW) coming from the Eastern Mediterranean, and even blocking the Ibiza Channel. On the other hand, during mild winters, less WIW is formed and then LIW flows through the channels, appearing at their characteristic depths (figure 2.4). The RHI index is used for seeking relationships between hydrodynamics conditions and the connectivity pattern around the Balearic Islands. While it suggested that the RHI captures biophysical processes mainly related to early life stages survival, it is not yet clear if and how they could be related to dispersal.

Larval exchanges simulated by the Lagrangian Flow Network (LFN) among the 6 discrete subpopulations of hake suggest that the subsurface circulation in the north-western Mediterranean, dominated by the Liguro-Provencal-Catalan current, drives a southwestward directional pattern of connectivity (figure 2.3). The Gulf of Lion is thus the main source of particles Import into the Iberian Peninsula. While this southwestward connectivity prevails in all 25 years under study, two distinct scenarios can be distinguished. The first connectivity pattern consists in a southwestward flux to the mainland, with a weak or null transport towards the Balearic Islands (figure 2.3). The second one reveals a reduced transport towards the Iberian Peninsula shelf and an eastward retroflexion of the main transport pathways, resulting in stronger connections with the Balearic Archipelago (figure 2.3). Larval Local Retention (LR) also displays consequent spatiotemporal variability, which seems less prominent than the changes of directional connectivity patterns (figure 2.3).

A statistical model was developed in [72] to assess the relative importance of the different connectivity indices and the climatic index RHI on the hake population fluctuations (figure 2.5). SR and RHI effects were the most representative in all management areas. Using a non-parametric test to compare the annual averages of SR among the 6 subpopulations we found that SR is significantly different in all subpopulations, except

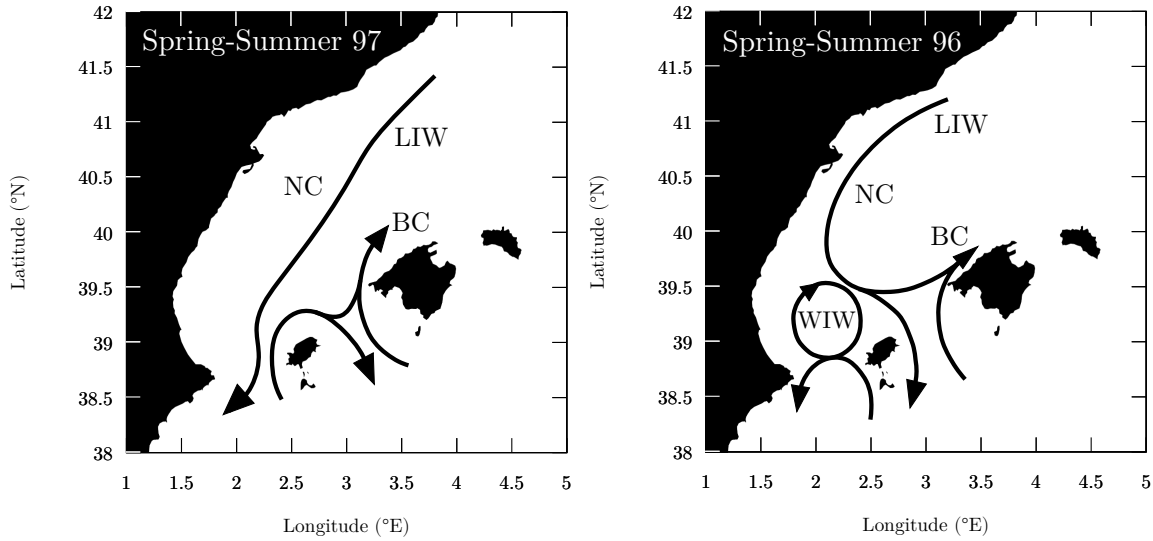


Figure 2.4: Regional ocean circulation pattern in the western Mediterranean corresponding to late spring–summer after a relatively mild winter, May 1997 (a) and after a relatively cold winter, May 1996 (b). Major currents in the region, the Northern Current (NC) and the Balearic Current (BC) are indicated. Adapted from [115].

comparing North Balearic Islands with Ebro delta and South Balearic Islands with Valencia gulf. For the RHI index, a clear directional change is observed from a negative significant effect on recruitment in the Balearic Islands (i.e., recruitment is favored under negative values of RHI) to a positive significant effect in the Gulf of Lion, and no effect observed in the Iberian Peninsula (figure 2.5).

Our study provides evidence of directional connectivity following the main pathways of the most prominent currents flowing through the study area. However, important inter-annual variability of connectivity is observed both for the retention and exchange of larvae. Overall, the Gulf of Lion is a main source contributing to the Spanish mainland coast, while the Balearic Sea appears as a sink receiving particles from several areas of the mainland. This suggests a potential complex metapopulation system with three main components: a source (Gulf of Lion), a sink (Balearic Islands) and a transition area (Spanish mainland coastline). The inter-annual variability of the connectivity processes and the temporal evolution of the RHI index explain together the inter-annual variability of recruitment estimated in the assessment groups and those observed by the scientific trawl surveys. Both connectivity processes and the RHI index influenced the hake density at the main nursery areas in the north of the Balearic archipelago: maxima of recruits are observed when connectivity is high and the RHI favored the survival of larvae. In contrast, the nursery area in the south seems more stable through time and is more dependent on SR. Overall, both the degree of connectivity that takes place from the

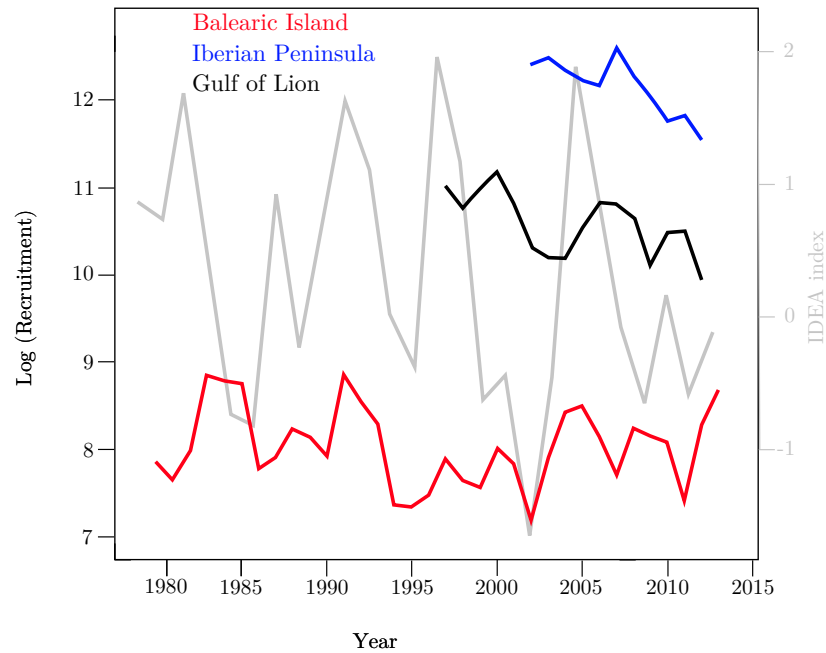


Figure 2.5: Time-series of annual recruitments from fisheries assessment in the three management areas (Balearic Islands, red colors; Iberian Peninsula, blue colors; Gulf of Lion, black colors) and the Regional Hydroclimatic Index (RHI, grey curve) [7].

end of autumn to early winter, and the RHI index that represents the hydro-climatic scenario affecting the survival of early life stages and prerecruits from the end of winter to spring, shape together the spatial pattern of hake recruits in spring [71].

Historically, marine populations tended to be classified as open or closed according to their replenishments being ensured primarily by immigrants or by local production [73]. While this dichotomy and its management implications could be applied in small metapopulation of littoral sedentary species (i.e., when connectivity processes are relatively well captured by local retention), it does not hold for most offshore fish stocks for which there is an increasing awareness that spatial and demographic structure is more complex than currently accounted for [22]. This inherently calls for indicators that properly parameterize the observed continuum between open and closed systems beyond stock boundaries and that are able to account for both local and distant connectivity processes. In this view, Self-Recruitment (SR), which was defined to take into account the influences of both local recruits and immigration from the surrounding subpopulations [17], seems best adapted. Indeed, our study shows that larval SR is the best synthetic predictor of fisheries recruitment, as it constitutes the mechanistic link among the three management areas of the European hake in the Western Mediterranean. We found that SR of four hake subpopulations are mainly controlled by the inter-annual variations of Import, emphasizing the role of network persistence. We also showed that variability in both LR and Imp in the Catalan Coast and in the northern Balearic Islands con-

tribute to meaningful changes in their respective SRs, indicating the importance of both network- and self-replenishment. Our results suggest that all subpopulations behave as sources, with stronger larval export than import.

Together with SR, the climatic index has an elevated explanatory power in two of the three management units. Our results reinforce the inverse relationship between this index and hake recruitment already documented in the Balearic Islands [105]. Low values of the index are related to anomalously intense formation of intermediate waters in the Gulf of Lion forced by winter wind-driven vertical mixing [7]. These nutrient-rich waters then flow further south and increase biological productivity in the Balearic sea, an area especially oligotrophic in the western Mediterranean, enhancing food availability for hake larvae and juveniles there [105]. These findings reveal how the link between climate variability and its ecological impact is geographically structured at regional scales. In this case, the same local oceanographic event (winter wind-driven vertical mixing in the Gulf of Lion) has opposite impacts in close-by regions.

CHAPTER 3

Sensitivity and robustness of larval connectivity diagnostics obtained from Lagrangian Flow Networks

We study in this chapter the sensitivity and robustness of four LFN-derived connectivity metrics measuring retention and exchange. The most relevant parameters are tested over large ranges and a wide region with contrasting hydrodynamics: density of released particles, node size (spatial scale of discretization), Pelagic Larval Duration (PLD) and spawning modality. We find a minimum density of released particles that guarantees reliable values for most of the metrics examined. We also find that node size has a nontrivial influence on them. Connectivity estimates for long PLDs are more robust against biological uncertainties (PLD and spawning date) than for short PLDs. For mass-spawners releasing propagules over short periods ($\simeq 2-10$ days), daily release must be simulated to properly consider connectivity fluctuations due to variable currents. In contrast, average connectivity estimates for species that spawn repeatedly over longer durations (few weeks to few months) remain robust even using longer periodicity (5-10 days). Our results have implications to design connectivity experiments with particle-tracking models and to evaluate the reliability of their results.¹

3.1 Introduction

Even though marine connectivity has been studied from several approaches, it remains difficult and costly to evaluate [23]. Sparse observations of larval distribution do not provide enough information to infer broad-scale connectivity. Genetic methods provide estimate of connectivity, usually at long-evolutionary-time-scales, but costly sampling tends to allow only for poor spatial coverage, preventing the full description of spatial

¹This chapter is based on: Pedro Monroy, Vincent Rossi, Enrico Ser-Giacomi, Emilio Hernández-García and Cristóbal López. “Sensitivity and robustness of larval connectivity diagnostics obtained from Lagrangian Flow Networks”. *ICES Journal of Marine Science* 74.6 (2017), pp. 1763–1779.

connectivity patterns. In this respect, biophysical models are relatively affordable and extremely powerful to study and forecast dispersal patterns at different temporal and spatial scales. As such, a significant part of connectivity research employs numerical bio-physical models, especially particle-tracking (or Lagrangian) models, to characterize transport and dispersion in the ocean [e.g. 76, 112, 177, 3, 183, 87]. Despite the widespread use of these modelling approaches, there is still a poor knowledge of the key biological traits (i.e. spawning areas, larval duration, larval behavior and mortality rates) from which most model parameters are derived [23]. In addition, it is not clear how different parameter choices could affect connectivity estimates and their variability. Last, in spite of the recognized influence that ocean currents have on the connectivity of marine ecosystems, these processes remain difficult to evaluate due to their inherent chaotic, unpredictable and multi-scale properties. For instance, [76] reported that the transport patterns of anchovy eggs are most sensitive to changes both in areas and in months of release (along with the corresponding changes in circulation) than to variations in biological parameters. Other species-specific studies found that the temporal variability in circulation is crucial in modulating dispersal [138], while others found that biological processes crucially affect modelled connectivity estimates [e.g. 128, 129]. These examples evidence the complexity of simulating tightly coupled bio-physical processes and the importance of parametrization. It calls for further quantitative and systematic characterization of the intrinsic functioning and variability of these models.

With the growing use of connectivity models to estimate connectivity of a given organism, scientists realized the importance of assessing their robustness and sensitivity. Most existing studies focused on the evaluation of uncertainties associated with the underlying hydrodynamical model [e.g. 137] or of those related to changes in any bio-physical parameters (such as larval mortality, vertical migration, depth of dispersion, density and frequency of particle releases) but considering a specific species in a given oceanic region [e.g. 76, 129, 141, 78, 177, 34, 53, 89]. This implicitly means that those results would only be valid for the species and region of interest. In contrast, our objectives are to explore the sensitivity of connectivity proxies to the commonly used parameters over large ranges of values without restricting our analyses to a target species. We also focus on an extended and fully covered region (Mediterranean basin) examining systematically the influence of different discretization-scales on the spatio-temporal sensitivity of the aforementioned diagnostics.

To our knowledge, [166] is the only study analysing systematically the sensitivity of larval transport predictions to large ranges of three universal input parameters: the number of particles released, the particle release depth and the particle tracking time. They showed that larval transport predictions are sensitive to changes in all three input parameters and are dependent on the local mixing strength. While [166] is the first sensitivity analysis of larval transport of this broad type, it solely focused on a dozen of near-shore sites over a relatively small oceanic region (the Southern California Bight). Moreover, this investigation is restricted to two-dimensional vertically-integrated Particle Density Distributions (PDDs) and to the 2-dimensional grid-based descriptors of connectivity directly related to them (such as raw connectivity matrices, dispersal kernels, probability density functions and particle concentrations).

We aim here at studying the general robustness and sensitivity of four connectivity proxies derived from Lagrangian Flow Networks (LFNs) (Section 2.4). While this approach has been already applied in different contexts, the global robustness and sensitivity of metrics derived from LFNs have not been quantitatively assessed yet.

The four complementary connectivity proxies tested here measure the retention and exchange of larvae and are calculated by manipulating elements of the classical connectivity matrix and its binary equivalent (Section 2.4). Through their integrated analysis, they provide more information than, and are not directly comparable to, classical connectivity diagnostics mentioned previously [42]. In addition, we extend the results of [166] by focusing on all sites of a larger and more heterogeneous oceanic region, namely the Mediterranean basin, which cover a large range of flow patterns and mixing intensities.

In this chapter we assess the sensitivity and robustness of connectivity proxies derived from LFNs over the Mediterranean basin. After presenting briefly the LFNs methodology and reporting the statistical methods used, we explore the sensitivity of the four metrics to numerical parameters, namely the density of initial particles and the node-size (Section 3.3). Then, we evaluate the impact of biological parameters such as the PLD, simulated by the period of tracking, and the spawning dates, simulated by the starting times (Section 3.4). Indeed, from the perspective of marine ecologists, there are high uncertainties in the appraisal, based on field observations or laboratory experiments, of the key life history traits controlling connectivity. These include estimates of the PLD [98], of the modality of spawning [89], and of the depth of dispersion [32, 34]. The results are interpreted and discussed against existing literature and allow to make recommendations for future connectivity studies using particle tracking models and with foreseen impacts of such parameter choices on connectivity metrics.

3.2 Data and methods

Applying the LFNs to a given oceanic area requires the computation of Lagrangian trajectories of fluid particles (simulating passively drifting larvae) driven by an eddy-resolving velocity field of the region. Two-dimensional trajectories are obtained at a fixed depth through the integration of the velocity field, linearly interpolated in time and space, using a fourth order Runge-Kutta algorithm [158] with integration time step 1 day. All outputs presented here used the daily horizontal flow field generated by Copernicus operational model implemented in the entire Mediterranean Sea at $\frac{1}{16}^\circ$ horizontal resolution over 26 years (1987-2012) [120]. We retained the surface layer at 12 m because it is arguably the most turbulent flow field (ocean interior circulation becomes more sluggish) that is not directly influenced by wind drag (as is the very first surface layer). It means that our results are on the conservative side: computation at deeper layers would return similar or even more robust metrics than those computed at 12 m because of the reduced turbulence and variability. Integrating particles in three-dimensions and the very few trajectories that end up on land before the integration ends ("beaching") have barely detectable impacts on our results, as discussed in [148] and

[158].

Besides the oceanic domain of interest, the selected depth for deploying the particles and the corresponding velocity field, the main parameters required by the LFN methodology are the node size (i.e. scale of spatial discretization), the area density of particles released within every node, the spawning time(s) at which particles are released and the duration of tracking which simulates the Pelagic Larval Duration (PLD, i.e. time larvae drift with ocean currents). This chapter analyses the sensitivity of four connectivity estimates to those parameters varying over large ranges of variability, within the limits imposed by our settings (table 3.1). The four connectivity metrics were defined in Section 2.4, and are local retention (LR), self-recruitment (SR), source sink strength (SSs) and source sink degree (SSd).

Sensitivity tests and statistical methods

Sensitivity tests are performed for all tunable parameters which are distinguished in two types. The numerical parameters refer to the node size and the density of particles initially released in each node. We want to understand how those intrinsic parameters and their variations affect the computation of connectivity metrics with the LFNs. With respect to the biological parameters, we will focus on perhaps the most universal life history traits used in dispersal model: the PLD, the date and frequency of spawning. Note that our analyses are restricted to the parameters commonly employed in off-line particle tracking models, while we did not explore the resolution and parametrization of the velocity field and corresponding ocean model. Another relevant quantity attributed to each node is the surface proportion covered by land (land ratio). It distinguishes "fully oceanic" nodes from coastal ones. As an example, the land ratio of all nodes at 12 m depth are shown in Fig. 3.1.

Quantitative comparisons among pairs of different experiments (e.g. 2-dimensional fields of any of our four connectivity metrics generated with two different sets of parameters) are performed by computing Pearson correlation coefficient r . It provides an absolute scale to measure similarity of spatial distributions of connectivity metrics obtained varying one parameter: In general $0 \leq |r| \leq 1$, with $|r| = 1$ indicating a perfect linear correlation, and $r = 0$ absence of linear correlation. Since r compares the value of two discrete fields node by node, it is highly sensitive to changes in spatial patterns. Note that this can be a disadvantage when one wants to focus on temporal variability with small nodes because when pattern suffers a small translation or rotation in space while their values remain practically the same across two experiments, the resulting r will be small while the patterns are visually identical.

It is worth noting that Pearson correlation measures linear relationship, so that its use may be questionable if the variables being compared follow a different relationship. It is also sensitive to outliers that might lead to large effects on r value. In order to check linearity and presence of outliers, we visually inspect the cloud of points on the scatter-plots of corresponding metric values in each node (e.g. Fig. 3.2). Additionally we tested the non-parametric Spearman correlation (not shown) which is known to be

Sensitivity test	Parameter	Range value
Node size and particle density (total: 1729 experiments)	Starting dates	From 1 September 2010 to 30 November 2010, every 5 days
	PLD	60 days
	Particle densities (km^{-2})	0.026, 0.052, 0.259, 0.518, 1.037, 1.556, 2.07, 2.588, 3.109, 3.630, 4.159, 4.674 and 5.184
	Node sizes	1° , $3/4^\circ$, $1/2^\circ$, $1/4^\circ$, $1/8^\circ$, $1/10^\circ$ and $1/12^\circ$
	Depth	$-12m$
Starting time and spawning frequency (total: 364 experiments)	Starting dates	From 1 September 2010 to 30 November 2010, every day
	PLDs	30 and 60 days
	Particle density (km^{-2})	0.518 (i.e. 1600 and 100 particles per node of $1/2^\circ$ and $1/8^\circ$, respectively)
	Node sizes	$1/2^\circ$ and $1/8^\circ$
	Depth	$-12m$
Uncertainties in PLD estimates (total: 1200 experiments)	Starting dates	1 September and 1 October each year over 2001-2010
	PLDs	from 5 to 65 days, with daily increments
	Particle density (km^{-2})	0.518 (i.e. 1600 particles per node of $1/2^\circ$)
	Node size	$1/2^\circ$
	Depth	$-12m$

Table 3.1: Summary of experiments performed to assess the sensitivity of the model to

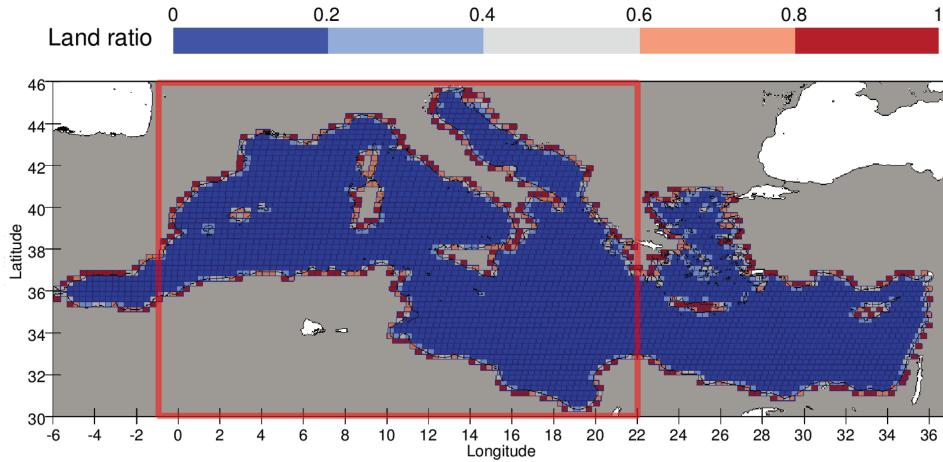


Figure 3.1: Grid used to construct the LFN of the Mediterranean Sea with node size of $1/4^\circ$ and labelling the nodes according to its land ratio at 12m. The discrete colour-scale represents the value of the land ratio and the black line is the 12m isobath from the ETOPO1 dataset. The interior of the red rectangle is the region used in all analyses except the one in Fig. 3.2.

more robust against outliers. We verified that our results are basically equivalent to the ones obtained with the Pearson correlation.

Over the range of parameter values upon which sensitivity is tested, a reference simulation should be chosen considering the optimal values that would return the "best" connectivity estimates. Then sensitivity experiments are generated by changing one parameter at a time and are finally compared against the reference. For instance, to explore the robustness of connectivity metrics to the density of particles, we chose the experiment using the largest number of particles as the reference simulation, as in [166]. Then, simulations obtained with decreasing number of particles are compared with the reference one.

Overall, the ensemble of numerical experiments performed are summarized in table 3.1 and are described in the following sections.

3.3 Numerical parameters

3.3.1 Number of released particles

We explore the sensitivity of connectivity diagnostics with respect to the density of particles initially released to determine the best compromise density that ensure robust estimates and reasonable computational cost. Simulations were conducted releasing particles every 5 days from 1 September 2010 to 30 November 2010 (a total of 19 starting dates) with a set of 13 different particle densities (spanning 0.02 up to 5.17 km^{-2}) and

7 different node-sizes (ranging $\frac{1}{12}^\circ$ - 1°). Details are reported in table 3.1. We use a PLD of 60 days for every simulation because it is considered as the longest integration time for which the 2-dimensional assumption (neglecting vertical movement) remains accurate [148]. Since longer PLD tend to favour long-distance dispersal [161], especially for passive larvae, it can also be considered as the "worst-case" scenario (i.e. results for shorter PLDs will return higher correlation coefficients, i.e. will be less affected by particle density).

We first investigate the cloud of points on the scatter-plots comparing all nodes of two simulations generated with different densities of particle released (Fig. 3.2), we observe that most nodes with the highest land ratios depart from the linear relationship. Those nodes are indeed coinciding with the boundaries of the hydrodynamical model (see Fig. 3.1). Since land ratio is related to initial number of particles per node², outliers are the few marginal nodes which have initially less particles than fully-oceanic nodes. Another issue is related to highly divergent oceanic areas: after a long integration time, the nodes located in such regions may end up with no particle at all, see figure 3.3. This also produces a sampling error in our metrics. As already mentioned by [42], this effect concerns essentially the Alboran Sea and, to a lesser extend, the Ierapetra wind-driven semi-permanent gyre (south of Cyprus).

In order to avoid the influence of these issues on our global analyses, we decided in the following to restrict our domain (see the red rectangle in Fig. 3.1) by excluding nodes whose longitude is $< 1^\circ\text{W}$ (removing the Alboran Sea) and $> 22^\circ\text{E}$ (removing the Ierapetra gyre), and excluding also the nodes with land ratio greater than 0.8. Note that this exclusion still keeps in the analyses the majority of the coastal nodes.

We compare each experiment to the reference configuration with the largest density of particles (5.17 km^{-2}) computing Pearson correlation for the four connectivity metrics. For every pairwise correlation corresponding to each specific pair of node-size and particle density, a temporal average was performed among the 19 different starting dates to compute standard errors. For each metric and node size, we obtain the minimum density of released particles that optimize robustness and computational cost of both metrics when correlation coefficients are above a certain threshold.

Sensitivity of the four metrics with respect to density of released particles is shown in figure 3.4. Instead of displaying Pearson correlation r versus particle density, we plot $1 - r$ versus number of particles per node. Thus, decreasing curves indicate that correlation improves with larger particle density. For all connectivity metrics, increasing the number of particles released per node returns higher r , so that $1 - r$ goes to 0. Moreover, the scaling of $(1 - r)$ with the number of particles released per node for the connectivity metrics LR , SR and SS_s is approximately a power law with exponent -1 independently of node-size (black line in Fig. 3.4). However, in the case of SS_d this dependence is more complex: it still decreases but slowly than the other metrics.

Based on this figure 3.4, one can estimate the minimum particle density required to

²Note that the seeding of particles only occurs in the vicinity of all effective grid points of the velocity field. In this way, we do not seed particles that will not be advected during the simulation (to avoid over-estimating retention).

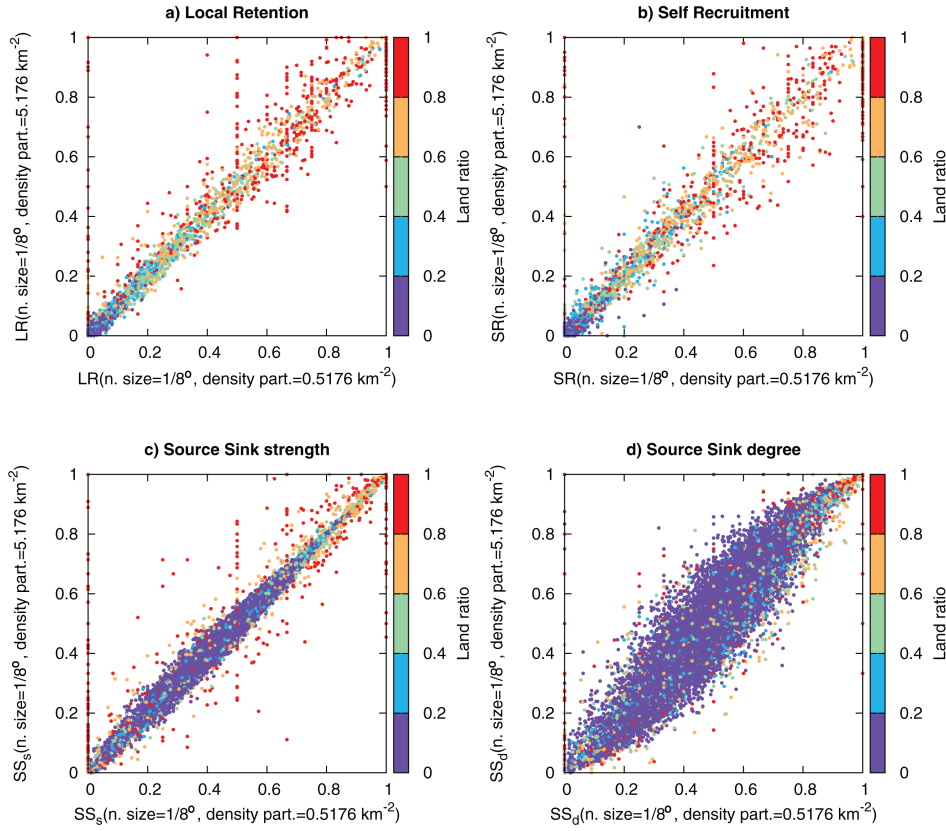


Figure 3.2: Scatter-plots for each connectivity metrics ((a) Local-Retention, (b) Self-Recruitment, (c) Source-Sink strength and (d) Source-Sink degree) among two LFN which only differ in particle density (0.518 and 5.176 km^{-2}). The other constant parameters are node-size= $1/8^\circ$, depth= 12 m , starting date is 16 October 2010 and PLD= 60 days. Colour represents the value of land ratio in the corresponding node.

obtain a robust result for each connectivity metric. We used a threshold of 0.95 for r ($1 - r = 0.05$ in Fig. 3.4) so that we consider the connectivity estimates to be insensitive to the number of particles released when r is greater than this value. We found a threshold of $\simeq 100$ particles per node for all node sizes when considering the metrics that are computed from the connectivity matrix (LR , SR and SS_s). Concerning SS_d , the thresholding procedure shows a dependence on the node size: values are reported in table 3.2.

The results show that the impact of the number of released particles on our different connectivity metrics has two different behaviours: SS_d improves with the number of particles slower than the other metrics. Moreover its scaling (i.e. the way in which the correlation with the reference case increases for larger particle number) depends also on the node-size, in contrast with the scaling of LR , SR and SS_s which depends only

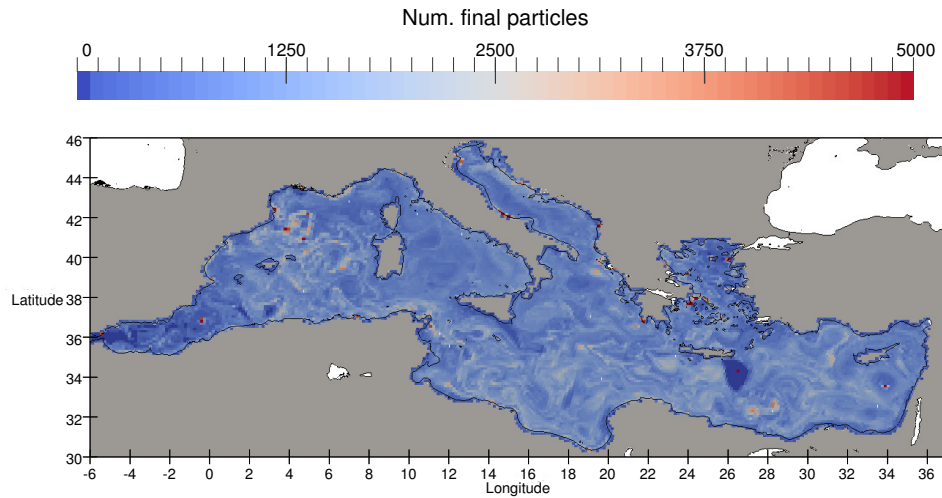


Figure 3.3: Number of particles in each node at the end of simulation for node-size= $1/8^\circ$, starting date = 1 September 2010, initial particle density = $5.176 km^2$ (i.e. 1000 particles at each node), depth = 12m and PLD = 60 days. Bathymetric contour (black line) at 12m depth.

Threshold ($r \geq 0.95$) for SS_d		
Node size ($^\circ$)	Particle density (km^{-2})	Number of particles per node
1	0.518	6400
3/4	0.518	3600
1/2	0.518	1600
1/4	1.037	800
1/8	1.037	200
1/10	1.556	$\simeq 190$
1/12	1.556	$\simeq 130$

Table 3.2: Minimum particle density and number of particles per node required to obtain a robust result for SS_d choosing a threshold of 0.95 in r . The thresholding procedure for the other metrics (LR , SR and SS_s) returns the single value of $\simeq 100$ particles per node, for any node-size.

on the initial number of particles per node. For our setup we find that 100 particles per node are sufficient to ensure the robustness of LR , SR and SS_s independently of node size. It is worth noting that this precise number may depend on other factors not included in this study: the characteristics of the underlying velocity field or the implementation of larval behavior (e.g. active vertical migration). Indeed, the exact number of particles to be released would depend on the ocean model used but the general laws we found (functional form of the improvement of correlation with particle number) still hold for any off-line particle model. However, the robustness threshold

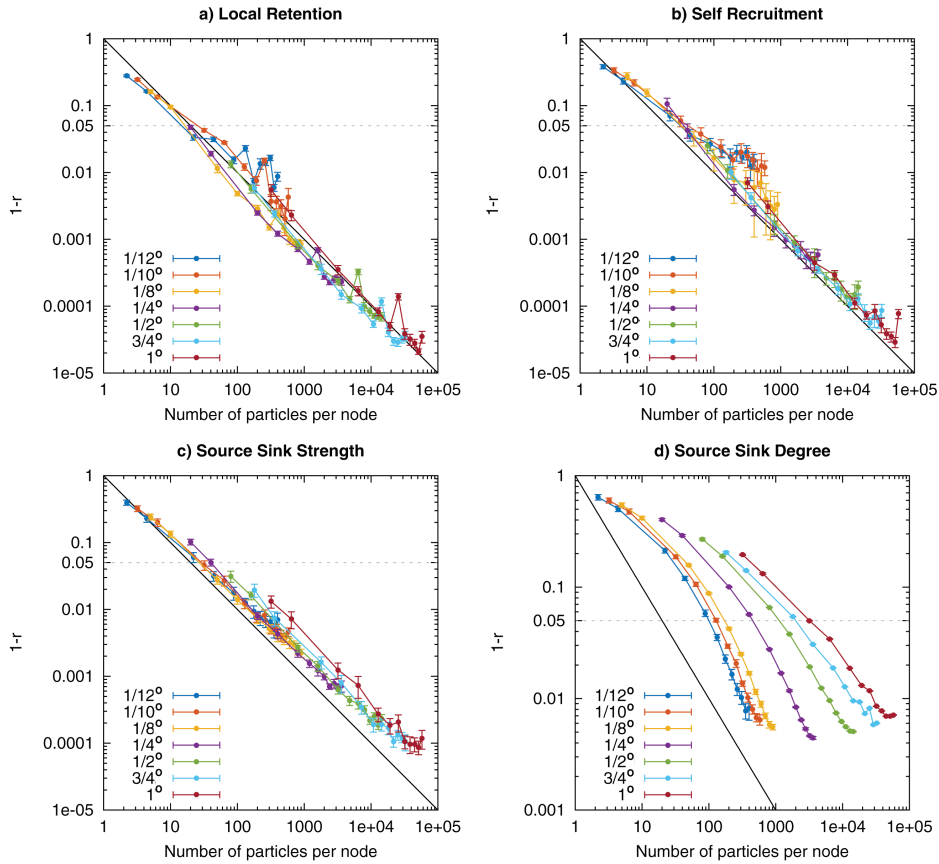


Figure 3.4: Initial particle density sensitivity tests for each connectivity metric: (a) LR , (b) SR , (c) SS_s and (d) SS_d . Colours represent different node-sizes, horizontal axis is the initial number of particles per node computed from LFN parameters (node-size and particle density) and vertical axis is the temporal average of $(1-r)$ among 19 starting dates. Pearson correlation coefficients r were calculated among every pair of node-size/particle-density and its reference pair, which has the same node-size and the highest particle density (5.176 km^{-2}). Parameters used are described in table 3.1. The error bars indicate the standard error of the mean and black line represents the function $1/(\text{Initial number of particles per node})$. The grey dotted line represent the threshold of 0.95 used to identify the recommended number of particles.

for SS_d depends on node size and remains greater than 100 particles (table 3.2) due to its different scaling. [166] also found a minimum number of particles which guarantees robustness in their model predictions. While they reported an exponential scaling of robustness with number of particles released, their results are not completely comparable to ours due to methodological differences. Our analyses focused on a PLD 60 days, however we stress that for shorter PLDs the recommended number of particles per

node would be lower than the threshold we propose. This is because the stochasticity of trajectories and the complexity of the circulation patterns experienced by particles decreased with tracking times (under the passive tracer assumption).

3.3.2 Spatial resolution discretization

The same set of simulations of previous study are also used to evaluate how the connectivity metrics are affected by the choice of node size (i.e. the spatial discretization to construct the connectivity matrix). We investigate differences in the spatial patterns of the four metrics when the node size of the network is changed. In fact, for such analysis, Pearson correlation can not be used because it assumes the same number of data-points for comparison, which means it can only be used for pairs of experiments with equal node-sizes.

Now we investigate the spatial variability looking at maps of the four metrics computed at a given time while varying the node size. A visual comparison between panels of figures 3.5, 3.6 and 3.7 is informative. Spatial patterns are finer for the high resolution discretization but large scale patterns still remain in lower resolutions. However, as the node size increased, the spatial variability decreased in exchange metrics (SS_s and SS_d), on the contrary, spatial variability decreases for higher grid resolutions in retention metrics (LR and SR) since the number of nodes with zero value increases.

Maps of the metric fields showed that more detailed patterns can be revealed using small nodes for both retention and exchange. Concerning LR and SR (Fig. 3.5), smaller nodes lead to non-zero values (red colors) essentially in nearshore and shelf regions, while those same retentive regions are less intense when considering larger nodes (i.e. which extend further away from continental shelves, thus encompassing the highly dispersive character of energetic boundary currents). This suggests that to obtain reliable estimates of larval retention, the scales of discretization (node-size) should be at least of the order of, or lower, than the mean width of the continental shelves. This is consistent with [19, 108] who uses high resolution computation to evidence high retention rates nearshore and over the continental shelves. Regarding the proxies of exchange, we stress that in large nodes the magnitude of exchange processes is slightly less important than in small nodes, therefore variability of values decrease. Note however that the relative range of values and the spatial patterns are similar among different node-sizes. The high robustness of SS patterns when increasing the coarse-graining of the system is related to the robustness of Lyapunov exponents [69]. Indeed, [158] demonstrated a relationship among such exponents and network measures used to compute the SS_d metrics. Note however that smaller nodes need higher computation costs, especially when interested in SS_d which requires the highest threshold of density particles per area (Table 3.2).

The choice of the node size has biological implications. As seen previously, it must be determined according to scales (e.g. basin versus local) and processes (retention or exchange) pertaining to the biological hypothesis to be tested. For instance, different parameter choices must be made if studying the dispersal of juvenile sea turtles across the entire Atlantic [137] or among a smaller region like the Balearic archipelago. Secondly,

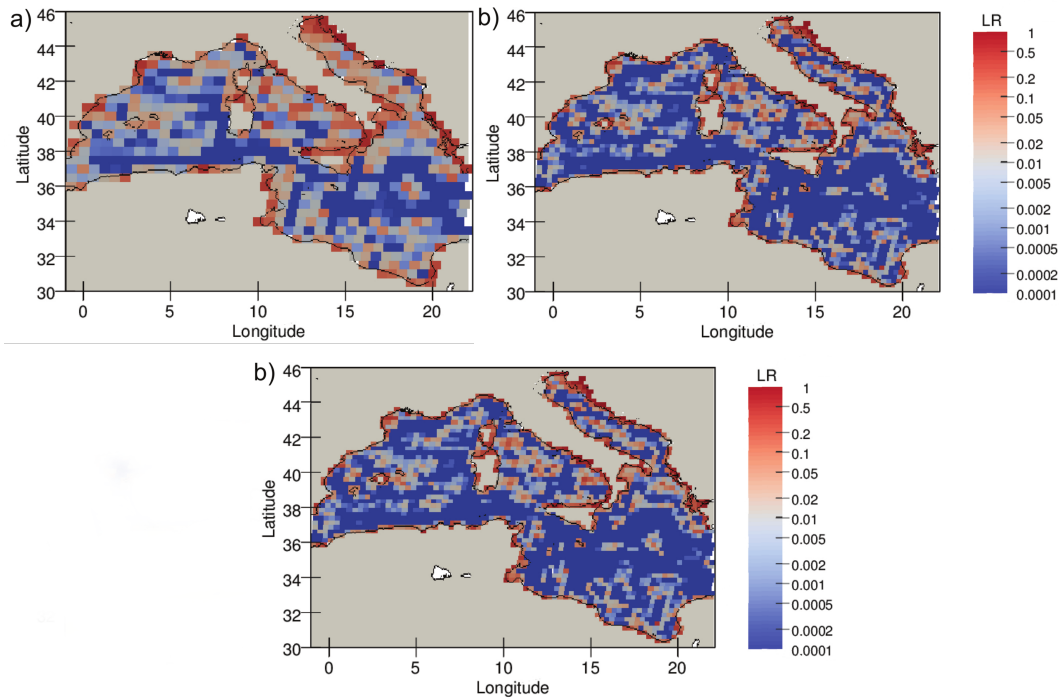


Figure 3.5: Maps of the Local Retention generated with particle density= 5.176 km^{-2} , starting date 15 November 2010, PLD=60 days and 12 m depth. Node size is: (a) $1/2^\circ$, (b) $1/4^\circ$ and (c) $1/8^\circ$.

one must consider the typical length-scales of fragmentation of the preferred habitat of the target species. For instance, small node sizes permit a better consideration of highly fragmented habitats (e.g. benthic habitats) and improved detection of small-scale dispersal patterns. However we also found that exchange metrics are highly dependent on the node-size, which affects the quantification of import/export from neighbouring patches. The importance of the choice of length-scales becomes even more relevant in seascape ecology (i.e. where no clear boundaries delimitate habitats). Indeed, [2] demonstrate that a combination of hydrographic variables and their spatial gradients improve their ability to model pelagic fish distribution only if they are calculated at the appropriate spatial scales. This means that to incorporate the quality of pelagic habitats within modelled connectivity estimates, the resolution of hydrographic variables and the spatial-scales at which they are averaged (i.e. node size) should be determined cautiously.

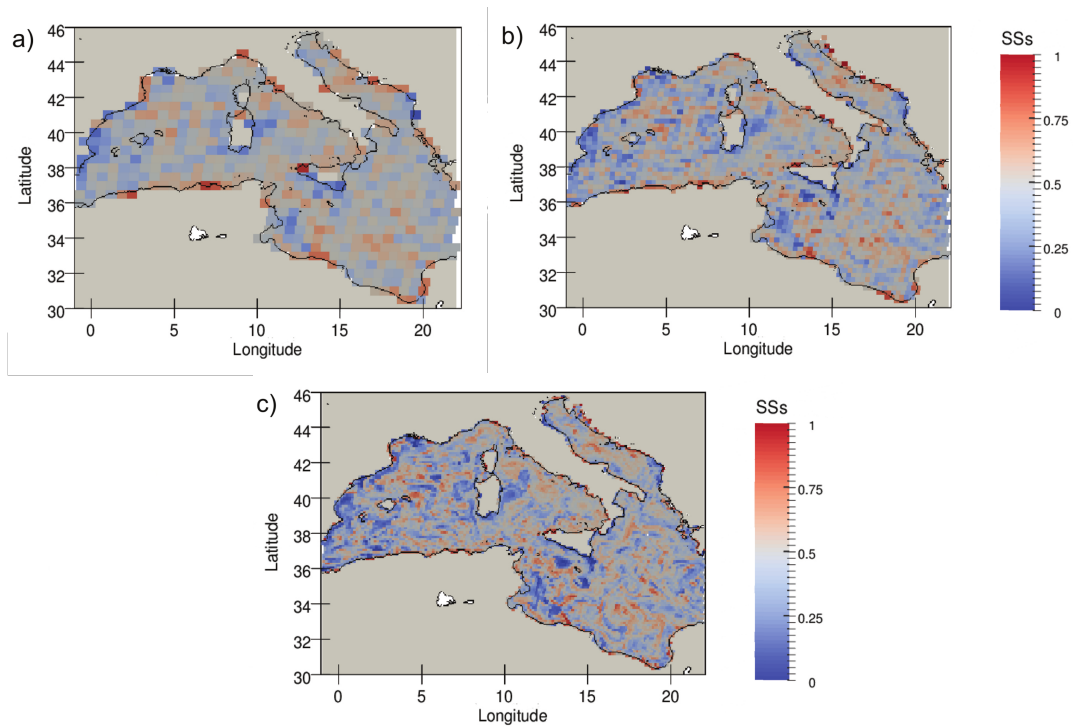


Figure 3.6: Maps of the Source Sink strength generated with the same parameters as in Fig. 3.5 (i.e. particle density= 5.176 km^{-2} , starting date 15 November 2010, PLD=60 days and 12 m depth). Node size is: (a) $1/2^\circ$, (b) $1/4^\circ$ and (c) $1/8^\circ$. Values close to zero imply a larval source whereas values close to 1 indicate larval sinks.

3.4 Biological parameters

3.4.1 Starting-date sensitivity

A common use of dispersal models in marine ecology is to evidence the temporal variability of connectivity of a given site [138, e.g.] or to discriminate geographical locations according to their mean connectivity [108, e.g.]. As such, the starting-date sensitivity study aims at quantifying how connectivity metrics change due to uncertainties in the day of one single spawning event. For this purpose, we compute the Pearson correlation coefficients for each connectivity metric node-by-node comparing pairs of experiments that only differ by their starting dates, maintaining a fixed time-lag (i.e. 2 events separated by a fixed number of days). To do this, we used an ensemble of simulations conducted with particles released every day from 1 September 2010 to 30 November 2010 (total of 91 spawning dates) using a PLD of 30 and 60 days, node size of $1/2^\circ$ and $1/8^\circ$ and the required particle density of 0.518 km^{-2} (see table 3.1). Over the total 91 experiments for a given node size and PLD, we compute average Pearson correlation and its standard error for 51 pairs of starting dates separated by time-lags spanning 1

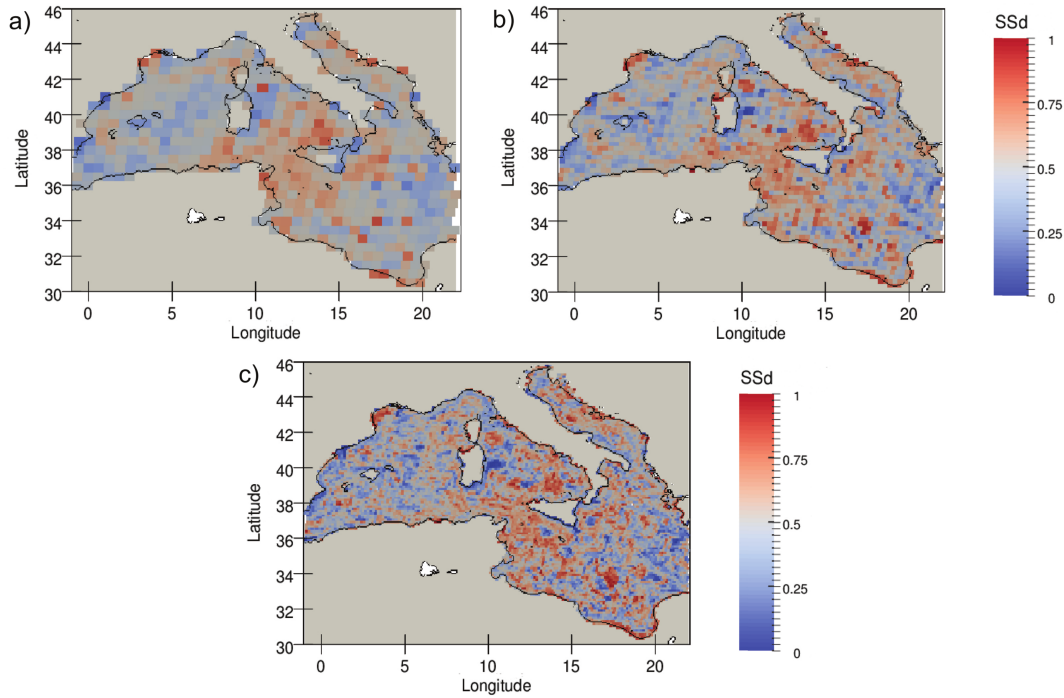


Figure 3.7: Maps of the Source Sink degree generated with the same parameters as in Fig. 3.5 (i.e. particle density= 5.176 km^{-2} , starting date 15 November 2010, PLD=60 days and 12 m depth). Node size is (a) $1/2^\circ$, (b) $1/4^\circ$ and (c) $1/8^\circ$. Nodes with values close to zero have a source character, whereas those with values close to 1 indicate a sink character.

to 40 days. We expect a decrease in correlation as the time lag between the two dates being compared increases.

Results of spawning date sensitivity study for node sizes of $1/2^\circ$ and $1/8^\circ$, using the two PLDs 30 and 60 days are shown in figure 3.8. Overall, Pearson correlation coefficients decrease when the time-lag between starting dates increases. For all metrics, one can distinguish two regimes with a quite rapid decrease during the first 8 to 15 days and then a rather slow linear decrease of the correlation until time lag matches with PLD value. At time lags higher than PLD the correlation stabilizes, however, our time-lag range only allows us to observe this for the PLD of 30 days. Note also that while the retention indices (LR and SR) remain quite robust (coefficients spanning 0.55 - 1), the exchange indices reveal higher dependence (SS_s and SS_d) with respect to spawning times with r falling down to 0.2 or lower for lag-times of 40 days. There are not large differences between both PLDs but it is worth noting that shorter PLDs are more sensitive to the spawning date for all metrics. We observe also that for larger node sizes the robustness to spawning-date variations increases for exchange metrics but decreases for retention ones.

The sensitivity study to spawning date highlighted that retention metrics are always

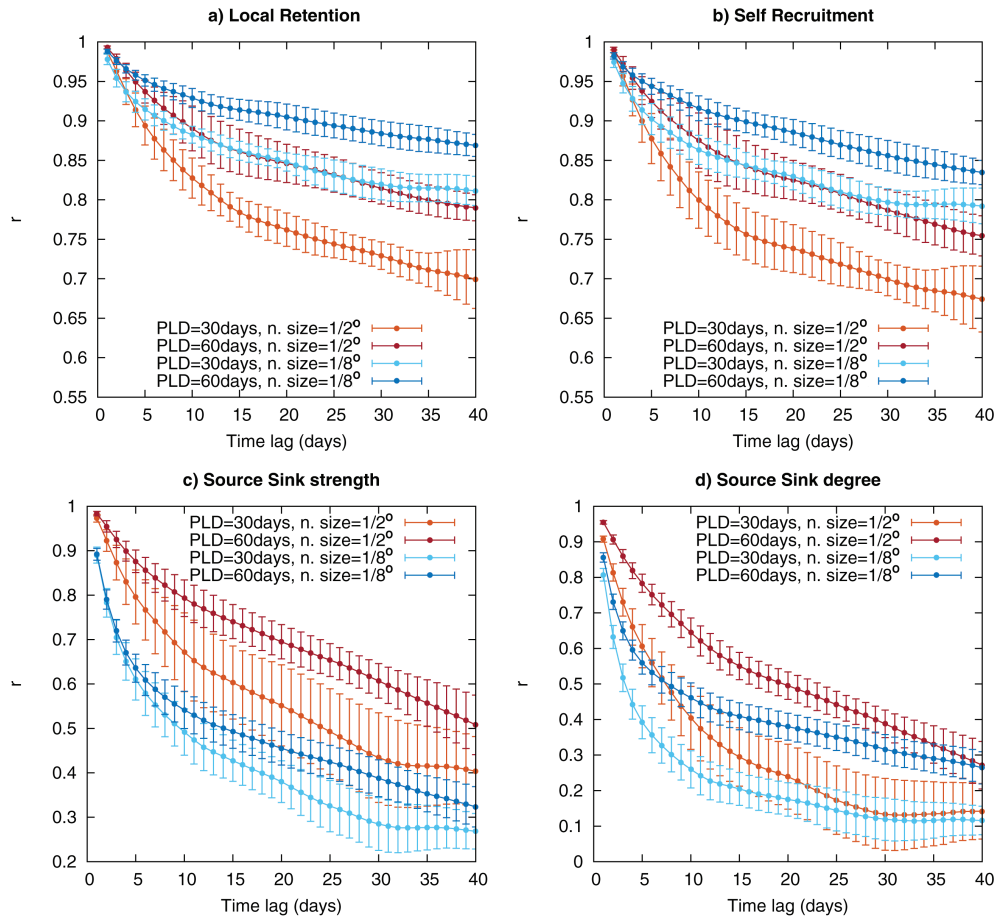


Figure 3.8: Starting-date sensitivity tests for each connectivity metric: (a) LR , (b) SR , (c) SS_s and (d) SS_d . Colours represent node-size and PLD, horizontal axis is the time-lag and vertical axis is the temporal average of r among 51 starting dates (1 September to 21 October 2010). Pearson correlation r was calculated among every pair of connectivity metric fields obtained from parameters that only differ in starting dates by the indicated time-lag. The error bars indicate the standard deviation among the set of coefficients obtained.

more robust than exchange ones. We also found two regimes for all PLDs and node-sizes studied. This can be explained by the temporal correlations of Lagrangian velocities. In the first regime, velocities are correlated among the reference simulation and lagged ones, this generates a fast decay of correlations, since it produces oriented changes in spatial patterns. The second regime is characterized by uncorrelated velocities which causes the slow down of pairwise correlations due to random variations of spatial patterns. The time lag at the transition between both regimes can be estimated by the Lagrangian correlation time [174], i.e. the time at which the Lagrangian velocities start to be uncorrelated. We found here that the second regime starts approximately at time-lag

of 10 days, which is greater than the Lagrangian correlation times of about 2-5 days in the ocean [134, 14]. This discrepancy might be due to that fact that for time lags larger than the Lagrangian correlation time, velocities can still be correlated at particular locations, especially due to mesoscale features (e.g. larvae trapped within eddies) [44, 19]. Looking at PLDs of 30 days, the existence of a third regime is suggested when the time-lag becomes greater than the PLD (correlation coefficients are constant and low). It could mean that the pair of experiments are statistically equivalent, therefore there is no causality between both simulations that do not overlap temporally. We only observe this for one tested PLD because the maximum time-lag used here is kept below 60 days. Therefore additional studies, preferentially in three-dimensions, are needed to further explore longer time-scales.

Correlation of connectivity metrics obtained with lagged spawning dates revealed that they are significantly more robust for longer PLD. Therefore, the uncertainties about the spawning dates for a short-PLD species will largely affect the results, whereas the same level of uncertainty for a long-PLD species will have limited impacts.

The influence of node size on the robustness of spawning date depends on the metric considered. Exchange metrics (SS_s and SS_d) are more robust when node-size increases, independently of the time-lag. On the contrary, retention metrics (LR and SR) are more robust when node size decreases. As we discussed previously (sect.), node size rules the spatial variability of retention and exchange: larger nodes return more variable retention processes, hence retention metrics are less robust, and smaller nodes increment the rate of exchanges resulting in a weaker robustness for exchange metrics.

3.4.2 Spawning frequency

Next we explored the sensitivity to spawning frequency. We consider as the reference simulation an hypothetical organism that would spawn every day during 3 months. We choose a daily spawning because is the temporal resolution of the hydrodynamic model and a duration of 3 months to explore a wide range of frequencies. Our objectives are then to evaluate the errors made on the estimation of both the mean and the standard deviation of our four connectivity metrics using lower spawning frequencies. The simulations are the same as for the spawning-date sensitivity study (see table 3.1): connectivity metrics are computed every day from 1 September 2010 to 30 November 2010 (91 spawning dates). As in the previous case, node-size and PLD are fixed when we calculate the temporal averages of the four metrics locally (node-by-node). For all node sizes, PLDs and spawning frequencies we computed the mean relative error (MRE) averaged over all the nodes with respect to the reference value obtained with daily spawning:

$$MRE(f_S) = \sqrt{\frac{1}{N} \sum_{i=1}^N \left(\frac{CM_{f_S}^i - CM_{f_D}^i}{CM_{f_D}^i} \right)^2}. \quad (3.1)$$

Where CM is one of the four connectivity metrics, f_D and f_S are the daily frequency and the spawning frequency being tested, respectively. The sum runs over the total N nodes (or geographical sites).

We now explore how our ability to significantly differentiate sites according to their simulated connectivities is affected by the spawning period. We used the same simulations as for the previous sensitivity studies and we fixed PLD, node size and the frequency of spawning to compare the connectivity of all pairs of nodes using the Kruskal-Wallis test (KW). This is a non-parametric version of one-way ANOVA, which tests whether both samples originate from the same distribution (in other words, if the connectivity properties of both nodes can be considered equal). Our reference is the total number of discriminated sites based on an hypothetical organism that spawn every day over 3 months. We then study how the total number of discriminated sites (i.e. the number of pairs of sites which have different connectivity properties according to the KW test) decreases when the spawning period increases for different significance levels.

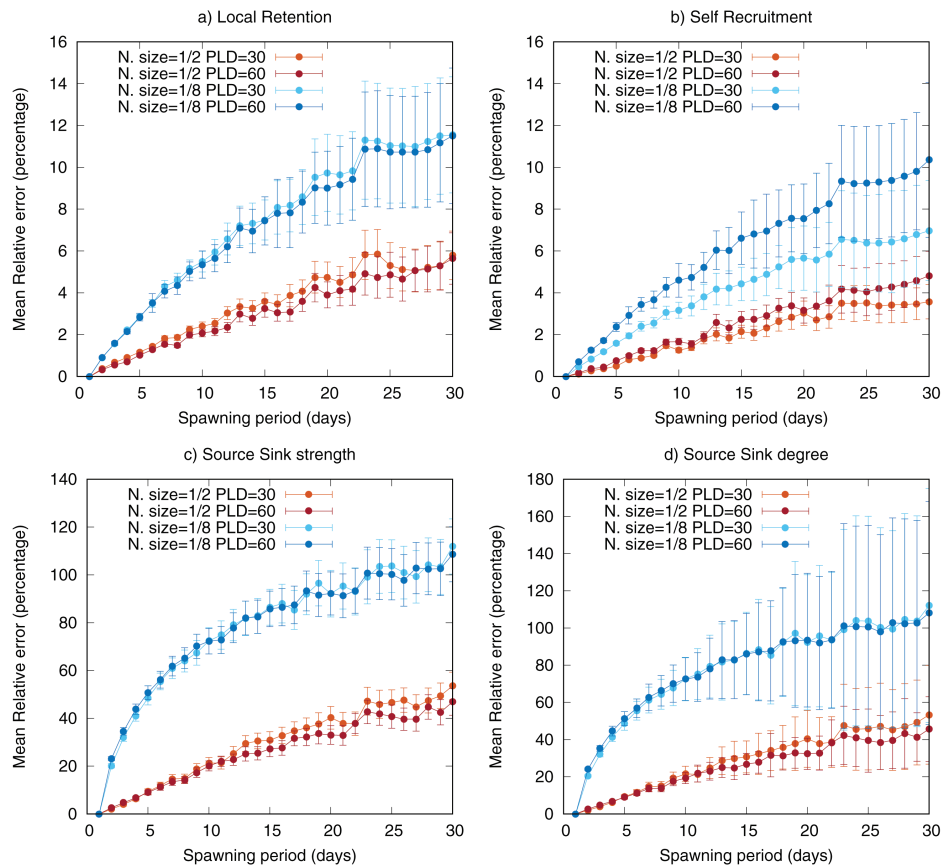


Figure 3.9: Spawning-frequency sensitivity tests. Mean relative error (MRE, Eq. (3.1)) for each connectivity metric: (a) LR , (b) SR , (c) SS_s and (d) SS_d . Colours represent node-size and PLD as indicated in the legend. The horizontal axis is the period of spawning (inverse of spawning frequency). The vertical axis is the MRE (expressed as a percentage). Lines indicate the MRE of the mean values while error bars represent the MRE of their standard deviations. The reference simulation with respect to which errors are computed is one of daily spawning.

Results of the spawning-frequency sensitivity study are shown in figure 3.9 and 3.10. Overall, the errors made when estimating the mean connectivity and its fluctuation as compared with the reference case of daily spawning increase with spawning period (Fig. 3.9). Mean Relative Error (MRE) is always larger (about one order of magnitude) in retention metrics than exchange ones. PLD has very little influence on the MRE for all the frequencies examined, but larger node sizes tend to produce lower mean relative errors. For instance, if one uses a node size of $1/8^\circ$ and a spawning period of 10 days over 3 months to study our hypothetical species, the mean connectivity estimates of retention will have errors (with respect to the reference daily spawning) of about 5% while exchange metrics will have errors of 50 to 100%, independently of its PLD.

When investigating the percentage of pairs of sites that can be statistically distinguished by their connectivity-metric distributions we see that it decreases with the spawning periodicity (Fig. 3.10 plots this percentage relative to the value for daily spawning). Note that this percentage decreases substantially slower for the retention metrics than for the exchange metrics, while SS_d has the faster decay. In this case, the PLD has an influence: long PLDs resulted in an increase (marked in SS_s and SS_d) of the number of discriminated pairs.

The sensitivity to spawning frequency was studied from two perspectives: we first studied how decreasing the spawning frequency with respect to a reference case of daily spawning increases the errors in the estimates of connectivity estimates for each node; then we investigated how the ability to differentiate distinct geographical sites by their connectivity properties decreases when spawning period is increased. We found that, with increasing spawning periodicity, errors grow slower in retention proxies than in exchange proxies (about one order of magnitude). This is consistent with our previous results and it suggest that changes in retention processes are primarily spatially-driven, i.e. controlled by the bathymetry that constrains the local currents. In contrast, temporal variability is very high in exchange metrics, so that high frequency must be considered to properly describe them. We also found that PLD has very little influence on metrics errors when the spawning period is lower than the PLD itself. Furthermore, increasing node size always decrease errors in both retention and exchange metrics.

We showed that increase in the spawning period affects negatively the statistical discrimination of sites with distinct connectivity properties. This is in line with [89] who found that spawning periodicity exerts a control on the number and persistence of network connections among distant sub-populations. This negative influence is considerably less intense in retention metrics than exchange ones. It reinforces our previous statement: any retention proxies display lower temporal variability than exchange metrics. By combining our conclusions derived from Fig. 3.9 and 3.10, we found that, when increasing the periodicity, small relative errors in retention metrics have relatively large negative impacts on the discriminations of sites. In contrast, large relative errors made on exchange metrics could still allow to discriminate sites properly. This has to do with the distinct levels of spatial and temporal variability of retention and exchange metrics [138], which are directly related to the intrinsic properties of the velocity field, and thus of the hydrodynamical model.

This spawning-frequency study has biological implications: if a given species is known

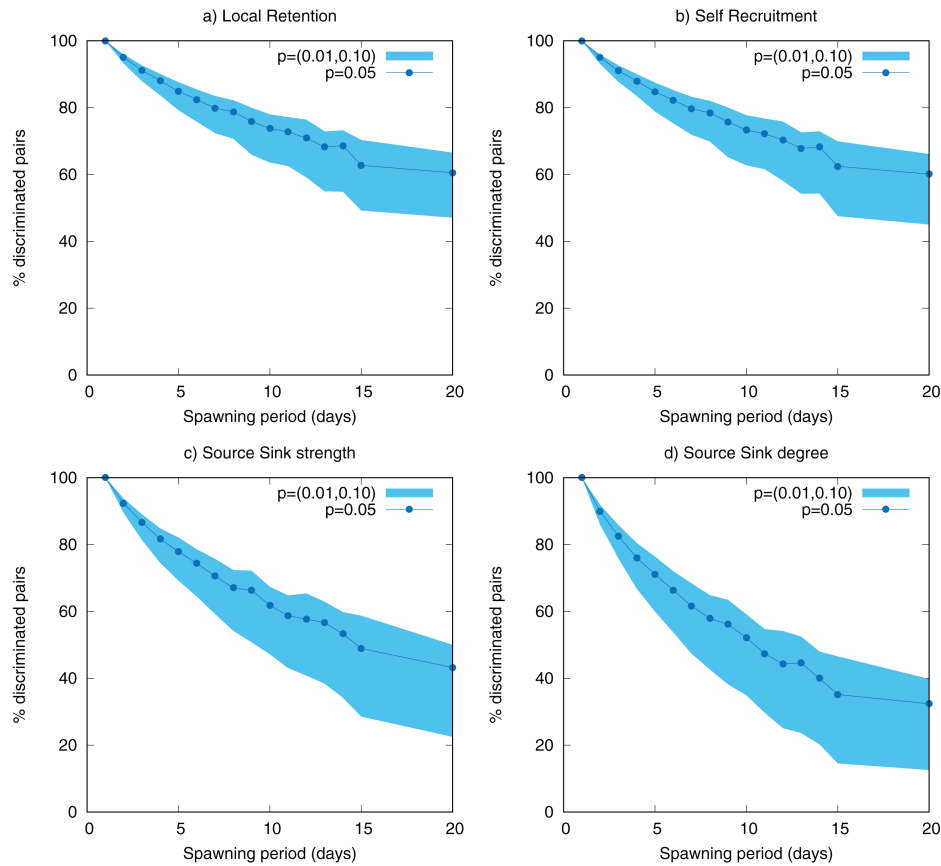


Figure 3.10: Percentage of discriminated pair of sites (normalized by the number of pairs discriminated using daily spawning frequency) as a function of spawning period for the following metrics: (a) LR , (b) SR , (c) SS_s and (d) SS_d . Blue curves represent the 0.05 significance level of the Kruskal-Wallis tests; upper and bottom contours correspond to 0.10 and 0.01 significance levels, respectively. Simulations used here are those of the spawning-frequency test (table 3.1), with node size of $1/2^\circ$ and PLD of 60 days. The decreasing curves indicate that the statistical properties of different sites become more difficult to distinguish for larger spawning period.

to spawn continuously over a 3-months period, similar mean connectivity estimates will be obtained when considering daily spawning or periods of 5 to 10 days. In other words, for a species known to spawn repeatedly over long period of a few months, using a periodicity of 5 to 10 days will still allow discriminating sites by their mean rates of larval retention and exchange. This is consistent with [76] who reported similar transport success for a PLD spanning over 15 days to 2 months when using periods ranging from 1 to 10 days. [167] argued that connectivity fluctuations (i.e. the temporal variability of ocean currents echoing on the variability of connectivity) would affect more

the seasonal spawners than the year-round spawners. Our results do not support this hypothesis since the 10 days threshold would apply to most oceanic regions and seasons. Nevertheless, it is also clear that the level of connectivity fluctuations highly depends on the sites and periods considered. Indeed, there exist oceanic areas e.g. the lagoon system of [34] for which higher spawning frequencies (i.e. spawning periods smaller than one day) are required to take into account rapidly changing flow fields (e.g. tidal currents, sea-breeze induced circulation, short-living sub-mesoscale fronts and eddies, etc...). Besides, our study suggests that the most precise connectivity estimates for given pairs of location/period could be attained by assessing a-priori the characteristic spatial and temporal variability scales of the flow and by selecting parameters accordingly. This is because, despite the stochasticity of the ocean circulation, there are locations and periods which have relatively stable dynamical properties, such as its level of turbulence (that could be evaluated through its eddy kinetic energy or Lyapunov fields) and its divergent/convergent character, thus resulting in quite constant connectivity patterns (see [42]).

3.4.3 PLD sensitivity

Finally we test how uncertainties on the PLD would impact the modelled connectivity estimates when considering a single-day spawning event. To do this, we performed simulations releasing particles on 1 September and 1 October every year over 2001-2010 (total of 20 starting dates) with PLD ranging from 5 to 65 days. Tracking times over 65 days are not tested because the 2-dimensional assumptions becomes inaccurate at longer time-scales [148]. Particle density was fixed to 0.518 km^{-2} and node-size $1/2^\circ$ (see table 3.1). Pearson correlations were computed for the four connectivity metrics by comparing all pairs of experiments differing by their PLDs (but using the same starting dates) and then by averaging the Pearson coefficients. In this way we measure the influence of all the possible positive and negative PLD deviations within our range of PLDs (60 values, and 3600 pairwise comparisons).

Results of the PLD sensitivity study are shown in figure 3.11. The four connectivity metrics reveal different behaviour. The exchange proxies SS_s and SS_d are considerably less robust to variations of the PLD than the metrics measuring retention (see the area enclosed between the $r = 0.9$ black contours, Fig. 3.11). Another interesting result is that uncertainties of a few days for long PLDs have less impact than a few-days uncertainty for small PLDs, as evidenced by the conical structures visible of isolines in all subplots of Fig. 3.11, especially marked within LR and SR .

Concerning the sensitivity to the PLD, we observe that correlations decrease when the PLD is shifted from a reference PLD. However, the rate of decrease for retention metrics revealed stronger dependence on the reference PLD than for exchange diagnostics. While it is well known that long PLDs increase mean dispersal distances of propagules and decrease their retention [53], the effects on exchange diagnostics may be not straightforward. We also found that relative errors in connectivity estimates due to uncertainties on the PLD are smaller for long PLD (Fig. 3.11). This means that if the mean PLD of

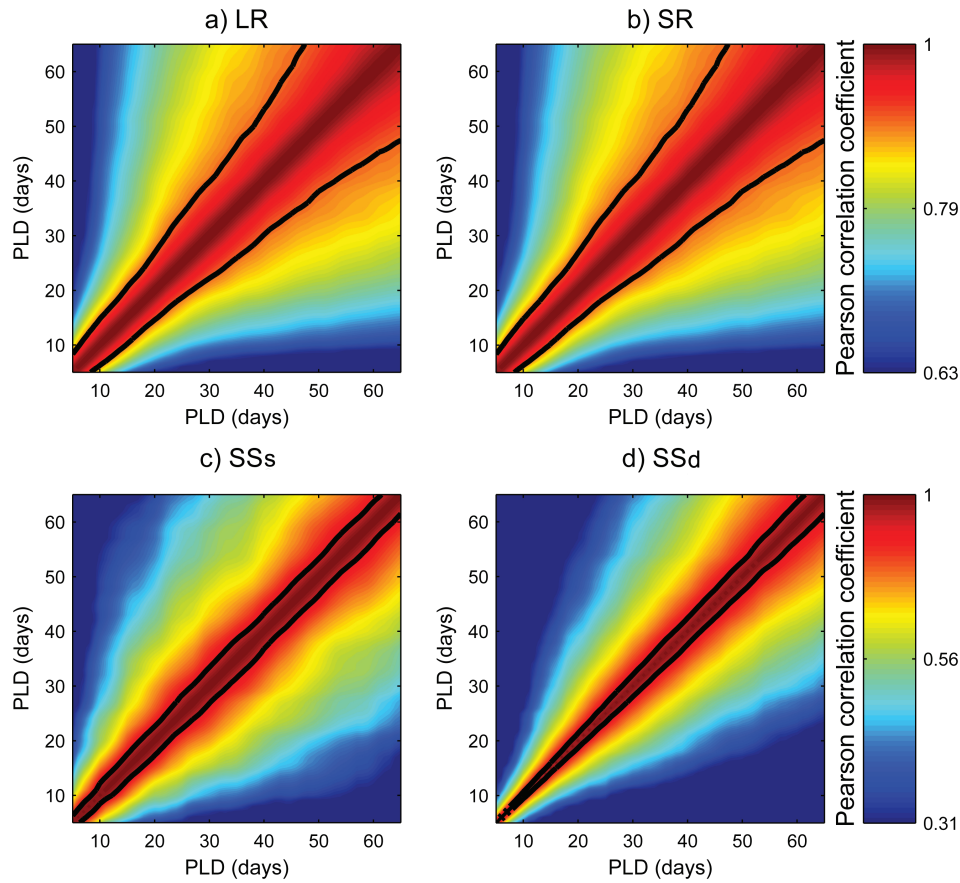


Figure 3.11: Results of PLD sensitivity test for each connectivity metric: (a) LR , (b) SR , (c) SS_s and (d) SS_d . The color represents Pearson correlation among two simulations that only differ by their PLD (in days, given by both axis). Black lines contour the 0.9 level. The temporal averaging concerns 20 starting dates, i.e. 1 September and 1 October over 2001-2010. Other parameters are: particle density of 0.518 km^{-2} (i.e. 1600 per node) and node-size $1/2^\circ$ (see table 3.1).

a given species is $50 \text{ days} \pm 10 \text{ days}$, the computation of retention indices will be very similar using 60 or 40 days tracking time (the corresponding pair or r -values falls within the black contours of Fig. 3.11). In contrast, for a given species with a mean PLD of $15 \text{ days} \pm 10 \text{ days}$, retention rates will be significantly different for PLDs of 5 or 25 days (outside the black contours in Fig. 3.11). This is consistent with [166] who found that the sensitivity of particle density distribution to PLD is much larger for short tracking times ($\leq 15 \text{ days}$) than for long tracking times ($\geq 20 \text{ days}$). We also demonstrated that this robustness effect does not hold for exchange metrics. It is worth noting that for PLD uncertainties lower than the characteristic time-scale of the flow (i.e. \pm a few days around the reference PLD), exchange metrics remain constant because the convergence of the flow is almost unchanged at these time-scales.

3.5 Other factors not considered

While some species-specific factors were not included in our sensitivity studies, they have the potential to affect connectivity estimates and their robustness. We did not explicitly test the sensitivity of our metrics to the depth of dispersion because it would depend on the location and season of the oceanic region of interest, as well as on the mixing parametrization of the hydrodynamical model. In the Baltic sea, [32] found that the depth distribution of larvae critically affects their dispersal. Along the Chilean coasts [53] found that retention increases with depth since currents are generally weaker and often shoreward. [166] suggested that the robustness of the depth of dispersion on connectivity estimates is proportional to the strength of vertical mixing. In other words, summer well-stratified water are usually dominated by baroclinic currents so that connectivity estimates are sensitive to the depth of dispersion. In contrast, winter-time deep-mixed layers waters and weak stratification favour barotropic flow in which connectivity estimates are less sensitive to the depths of dispersion.

In the Mediterranean Sea, [176] observed in spring that most fish larvae are concentrated in the surface mixed-layer, that is between 20 and 50 m thick. This is consistent with [186] who reported surface mixed-layer of less than 50 m in summer and about 100 m during winter or even more in specific areas of deep-water formation. It suggests that connectivity estimates during summer might be very similar in the top 50 m, extending down to 100 m in winter. This is consistent with [104] who argued that mesoscale processes (whose magnitude is governed by atmospheric seasonal forcing) control aggregation and dispersion processes in the north-west Mediterranean sea. Note that from a more global perspective, [171] proposed a simplified classification of fish eggs as pelagic (0-50 m), mesopelagic (150-250 m) and bottom eggs (250-350 m, or the bottom of the shelf). Since dispersal at various depths can be examined by selecting the corresponding vertical layer of the model, it will become possible to test this effect globally.

Another factor that was not tested here but that might affect connectivity estimates is the representation of small-scale (sub-mesoscale and below) structures in the simulated velocity fields. Indeed, [137] indicated that the use of non-eddy-resolving model outputs to compute drifting trajectories yields predictions that are inconsistent with observations. To circumvent this issue, it is common to add a random component (or random walk) to the particle trajectories to reproduce this non-resolved turbulence. [139] found that adding a random-walk term to the trajectories calculated with an eddy-resolving model does not mitigate the errors introduced by the temporal averaging, at least for regional to large-scale focus. By adding noise to trajectories or by smoothing a given velocity field, [69] investigate the effect of the effective horizontal resolution of the simulated currents and found small impacts on the computation of Lyapunov exponents. We expect the same levels of robustness for our connectivity metrics because network measures (such as degrees, which allows the computation of SS_d) are physically related to the Lyapunov exponents field [158]. Concerning the vertical dimension, [166] reported that the addition of vertical sub-grid scale mixing does not alleviate the sensitivity of trajectories to the depth of dispersion. Although the two latter studies advocate for a small impact of sub-

grid mixing to connectivity estimates, further studies are needed, especially considering the growing development of very high-resolution hydrodynamical models.

Last, the implementations of complex larval behaviour, mortality or success of settlement e.g.[94, 130] as well as three-dimensional trajectories [87] are not studied here but are envisaged for future development. While [52] reported that vertical migration is a biological factor that significantly influences connectivity patterns, it is likely it would be so primarily in systems characterized by strong vertical shear e.g. coastal upwelling [141, 19]. Another relevant process is the propagule buoyancy (e.g. changing mass density of eggs during its early-life stages) which has been found to significantly affect transport success of anchovy eggs [128] but not in the larvae of a sessile gastropod [51]. This example clearly suggests that the effect of those fine biological parametrizations on connectivity are highly species-specific.

CHAPTER 4

Modeling the dynamical sinking of biogenic particles in oceanic flow

This chapter addresses the problem of sinking particles in a realistic oceanic flow, with major energetic structures in the mesoscale, focussing in the range of particle sizes and densities appropriate for marine biogenic particles. Our aim is to evaluate the relevance of theoretical results of finite size particle dynamics in their applications in the oceanographic context. By using a simplified equation of motion of small particles in a mesoscale simulation of the oceanic velocity field, we estimate the influence of physical processes such as the Coriolis force and the inertia of the particles, and we conclude that they represent negligible corrections to the most important terms, which are passive motion with the velocity of the flow, and a constant added vertical velocity due to gravity. Even if within this approximation three-dimensional clustering of particles can not occur, two-dimensional cuts or projections of the evolving three-dimensional density can display inhomogeneities similar to the ones observed in sinking ocean particles.¹

4.1 Introduction

The sinking of small particles suspended in fluids is a topic of both fundamental importance and of practical implications in diverse fields ranging from rain nucleation to industrial processes [111, 46].

In the oceans, photosynthesis by phytoplankton in surface waters uses sunlight, inorganic nutrients and carbon dioxide to produce organic matter which is then exported downward and isolated from the atmosphere [68], a process which forms the so-called biological carbon pump. The downward flux of carbon-rich biogenic particles from the marine surface due to gravitational settling, one of the key process of the biological carbon pump, is responsible (together with the solubility and the physical carbon pumps) of much of the oceans' role in the Earth carbon cycle [152]. Although most of the organic

¹This chapter is based on: Pedro Monroy, Emilio Hernández-García, Vincent Rossi and Cristóbal López. “Modeling the dynamical sinking of biogenic particles in oceanic flow”. *Nonlin. Processes Geophys.* 24 (2017), pp. 293–305.

matter is metabolized and remineralized in surface waters, a significant portion sinks into deeper horizons. It can be sequestered on various time scales spanning a few years to decades in central and intermediate waters, several centuries in deep waters and up to millions of years locked up in bottom sediments [38]. Suitable modeling of the sinking process of particulate matter is thus required to properly assess the amount of carbon sequestered in the ocean and in general to better understand global biogeochemical cycling and its influence on the Earth climate.

This is a challenging task that involves the downward transport of particles of many different sizes and densities by turbulent ocean flows which contain an enormous range of interacting scales. In the oceanographic community, numerous studies approached this problem by considering biogenic particles transported in oceanic flow as passive particles with an added constant velocity in the vertical to account for the sinking dynamics [163, 164, 140, 150, 156]. They suggest that the sinking of particles may not be strictly vertical but oblique, meaning that the locations where the particles are formed at the surface may be distant from the location of their deposition in the seafloor sediment. Then [164] presented the concept of statistical funnels which describe and quantify the source region of a sediment trap (subsurface collecting device of sinking-particles used to get estimate of vertical fluxes). The validity of this approximation and the influence of different physical processes is however poorly discussed in these analyses.

In the physical community, the framework to model sinking particles is based on the Maxey-Riley-Gatignol equation for a small spherical particle moving in an ambient flow [107, 54, 111, 135, 26], which highlights the importance of mechanisms beyond passive transport and constant sinking velocity, such as the role of finite size, inertia and history dependence. A major outcome of these studies is that inhomogeneities and particle clustering can arise spontaneously even if the fluid velocity field is incompressible and particles do not interact [169]. Particle clustering and patchiness is indeed observed in the surface and subsurface of the ocean [96, 20, 113]

Here we consider the theory of small but finite-size particles driven by geophysical flows, which is, as mentioned above, conveniently based on the Maxey-Riley-Gatignol equation. In Sect. 4.2 we review the main characteristics of marine particles which are relevant for their sinking dynamics. In Sect. 4.3 we present the equations of motion describing this process, together with the approximations required to obtain them and the type of particles for which they are valid. In particular, we discuss its validity and the relevance of the different physical processes involved in the range of sizes and densities of marine biogenic particles. In Sect. 4.4 we use these equations to study the settling dynamics in a modelled oceanic velocity field produced by a realistic high-resolution regional simulation of the Benguela upwelling system (southwest Africa). We estimate the relevance of physical processes such as the Coriolis force and the inertia of the particles with respect to the settling velocity. We also observe the spatial distribution of particles falling onto a plane of constant depth above the seabed and we identify clustering of particles that is interpreted with simple geometrical arguments which do not require physical phenomena beyond passive transport and constant terminal velocity.

4.2 Characteristics of marine biogenic particles

In theory, the sinking velocities of biogenic particles depend on various intrinsic factors (such as their sizes, shapes, densities, porosities) which can be modified along their fall by complex bio-physical processes (e.g. aggregation, ballasting, trimming by remineralisation) as well as by the three-dimensional flow field [170]. However reasonable estimates of the effective sinking velocities of marine particles can be obtained by taking into account only its size and density [109]. In our Lagrangian setting we thus consider that the two key properties of marine particles controlling their sinking dynamics are their size and density. Here we present the standard classification of marine particles according to the typical range of size and density by compiling different bibliographical sources.

4.2.1 Size

Because of the diversity of the shapes, the size of a particle refers to the diameter of a sphere of equivalent volume (Equivalent Spherical Diameter) [56]. The size of marine particles ranges from 1 *nm* (almost-dissolved colloids) to aggregates larger than 1 *cm* [170].

Originally, the size classification of particles was based on the minimal pore size of the nets used for their collection, which is about $\simeq 0.45 - 1.0 \mu\text{m}$. Any material larger than $0.2 \mu\text{m}$ (thus isolated by the filtration of seawater) is regarded as particulate organic matter, while the fraction that percolates through the filter is labelled as dissolved matter. This includes colloidal and truly dissolved materials (see Fig. 4.1). Although this discrimination of the size-continuum observed in the real ocean is somehow arbitrary, it is useful –and we will follow it– because particles smaller than $1.0 \mu\text{m}$ are not prone to sinking [67].

In the following, our focus is thus on particulate matter larger than $1.0 \mu\text{m}$ (Fig. 4.1). Organic matter is produced in the sun-lit layer of the ocean by the primary production through photosynthesis of autotrophic microbes (mainly bacteria and phytoplankton). During their lifetime growth they exude colloidal and small particles to finally form larger particles when they die. Dead phytoplankton are within the range of $1 \mu\text{m}$ (picoplankton, e.g. cyanobacteria) and a few hundred of micrometers (microphytoplankton, e.g. diatoms).

Thereafter zooplankton consumes alive phytoplankton and inert particles and produce fecal pellets and dead bodies. Most fecal materials have enough size to sink rapidly by their own [37]. Typical sizes of such particles are $10 \mu\text{m}$ for a pellet of copepod of $200 \mu\text{m}$ length [79], krill fecal pellets are between $160 \mu\text{m} - 460 \mu\text{m}$ [109] and euphausiid fecal pellets span $300 \mu\text{m} - 3 \text{mm}$ [85], providing the total range of $10 \mu\text{m}$ to 3mm . Concerning the zooplankton dead bodies, they are divided in micro-, meso- and macro-, with sizes in the range $20 \mu\text{m} - 1 \text{cm}$. A detailed summary is given in Table 4.1.

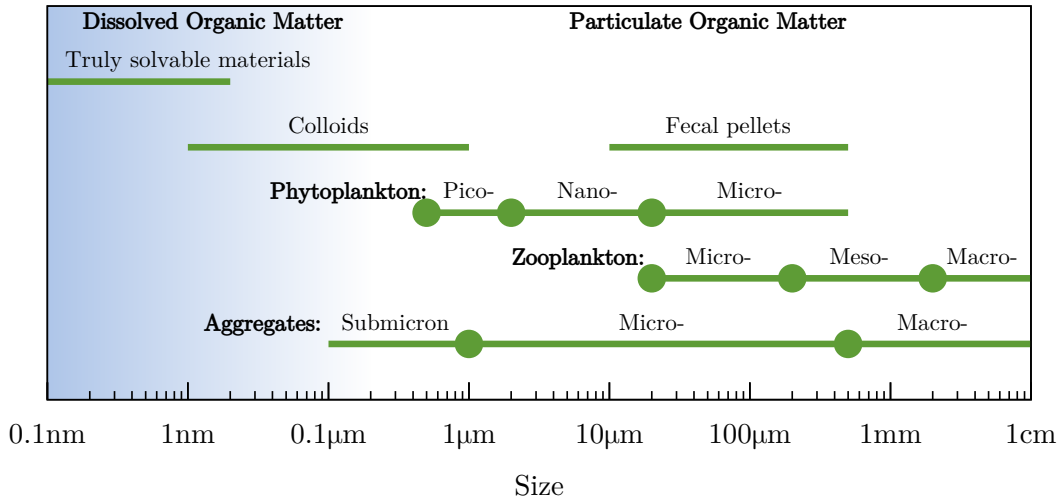


Figure 4.1: Size and classification of marine particles (adapted from [165]).

Finally, there are the so-called organic aggregates which occur in the size range of $1\mu\text{m}$ to 10cm . They are typically formed *in-situ* by physical aggregation or biological coagulation and are usually composed of numerous planktonic individuals and fecal pellets stucked together within a colloidal matrix. They are often distinguished in three size classes [165]: macroscopic aggregates or macro-aggregates $> 5\text{mm}$ usually called marine snow; microscopic, from 1 to $500\mu\text{m}$, also known as micro-aggregates; and submicron particles $< 1\mu\text{m}$ (which do not sink).

4.2.2 Density

The density of marine particles depends on their composition which can be divided into a mineral and a organic fraction [100]. The mineral or inorganic matter consists of biogenic minerals: Particulate Inorganic Carbon (PIC), e.g. calcium carbonate produced by coccoliths with density 2700 kg/m^3 and Biogenic Silica (BSi), produced by diatoms, significantly less denser than PIC, 1950 kg/m^3 [8]. The density of Particulate Organic Matter (POC) ranges widely depending on its origin. For instance, the density of cytoplasm spans from 1030 to 1100 kg/m^3 , while the one of fecal pellets ranges between 1174 kg/m^3 and 1230 kg/m^3 [85]. Despite this variability, it is possible to assign a range to the density of organic matter, from 1050 to 1500 kg/m^3 .

Considering all these estimates together, the density of marine particle ranges approximately between 1050 to 2700 kg/m^3 [99]. This should be compared a standard value for sea water density in the interior ocean which spans roughly 1020-1030 kg/m^3 . Thus

Individual Particles (mostly organic)	Aggregates (compounds of organic and inorganic particles)
<p data-bbox="239 595 584 629">Fecal pellets (cylindrical):</p> <ul style="list-style-type: none"> <li data-bbox="300 658 715 797">• Krill fecal pellets: Length between 400 μm and 9 mm, diameter 120 μm [109]. ESD (160 μm – 460 μm) <li data-bbox="300 826 715 927">• 10 μm, consistent with pellet volume of a 200 μm copepod [79] <p data-bbox="239 956 564 990">Dead zooplankton [170]:</p> <ul style="list-style-type: none"> <li data-bbox="300 1019 576 1084">• Macrozooplankton: size > 2000 μm <li data-bbox="300 1113 612 1178">• Mesozooplankton: 200 < size < 2000 μm <li data-bbox="300 1207 580 1272">• Microzooplankton: 20 < size < 200 μm <p data-bbox="239 1301 596 1335">Dead phytoplankton [170]:</p> <ul style="list-style-type: none"> <li data-bbox="300 1364 600 1429">• Microphytoplankton: (size > 200 μm) <li data-bbox="300 1458 592 1523">• Nanophytoplankton: (20 < size < 200 μm) <li data-bbox="300 1552 580 1617">• Picophytoplankton: (2 < size < 20 μm) 	<p data-bbox="740 595 954 629">Aggregates[165]:</p> <ul style="list-style-type: none"> <li data-bbox="785 658 1187 723">• Macroscopic (Marine Snow): size > 500 μm. <li data-bbox="785 752 1107 817">• Microscopic: 1μm < size < 500 μm. <li data-bbox="785 846 983 911">• Submicron: size < 1 μm.

Table 4.1: Simplified categorization of marine biogenic particles, and their associated sizes.

most of the particle types described previously will sink. Assuming constant size and density for each particle along its downward course, we deduce that most of the particles types described previously will sink. This holds without considering biogeochemical and (dis)aggregation processes that may occur in nature, thus lowering the particle density and resulting in clustering and trapping of particles at particular isopycnals [168]. Note that we do not consider here living organisms which show vertical movements by active swimming or by controlling their buoyancy [116, 6].

4.3 Equations of motion for small spherical rigid particles

4.3.1 The Maxey-Riley-Gatignol equation

To describe the sedimentation of biogenic particles, we need to study the motion of single particles driven by fluid flow. A milestone to analyze the dynamics of a small spherical rigid particle of radius a subject to gravity acceleration \mathbf{g} in an unsteady fluid flow $\mathbf{u}(\mathbf{r}, t)$ is given by the Maxey-Riley-Gatignol [107, 54, 111, 26] equation (MRG in the following). The full MRG is very complicated to manage. A further simplification is usually performed based on the single assumption of very small particles (what this exactly means will be discussed later on). Equation (1.51) is the starting point for most inertial particle studies [111, 9, 26].

We now discuss the validity of the MRG equation Eq. (1.50) or rather its simplified form Eq. (1.51) for the range of sizes and densities of marine organisms. We do so in the context of open-ocean flows, which are typically most energetic at the mesoscale (scales of about 100 km), and where there is a strong stratification, with vertical velocities three or four orders of magnitude smaller than horizontal ones. The motion becomes more three-dimensional, and then the concepts of three-dimensional turbulence more relevant, below scales l of some hundred of meters, with typical velocities decreasing as $l^{1/3}$ for decreasing scale and velocity gradients increasing as $l^{-2/3}$ until the Kolmogorov scale $l = \eta$ below which flow becomes smooth. Because of its direct exposure to wind, turbulence intensity is typically larger at the ocean surface, with values of turbulent energy dissipation in the range $1 \cdot 10^{-6} m^2/s^3 < \epsilon < 3 \cdot 10^{-5} m^2/s^3$ [81], than at depth. The first condition for the validity of the MRG equation that was originally discussed by [107] is that the particles have to be much smaller than the typical length scale of variation of the flow. This means that for multiscale (turbulent) flows the radius of the particle a has to be much smaller than the Kolmogorov scale η , which according to the previous values of ϵ , is typically $0.3mm < \eta < 2mm$ in the ocean surface [121, 81]. Note that we only have to consider worst-case situations for assessing the validity of the different approximations. Another condition to be fulfilled is that the shear Reynolds number must be small $Re_{\nabla} = a^2 U / \nu L \ll 1$, where U and L are typical velocity and length scales. For a turbulent ocean with multiple scales and velocities, the most

restrictive condition arises when they take the values of the Kolmogorov velocity v_η and length η , respectively, since then the velocity gradients are maxima. In this case the condition becomes $Re_\nabla = a^2/\eta^2 \ll 1$, which again is satisfied for small particles. We note that [59] found that the relative importance of the history term in Eq. (1.50) with respect to the drag force is of the order of a parameter which in our notation is $(Re_\nabla)^{1/2}$. This justifies neglecting the history term for small particles, although its importance increases for increasing size [36, 59].

Another condition to be satisfied for the validity of the MRG equation is that the so-called Reynolds particle number, $Re_p = \frac{a|v-u|}{\nu}$ should fulfill $Re_p \ll 1$. Considering that gravity force dominates over other forces one has $|v-u| \simeq |v_s| \equiv v_s$, where v_s is, as introduced before, the settling velocity of particles in a quiescent fluid due to Stokes drag. The Reynolds particle number is then $Re_p = \frac{av_s}{\nu}$. Note that the settling velocity depends only on the densities of particles via the parameter β . Assuming a mean density of sea water in the upper ocean as $\rho_f = 1025 \text{ kg/m}^3$ the parameter β has values within the range [0.5, 0.99] for the typical values of the density of marine particles previously discussed. Fig. 4.2 shows v_s for different sizes and the regions where $Re_p > 1$ (and other parameter regions where MRG is not a good approximation) as a function of particle radius and for the limiting values of β . It reveals that Eq. (1.50) can not describe ocean particles larger than $300 \mu\text{m}$ of any density, and for a limited range of densities when the particle radius exceeds approximately $100 \mu\text{m}$. In fact, the range of application of MRG to marine particles is plotted in the blue area, which at the same time gives an estimate of the typical sinking velocities for a given particle size.

Summarizing, both the MRG and its approximation Eq. (1.51) are valid for marine particles with size within the range $1 \mu\text{m}$ and $200 \mu\text{m}$. That is, it is valid for all particulate organic matter in Fig. 4.1 except the largest of the micro-aggregates and meso- and macro-bodies of zooplankton. The sinking velocities range from 1 mm/day - 1 km/day .

4.3.2 The MRG equation in a rotating frame and further simplifications

We are interested in applying Eq. (1.51) in oceanic flows, where the particle \mathbf{v} and flow \mathbf{u} velocities are expressed in a frame rotating with the Earth angular velocity $\boldsymbol{\Omega}$ [45, 16, 173, 135, 155]. Both time derivatives $\frac{d}{dt}$ and $\frac{D}{Dt}$ have to be corrected following the rule

$$\frac{d}{dt} \rightarrow \frac{d}{dt} + 2\boldsymbol{\Omega} \times \mathbf{v} + \boldsymbol{\Omega} \times (\boldsymbol{\Omega} \times \mathbf{r}), \quad (4.1)$$

$$\frac{D}{Dt} \rightarrow \frac{D}{Dt} + 2\boldsymbol{\Omega} \times \mathbf{u} + \boldsymbol{\Omega} \times (\boldsymbol{\Omega} \times \mathbf{r}). \quad (4.2)$$

Where $\Omega = |\boldsymbol{\Omega}|$ and \mathbf{r} is the particle position vector whose origin is in the rotation axis. So that Eq.(1.51) is now

$$\frac{d\mathbf{v}}{dt} = \beta \frac{D\mathbf{u}}{Dt} - \frac{\mathbf{v} - \mathbf{u}}{\tau_p} - 2\boldsymbol{\Omega} \times (\mathbf{v} - \beta\mathbf{u}) + \mathbf{v}'_s/\tau_p. \quad (4.3)$$

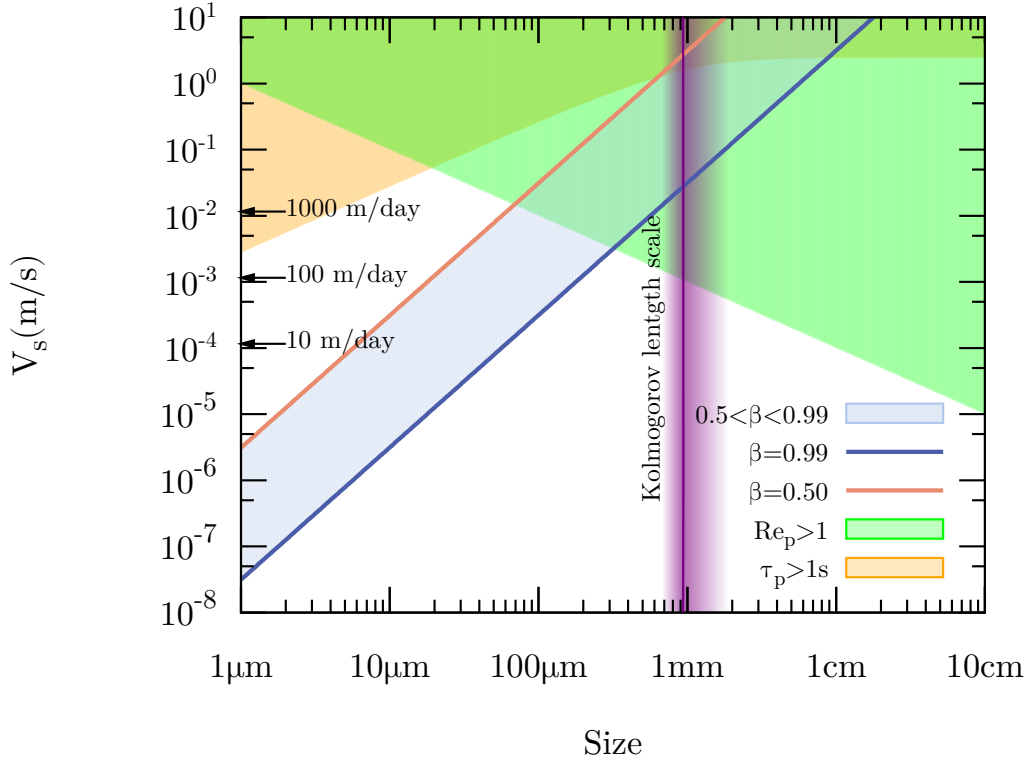


Figure 4.2: Sinking velocity versus particle radius for different β , which is determined by densities. The blue zone determines the values of the settling velocities at a given radius, as determined by the typical marine particle densities. The green area is determined by the condition $Re_p > 1$ for which the MRG equation is not valid. Use of the MRG equation is also unjustified for particles larger than the Kolmogorov length scale also plotted in the figure. We also show the region $\tau_p > \tau_\eta \approx 1s$ where the additional approximation leading to Eq. (4.4) becomes invalid.

Two apparent forces arise in the equation, the Coriolis force $2\mathbf{\Omega} \times (\mathbf{v} - \beta\mathbf{u})$ and the centrifugal force, which is included in a modified sinking velocity $\mathbf{v}'_s = (1 - \beta)(\mathbf{g} - \mathbf{\Omega} \times (\mathbf{\Omega} \times \mathbf{r}))\tau_p$. The effect of the centrifugal force is very small (of order 10^{-3} compared to gravity) and can be absorbed in a redefinition of \mathbf{g} . Thus, in the following we take $\mathbf{v}'_s = \mathbf{v}_s$ with the properly chosen \mathbf{g} .

The ratio between the particle response time and the Kolmogorov time scale is the Stokes number $St = \tau_p/\tau_\eta$, which measures the importance of particle's inertia because of its size and density. According to the range of ϵ in the ocean mentioned before, we get $0.1 s < \tau_\eta < 5 s$, and for our range of particle sizes $10^{-6} s < \tau_p < 10^{-2} s$ so we can assume that $St \ll 1$ (see Fig. 4.2). This motivates us to make a second (standard) approximation [9, 64] of the MRG equation expanding in powers of τ_p (note that it

would be more natural to make the expansion in powers of the non-dimensional St but we prefer to do it in τ_p to control on the time scales of the problem). Assuming first the solution to Eq. (1.51):

$$\mathbf{v} = \mathbf{u} + \mathbf{u}_1\tau_p + \mathbf{u}_2\tau_p^2 + \dots,$$

and using $\frac{d\mathbf{v}}{dt} = \frac{D\mathbf{u}}{Dt} + O(\tau_p)$, we get that the particle velocity at first order in τ_p is

$$\mathbf{v} = \mathbf{u} + \mathbf{v}_s + \tau_p(\beta - 1) \left(\frac{D\mathbf{u}}{Dt} + 2\boldsymbol{\Omega} \times \mathbf{u} \right). \quad (4.4)$$

It is worth recalling that $\tau_p(1 - \beta) = v_s/g$, so that all dependencies on particle size and density appear in Eq. (4.4) through the combination of parameters defining v_s . Different combinations of size and density, taken within the ranges reported in Sect. 4.2, follow the same dynamics if they have the same undisturbed settling velocity v_s .

A further discussion of Eq. (4.4) follows. At this order only three physical processes correct the particle velocity with respect to the fluid velocity: the Stokes friction determining the settling velocity v_s , the inertial term given by $\tau_p(\beta - 1)\frac{D\mathbf{u}}{Dt}$ whose major effect is to introduce a centrifugal force pulling particles away from vortex cores [106, 111], and the influence of the Coriolis force $2\tau_p(\beta - 1)\boldsymbol{\Omega} \times \mathbf{u}$. Concerning sinking dynamics, the $\mathbf{v} = \mathbf{u} + \mathbf{v}_s$ is the most relevant approximation, and many other studies consider it, mainly in oceanographic contexts [e.g. 163]. Note that we can use the right-hand-side of Eq. (4.4) with $\mathbf{u} = \mathbf{u}(\mathbf{r}, t)$ to define the particle velocity \mathbf{v} as a velocity field in three-dimensional space $\mathbf{v} = \mathbf{v}(\mathbf{r}, t)$. If one uses the lowest-order approximation $\mathbf{v} \approx \mathbf{u}$ we have $\nabla \cdot \mathbf{v} = \nabla \cdot \mathbf{u} = 0$ when the fluid velocity field \mathbf{u} is incompressible (which is the case for ocean flows). This means that when considering this term alone, one cannot obtain a compressible particle velocity whereas this was the main reason invoked to explain the clustering of finite-size particles [169, 10]. For this reason, numerous studies [173, 111, 11, 12, 26, 59, 60, 13] consider the role of the additional terms. With them $\nabla \cdot \mathbf{v} = \tau_p(\beta - 1)\nabla \cdot \left(\frac{D\mathbf{u}}{Dt} + 2\boldsymbol{\Omega} \times \mathbf{u} \right) \neq 0$, and inertia-induced clustering may occur. In the following sections we address two main questions: a) how relevant for the sinking dynamics are the Coriolis and centrifugal terms?; and b) are they essential ingredients for the clustering of biogenic particles? We will study the relevance of the different terms in Eq. (4.4) in a realistic oceanic setting.

4.4 Numerical simulations

The velocity flow \mathbf{u} of the Benguela region was produced by a regional simulation of a hydrostatic free-surface primitive equations model called ROMS (Regional Ocean Modelling System). The configuration used here extends from 12°S to 35°S and from 4°E to 19°E (blue rectangle in Fig. 3) and was forced with climatological atmospheric data [61]. The simulation area extends from 12°S to 35°S and from 4°E to 19°E (blue rectangle in Fig. 4.3). The velocity field data set consists of 2 years of daily averages of zonal (u), meridional (v) and vertical velocity (w) components, stored in a 3D grid with a horizontal resolution of 1/12° and 32 vertical terrain-following levels using a stretched

vertical coordinate where the layer thickness increases from surface/bottom to the ocean interior.

In order to integrate particle trajectories from the velocity in Eq. (4.4) we interpolate linearly $\mathbf{u}(\mathbf{r}, t)$ from the closest space-time grid points to the actual particle locations. Given the huge disparity between the model resolution and the small particle-sizes considered, it is pertinent to parameterize in some way the unresolved scales. This can be done by different approaches, from stochastic Lagrangian modeling [18], to deterministic kinematic fields [126]. The first approach is adopted by adding a simple white noise to the particle velocity [172], with different intensity in the vertical and horizontal directions. Thus, we consider this noisy version of the simplified MRG:

$$\frac{d\mathbf{r}(t)}{dt} = \mathbf{v}(t) \quad (4.5)$$

$$\mathbf{v} = \mathbf{u} + \mathbf{v}_s + \tau_p(\beta - 1) \left(\frac{D\mathbf{u}}{Dt} + 2\boldsymbol{\Omega} \times \mathbf{u} \right) + \mathbf{W}. \quad (4.6)$$

$\mathbf{W}(t) \equiv \sqrt{2D_h}\mathbf{W}_h(t) + \sqrt{2D_v}W_z(t)$, with $(\mathbf{W}_h, W_z) = (W_x(t), W_y(t), W_z(t))$ a three-dimensional vector Gaussian white noise with zero mean and correlations $\langle W_i(t)W_j(t') \rangle = \delta_{ij}\delta(t - t')$, $i, j = x, y, z$. We consider an horizontal eddy diffusivity, D_h , depending on resolution length scale l according to Okubo formula [121, 69]: $D_h(l) = 2.055 \times 10^{-4}l^{1.15}$ (m^2/s). Thus, if taking $l \sim 8 \text{ km} = 8000 \text{ m}$ (corresponding to $1/12^\circ$) we obtain a value that we approximate by $10m^2/s$. In the vertical direction we use $D_v = 10^{-5}m^2/s$ [149].

In order to obtain quantitative assessment of the relative effects of the different physical terms in Eq. (4.6), we will compare trajectories obtained from the following expressions which only consider some of the terms of the full expression Eq. (4.6):

$$\mathbf{v}^{(0)} = \mathbf{u} + \mathbf{v}_s + \mathbf{W}, \quad (4.7)$$

$$\mathbf{v}^{(co)} = \mathbf{u} + \mathbf{v}_s + \tau_p(\beta - 1)2\boldsymbol{\Omega} \times \mathbf{u} + \mathbf{W}, \quad (4.8)$$

$$\mathbf{v}^{(in)} = \mathbf{u} + \mathbf{v}_s + \tau_p(\beta - 1) \frac{D\mathbf{u}}{Dt} + \mathbf{W}. \quad (4.9)$$

Besides the random noise term, the first expression (4.7) only considers the settling velocity, equation (4.8) resolves the settling velocity plus the Coriolis effect, and equation (4.9) considers the settling plus the inertial term.

For the numerical experiments we will consider a set of six values of v_s ranging from $5m/day$ to $200m/day$, with different integration times to have in all the cases a sinking to about $1000 - 1100 \text{ m}$ depth. The stochastic equation (4.5) with expressions (4.6)-(4.9) is written in spherical coordinates and numerically integrated using a second-order Heun's method with time step of 4 hours [175]. We use $R = 6371 \text{ km}$ for the Earth radius, $g = 9.81m/s^2$, and the angular velocity $\boldsymbol{\Omega}$ is a vector pointing in the direction of Earth axis and modulus $|\boldsymbol{\Omega}| = 7.2722 \times 10^{-5} \text{ s}^{-1}$. We take v_s and τ_p constant in each experiment because, although water density may increase with depth, this variation is at most of $10kg/m^3$ in the range of depths we are considering here and then the impact on v_s is below 0.1%. We use as initial starting date 17 September 2008. The numerical experiments consist in launching $N = 6000$ particles from initial conditions randomly

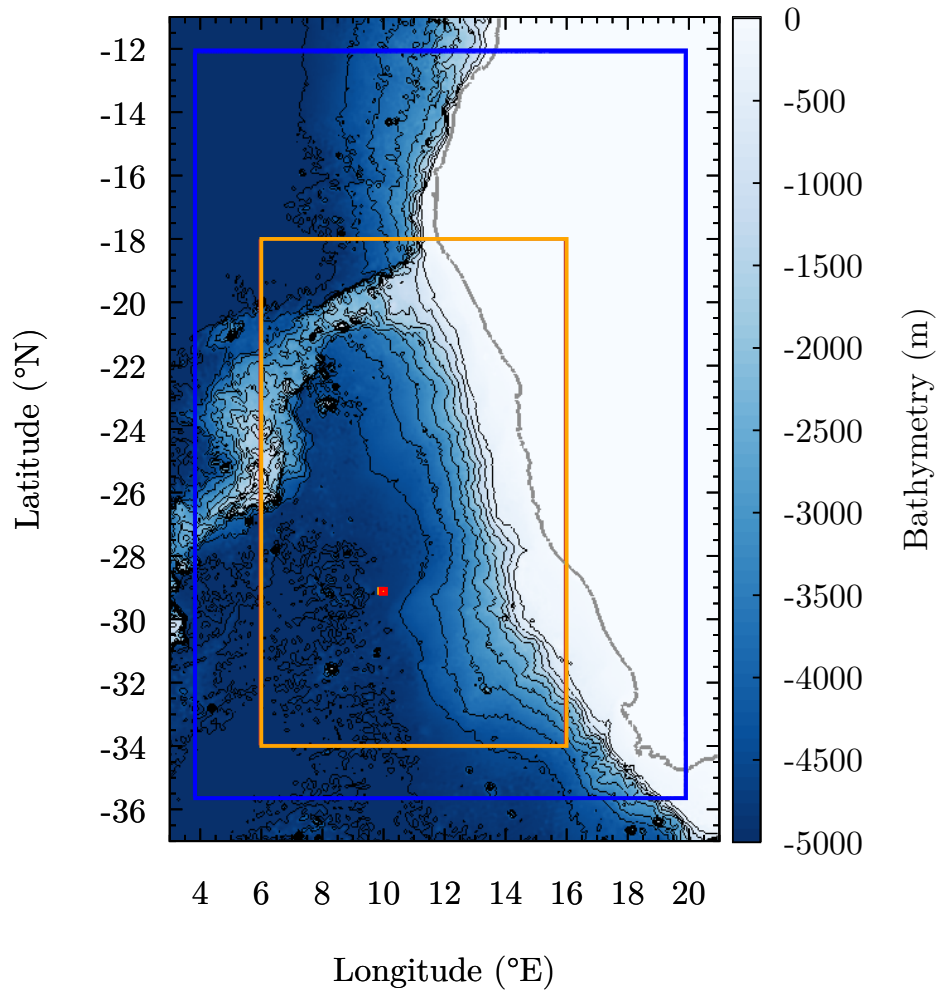


Figure 4.3: Map of region of study. Color corresponds to bathymetry. Blue rectangle is region used for simulations of the ROMS model. Orange rectangle is the region for the clustering numerical experiment of Sect. 4.5 and red rectangle is the release site of the sinking numerical experiments of Sect. 4.4. Gray represent the coastline.

chosen in a square of size $1/6^\circ$ centered at $10.0^\circ E$ $29.12^\circ S$ and $-100.0m$ depth (red rectangle in Fig. 4.3), and in letting them evolve for a given time t_f (stated in Table 4.2) following Eq. (4.5) with expressions (4.6)-(4.9). We use in each case identical initial conditions and the same sequence of random numbers for the noise terms. In this way we guarantee that any difference in particle trajectories arise from the inclusion or not of the inertial and Coriolis terms. We obtain the time-dependent positions of all the particles for each approximation to the dynamics: $\mathbf{r}_i(t)$, $\mathbf{r}_i^{(0)}(t)$, $\mathbf{r}_i^{(co)}(t)$, and $\mathbf{r}_i^{(in)}(t)$, $i = 1, \dots, N$, following respectively Eqs. (4.6)-(4.9) and the corresponding final positions at $t = t_f$.

Table 4.2 gives the mean and the standard deviation of the depths attained by the set of particles in each numerical experiment as obtained from Eqs. (4.5) and (4.6). We find that the use of the different approximations (4.7)-(4.9) gives virtually the same results. The only differences larger than 1 *cm* in mean or standard deviation are the ones for the smallest unperturbed settling velocity considered, $v_s = 5$ *m/day*, and are also reported in Table 4.2. The measured differences are negligible as compared with the traveled distance or even with the model grid size. Indeed small changes in the ROMS model configuration or in the velocity interpolation procedure would have an impact larger than this. The mean displacements in the horizontal obtained with the different approximations (not shown) differ also in less 0.1%. We thus conclude that the simplest approximation Eq. (4.7) which only considers passive transport and an added constant sinking velocity already provides a good description of the sinking process for the type of marine particles and the range of space and time scales considered here. Note that the depth attained by the particles is always slightly shallower than $z = -1100$ *m*, which is the depth that would be reached in a still fluid. It is still debated under which conditions fluid flows enhances or reduces the settling velocity [106, 180, 151, 12].

v_s (<i>m/day</i>)	integration time t_f (<i>days</i>)	Mean final depth (<i>m</i>)	std final depth (<i>m</i>)
200	5	-1091.78	3.88
100	10	-1065.33	6.57
50	20	-1033.97	6.22
20	50	-1051.85	22.67
10	100	-1043.49	51.22
5	200	-1054.97	62.03
		-1054.76 (co)	62.14 (co)
		-1054.76 (in)	62.16 (in)
		-1054.72 (0)	62.14 (0)

Table 4.2: Mean and standard deviation of the set of depths attained, according to Eqs. (4.5) and (4.6), by the set of particles released from the red rectangle in Fig. 4.3 at $z = -100$ *m* for the different values of v_s and integration times used. The results labeled (co), (in), and (0) are obtained from the different approximations in Eqs. (4.7)-(4.9), which differ more than 1 *cm* from the ones obtained from Eq. (4.6) only in the $v_s = 5$ *m/day* case. .

We perform now a more stringent test going beyond the analyses of mean displacements by considering differences between individual particle trajectories. To assess the impact of the Coriolis and of the inertial effects we compare the positions $\mathbf{r}_i^{(co)}(t)$, and $\mathbf{r}_i^{(in)}(t)$ with the simpler dynamics Eq. (4.7) which gives $\mathbf{r}_i^{(0)}(t)$ for each time t . To do so we compute the root mean square difference in position per particle and time, which

we separate in vertical and horizontal components:

$$r_h^{(k)}(t) = \sqrt{\frac{1}{N} \sum_{i=1}^N \left(\mathbf{x}_i^{(0)}(t) - \mathbf{x}_i^{(k)}(t) \right)^2} \quad (4.10)$$

$$r_v^{(k)}(t) = \sqrt{\frac{1}{N} \sum_{i=1}^N \left(z_i^{(0)}(t) - z_i^{(k)}(t) \right)^2} \quad (4.11)$$

with $\mathbf{x}_i = (x_i, y_i)$, the horizontal position vectors, and the superindex (k) takes the values (*co*) or (*in*).

Fig. 4.4 shows the influence of the Coriolis term in the horizontal component for each sinking velocity as a function of time. We observe an exponential growth in a wide range of times, which reveals the chaotic behavior of each of the compared trajectories. The value of the exponent 0.08days^{-1} is in agreement with the order of magnitude of the Lyapunov exponent calculated using the same ROMS velocity model and region [15]. Similar exponential growth with the same growth rate were observed for the inertial terms and the vertical components (not shown), although the absolute magnitude of these mean root square differences was much smaller.

The horizontal and vertical differences $r_{h,v}^{(co)}$ at the final integration time t_f (i.e. the time at which the particles reach an approximate depth of 1000 *m* for each value of v_s) are displayed in Fig. 4.5, both as a function of v_s and of t_f . Similarly, the values of $r_{h,v}^{(in)}$ are presented in Fig. 4.6. The behavior can be understood as resulting from two factors: on the one hand smaller v_s requires larger t_f to reach the final depth, and larger integration time t_f allows for accumulation of larger differences between trajectories. On the other hand the Coriolis and inertial terms in Eqs. (4.8)-(4.9) are proportional to $\tau_p(\beta - 1) = v_s/g$ so that their magnitude decreases for smaller v_s . The combination of these two competing effects shapes the curves in Figs. 4.5 and 4.6, which for the vertical-difference case turn-out to be non-monotonic in v_s or t_f .

In all cases, the differences (both in vertical and horizontal) between the simple dynamics (4.7) and the corrected ones in Eqs. (4.8) and (4.9) are negligible when compared with typical particle displacements, or even with model grid sizes. For example, we imposed in our simulations a vertical displacement close to 1000 *m*, whereas the mean root square difference with respect to simple sinking is below 1 *m* for the Coriolis case (Fig. 4.5) and below 1 *cm* for the inertial case (Fig. 4.6). In the horizontal direction, displacements during those times are of the order of hundreds of *km*, whereas the corrections introduced by the Coriolis and inertial terms are in the worst cases of the order of a few kilometers or of tens of meters, respectively. In particular, the most important impact (horizontal differences of tens of kilometer) is attributed to the Coriolis term for particles sinking at 5 *m/day* (Fig. 4.5). It is worth noting that although the small value of Rossby number $\simeq 0.01$ for mesoscale processes might indicate a strong influence of the Coriolis force in Eq. (4.6), its influence on particle dynamics becomes negligible because it is multiplied by τ_p or equivalently, the Stokes number, which is significantly small for biogenic particles. Nevertheless Rossby number coincides with the ratio of inertial term to Coriolis term in Eq. (4.6) and its value $\simeq 0.01$ explains the difference of

two orders of magnitude among the corrections arising from the inertial force and from Coriolis. The trajectories of the full dynamics ruled by Eq. (4.6) are nearly identical to the ones under the approximation which keeps only the sinking term and Coriolis, so that the corresponding comparison to $\mathbf{r}_i^{(0)}$ gives a figure essentially identical to Fig. 4.5 (not shown).

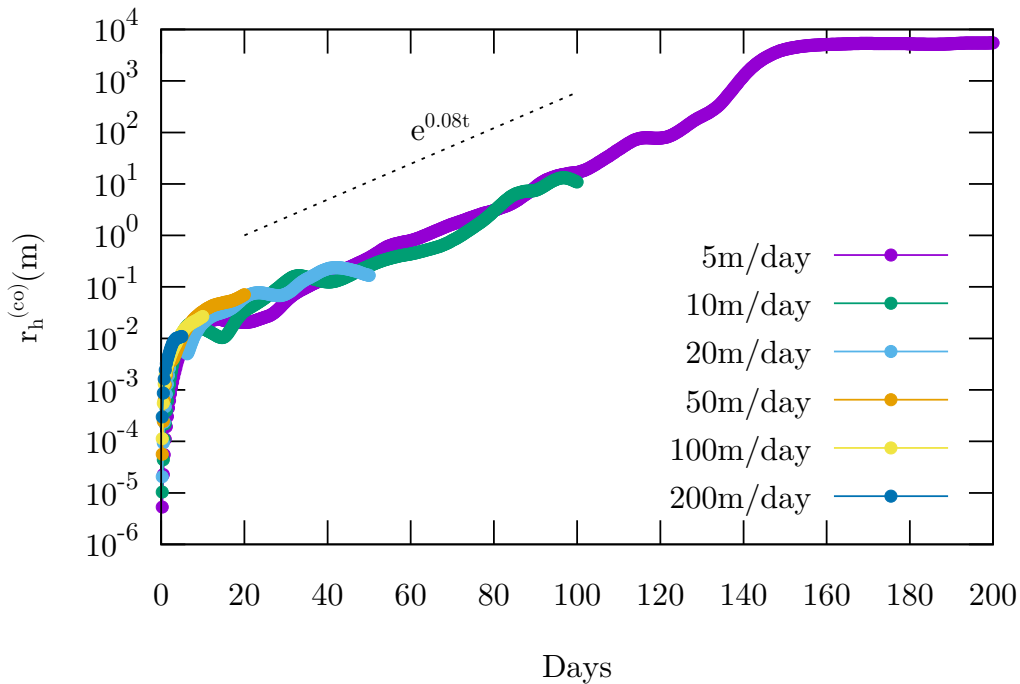


Figure 4.4: Root mean square difference per particle, as a function of time, between horizontal particle positions computed with Eq. (4.7) and with Eq. (4.8), i.e. with and without the Coriolis term. The different colors correspond to distinct values of the unperturbed sinking velocity. The dashed line is an exponential with slope 0.08 day^{-1} .

In summary, for the range of sizes and densities of the marine particles considered here, the sinking dynamics is essentially given by the velocity $\mathbf{v} = \mathbf{u} + \mathbf{v}_s$, which has been the one used in some oceanographic studies [163, 164, 150]. Note however that a new question arises: what is then the reason for the observed clustering of falling particles [96, 20, 113]? The argument of the non-inertial dynamics of the particles does not serve since $\nabla \cdot \mathbf{v} = \nabla \cdot \mathbf{u} = 0$. A possible response is explored in the next section.

4.5 Geometric clustering of particles

Compressibility of the particle-velocity field, i.e. $\nabla \cdot \mathbf{v} \neq 0$, which can arise from inertial effects even when the corresponding fluid-velocity field is incompressible $\nabla \cdot \mathbf{u} = 0$, has

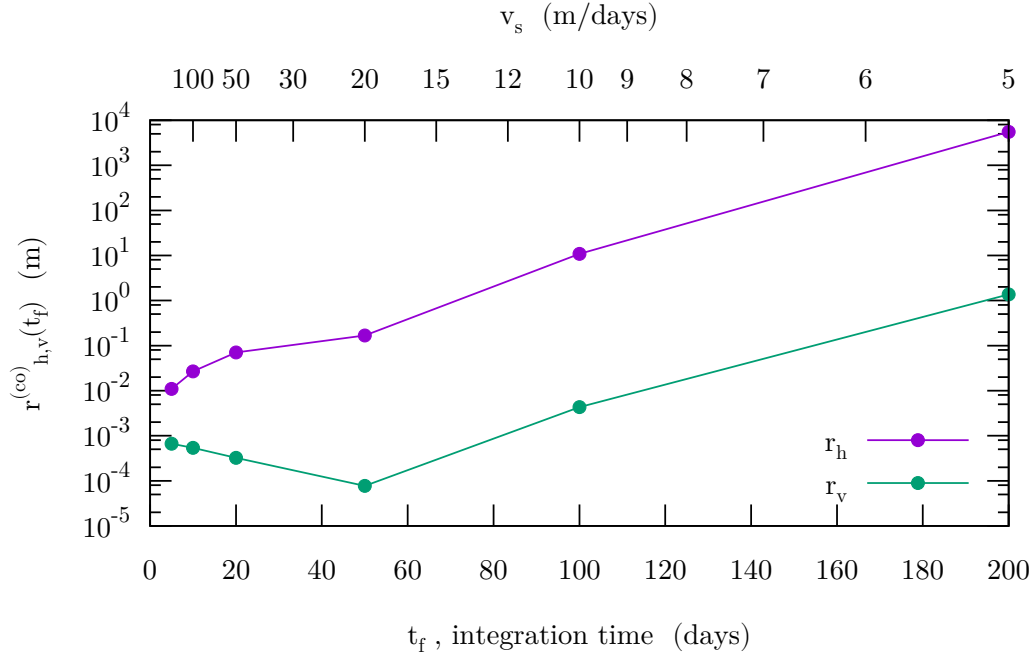


Figure 4.5: Root mean square difference per particle between final positions (at times t_f stated in Table 4.2) computed with and without the Coriolis term (Eqs. (4.8) and (4.7), respectively). Data are presented as a function of the unperturbed sinking velocity v_s used (upper horizontal scale) and of the final integration time t_f (lower horizontal scale). Upper violet line, the horizontal difference $r_h^{(co)}(t_f)$; lower green line, the vertical difference $r_v^{(co)}(t_f)$.

been identified as one of the mechanisms leading to preferential clustering of particles in flows [169, 9]. This is so because $\rho(t)$, the particle density at time t at the location $\mathbf{r} = \mathbf{r}(\mathbf{r}_0, t)$ of a particle that started at \mathbf{r}_0 at time zero, satisfies $\rho(t) = \rho(0)\delta^{-1}$, where δ is a dilation factor equal to the determinant of the Jacobian $|\frac{\partial \mathbf{r}}{\partial \mathbf{r}_0}|$, which satisfies

$$\frac{1}{\delta} \frac{D\delta}{Dt} = \nabla \cdot \mathbf{v} \quad (4.12)$$

or, using $\delta(0) = 1$:

$$\delta(t_f) = e^{\int_0^{t_f} dt \nabla \cdot \mathbf{v}}. \quad (4.13)$$

Thus, particles will accumulate (i.e. higher $\rho(t_f)$) in final deep locations receiving particles whose trajectories have predominantly travelled through regions with $\nabla \cdot \mathbf{v} < 0$. We have seen however that, to a good approximation $\nabla \cdot \mathbf{v} \approx \nabla \cdot \mathbf{u} = 0$ since inertial effects can be neglected for the type of marine particles we consider here, and then the three-dimensional particle-velocity field is incompressible.

We now reproduce numerically a typical situation in which clustering of marine particles is observed. We release particles uniformly in an horizontal layer close to the

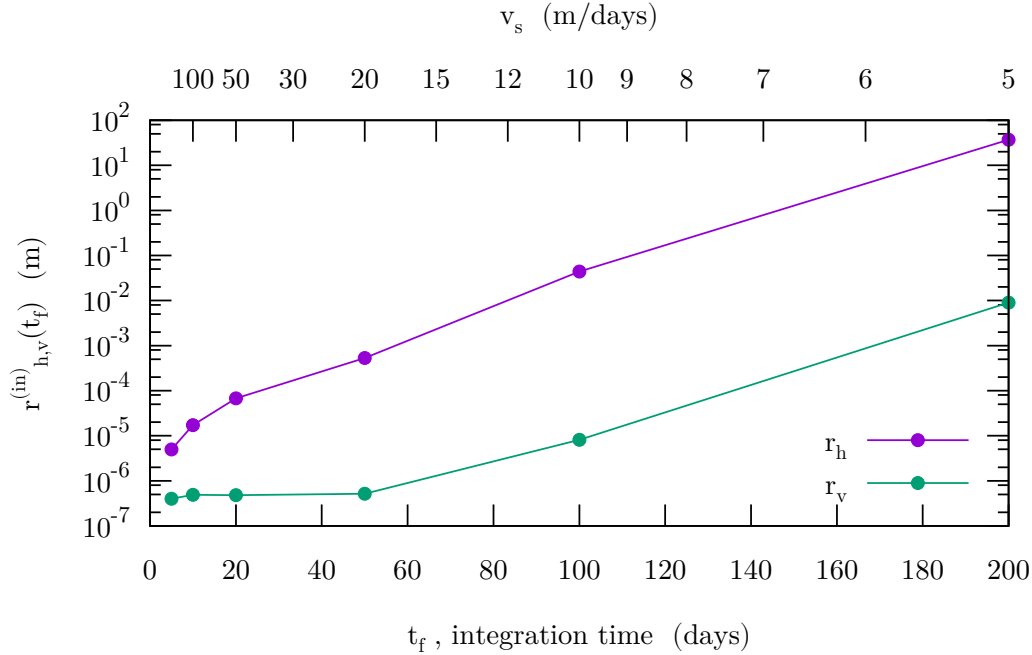


Figure 4.6: Root mean square difference per particle between final positions (at times t_f stated in Table 4.2) computed with and without the inertial term (Eqs. (4.9) and (4.7), respectively). Data are presented as a function of the unperturbed sinking velocity v_s used (upper horizontal scale) and of the final integration time t_f (lower horizontal scale). Upper violet line, the horizontal difference $r_h^{(in)}(t_f)$; lower green line, the vertical difference $r_v^{(in)}(t_f)$.

surface, we let them sink within the oceanic flow and we finally observe the distribution of the locations where they touch another horizontal deeper layer. The domain chosen is the rectangle $12^\circ S$ to $35^\circ S$ and $4^\circ E$ to $19^\circ E$ (orange rectangle in Fig. 4.3). We divide the domain horizontally in squares of side $1/25^\circ$, then initialize 1000 particles at random positions in each of them in August 20, 2008 at depth $z = -100$ m (i.e. the bottom of the euphotic layer, starting point of our biogenic particles), and then integrate each trajectory until it reaches -1000 m depth. We use expression (4.7) for the velocity, with $v_s = 50$ m/day. In order to avoid any small fluctuating compressibility arising from the noise term we put $\mathbf{W} = \mathbf{0}$ but we have checked that the result in the presence of noise is virtually indistinguishable (not shown). At the bottom layer ($z = -1000$ m) we count how many particles arrive to each of the $1/25^\circ$ boxes and display the result in Fig. 4.7(a). Despite $\nabla \cdot \mathbf{v} = 0$ we see clear preferential clustering of particles in some regions related to eddies and filaments. We note that our horizontal boxes have a latitude-dependent area so that distributing particles at random in them produces a latitude-dependent initial density which could lead to some final inhomogeneities. We have checked however that for the range of displacements of the particles, this effect

is everywhere smaller than 5% and thus can not be responsible for the large clustering observed in Fig. 4.7(a). Nevertheless, this effect will be taken into account later.

We explain the observed particle clustering by considering the field displayed in Fig. 4.7(a) as a projection in two dimensions of a density field (the cloud of sinking particles) which evolves in three-dimensions. Even if the three-dimensional divergence is zero, and then an homogeneous three-dimensional density will remain homogeneous, a two-dimensional cut or projection can be strongly inhomogeneous. This mechanism has been proposed to explain clustering and inhomogeneities in the ocean surface [77, 80], but we show here that it is also relevant for the crossing of a horizontal layer by a set of falling particles.

A simple way to confirm that this clustering arises from the two-dimensionality of the measurement is to estimate the changes in the horizontal density of evolving particle layers as if they were produced just by the horizontal part of the velocity field. This is only correct if an initially horizontal particle layer remains always horizontal during the sinking process, which is not true. But, given the huge differences in the values of the horizontal and vertical velocities in the ocean, we expect this approximation to capture the essential physics and provide a qualitative explanation of the observed cluster. We expect the approximation to become better for increasing v_s , because of the shorter sinking time during which vertical deformations could develop. Thus we compute the two-dimensional version of the dilation field, $\delta_h(\mathbf{x}, t_f)$, at each horizontal location \mathbf{x} in the deep layer at $z = -1000m$:

$$\delta_h(\mathbf{x}, t_f) = e^{\int_0^{t_f} dt \nabla_h \cdot \mathbf{v}} \quad (4.14)$$

with the horizontal divergence

$$\nabla_h \cdot \mathbf{v} \equiv \frac{\partial v_x}{\partial x} + \frac{\partial v_y}{\partial y} = \frac{\partial u}{\partial x} + \frac{\partial v}{\partial y} = -\frac{\partial w}{\partial z}, \quad (4.15)$$

where in the second equality we have used Eq. (4.7) from which $\nabla_h \cdot \mathbf{v} = \nabla_h \cdot \mathbf{u}$ and the third one is a consequence of $\nabla \cdot \mathbf{u} = 0$. In order to get the values of δ_h on a uniform grid on the $-1000m$ depth layer at the arrival date t_f of the particles in the previous simulation, we integrate backwards in time trajectories from grid points separated $1/50^\circ$ at $z = -1000m$ until they reach $-100m$. The starting date (t_f) of the backwards integration was September 7, 2008, i.e. 18 days after the release date used in the previous clustering experiment. This value correspond to the average duration time of trajectories in that experiment. Then δ_h was computed integrating in time the values of $\nabla_h \cdot \mathbf{v}$ along every trajectory using Eq. (4.14).

Figure 4.7(b) displays the quantity $\delta(\mathbf{x}, t_f)^{-1} \cos(\theta_f) / \cos(\theta_0)$, which gives the ratio between densities in the upper and lower layer, corrected with the angular factors controlling the area of the horizontal boxes so that this can be compared with the ratio between particle numbers displayed in Fig. 4.7(a). θ_f is the latitude of point \mathbf{x} , and θ_0 is the latitude of the corresponding trajectory in the upper $z = -100 m$ layer. As stated before, the latitudinal corrections by the cosine terms are always smaller than a 5%. Although there is no perfect quantitative agreement, there is clear correspondence

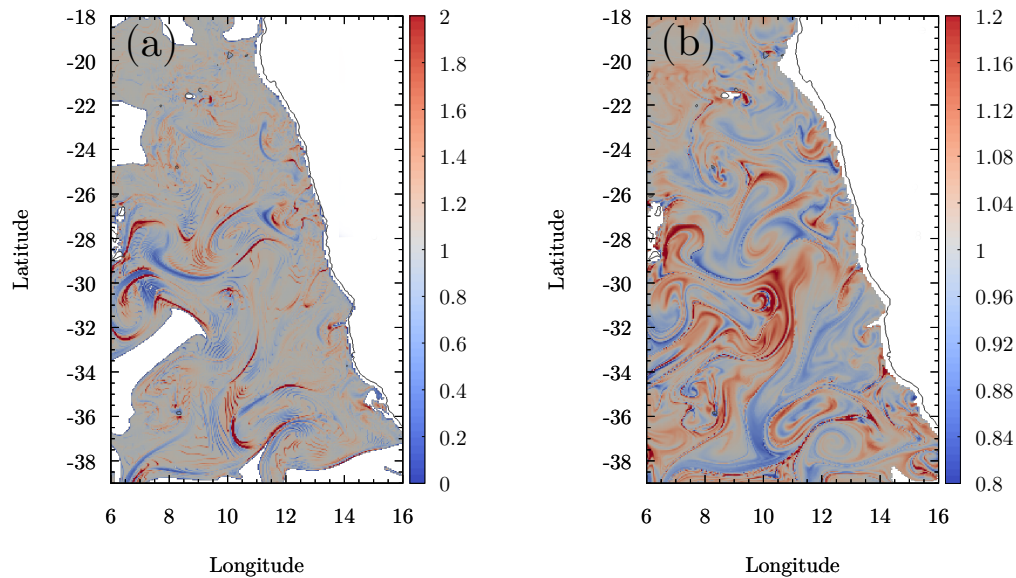


Figure 4.7: Results of the clustering numerical experiments of Sect. 4.5. (a) N_f/N_0 , the number of particles N_f arriving to an horizontal box of size $1/25^\circ$ in the horizontal layer at $z = -1000$ m, normalized by the number of particles $N_0 = 1000$ released from the upper $z = -100$ m layer. (b) The corrected dilation factor $\delta(\mathbf{x}, t_f)^{-1} \cos(\theta_f)/\cos(\theta_0)$ mapped on the final $z = -1000$ m layer. It gives the ratio between horizontal densities at the final and initial locations, corrected with the latitudinal dependence of the horizontal boxes used in panel (a), to give an estimation of the local particle number ratio between lower and upper layer. Black thin line represents the coastline; white oceanic areas indicate in (a) regions which do not receive any falling particles; in (b) regions from which the backward integration ends up outside the domain.

between the main clustered structures in panels (a) and (b) of Fig. 4.7, confirming that they originate from the horizontal dynamics in an incompressible three-dimensional velocity field. We have checked in specific cases that locations with larger differences between Figs. 4.7(a) and (b) correspond to places with large dispersion in the arrival times to the bottom layer, indicating deviations from the horizontality assumption.

In the next chapter we develop a deeper description of the inhomogeneities described here.

CHAPTER 5

Inhomogeneities of sinking particles in ocean flows

This chapter focusses on the role of the transport processes, in particular on how a homogeneous layer of particles stretches and folds due to the oceanic currents while it is sinking, to finally form inhomogeneous and clustering when they are trapped. We do not consider geological time scales, so that our results explicitly attempt to explain some of the measurements obtained in sediment traps. We perform numerical experiments in the Benguela region (in the southwest coasts of Africa) by letting particles to sink from the marine surface and then collect them at a given depth. We analyse the accumulated density of particles at any given position, and analytically obtain a general formula for this as a function of the velocity of the particles (that depends on the size and density of the particles through their settling velocity). We check the validity of our formula for the mentioned region, improving here the analysis of Section 4.5. We compare the different distributions that represents organisms of different densities and sizes conform.¹

5.1 Introduction

The sinking of biogenic particles in the oceans provides the essential food source for the deep-sea organisms, but also it is a fundamental ingredient of the biological carbon pump [152]. During the settling of marine particles, biochemical reactions occur that modify sinking particle fluxes [117]. Remineralization and grazing decrease the flux of marine snow with depth [37]. Furthermore, oceanic currents induce lateral transport of sinking particles due to their relatively small vertical velocity compared to horizontal ocean velocities. This implies that sinking particles travel almost horizontally, and their source area may be rather distant from the location where they settle in the deep ocean [163, 181, 156, 95]. When settled on the seafloor or collected at a given depth by sediment traps [20], a relevant feature is the presence of inhomogeneities in the spatial distribution of the particles, i.e. collecting sites that are relatively close can receive a significantly different amount of particles [95]. This is mainly attributed to inhomogeneities in the primary production of particles in the upper ocean, but the combined effect of biochem-

¹This chapter is based on: Pedro Monroy, Gabor Drótos, Emilio Hernández-García and Cristóbal López. “*Spatial inhomogeneities in the sedimentation of biogenic particles in ocean flows: analysis in the Benguela region*”. Under review, *Journal of Geophysical Research - Oceans* (2019)

ical reactions and ocean currents acting while the particles are sinking can alter their spatial distribution [39]. Concerning some of these processes relevant on non-geological time scales, much has been learnt by suspending sediment traps in the ocean to collect the particles: in particular, about the amount of delivered particles from the surface, the organisms that are involved, their size and thus their settling speed, and the aggregates that form while sinking (marine snow). But many questions still remain open referring to the above-mentioned inhomogeneous distribution of the particles: How do the spatial patterns of sedimentation depend on the characteristics of the particles? How do oceanic currents shape these patterns? And how do the biogeochemical processes shape them during sinking? Proper answers to these questions will for sure be relevant for a proper quantification of the biological carbon pump, and help identify those areas of the oceans that can be labeled as sinks or sources of carbon. Therefore, their further study is needed in order to better estimate ocean carbon sequestration from primary production in the upper ocean, inferred for example from satellite data.

This chapter focuses on the role of the transport processes on some of the above questions, in particular on how a layer of particles homogeneously released at the surface would give rise to strong spatial inhomogeneities when arriving to some depth, because of the stretching and folding action of the oceanic currents during the sinking process. We do not consider geological time scales, so that our results explicitly attempt to provide a basis for explaining some features of measurements carried out with sediment traps [95]. We perform numerical experiments in the Benguela region (at the southwestern coasts of Africa) by letting particles sink from a layer near the marine surface and then observing where do they arrive at a given depth. We analyze the accumulated density of particles at different locations.

In [40], analytical expressions were found that give the mass or the density of particles accumulated at a collecting horizontal surface at a given depth, coming from a falling sheet of particles released at a shallower depth, in terms of the trajectories of the particles and properties of the velocity field along them. In this chapter we use that framework, adapted so that it could be applied more conveniently to realistic oceanic settings. Specifically we apply it to the sinking of biogenic particles in the Benguela region, using an ocean velocity field computed in that region. Since particle vertical motion involves a settling term which depends on particle physical properties (density and size), the final distribution will depend on these physical characteristics. Thus, we can compare the different distributions that particles of different densities and sizes will form by studying different values of the settling velocity.

A main finding in [40] was that the dependence of the particle density on horizontal position at the collecting surface can be understood in terms of two basic processes: the stretching due to the flow of the sinking sheet of particles, and the projection of this sheet on the surface where particles will accumulate. In our numerical experiments in the Benguela region, we check the validity of our analytic expressions, analyze how they may explain the inhomogeneities of sedimentation in this particular geographical zone, and test the relative importance of the two mechanisms producing inhomogeneity, stretching and projection. Also, we will examine the role of the resolution at which the distribution on the density at the accumulating surface is sampled, and provide new

analytical formulae that help the discussion of the results in the oceanic framework.

The chapter is organized as follows: In section 5.2 we present the data and the methods of our work, which includes the analytical formulae describing the accumulated density of particles at a given depth, the decomposition of the dynamics into the stretching and projection, and also the statistical methodology to compare these results with the ones obtained from direct sampling of particle positions. In section 5.3 we present our numerical results for the Benguela region.

5.2 Data and methods

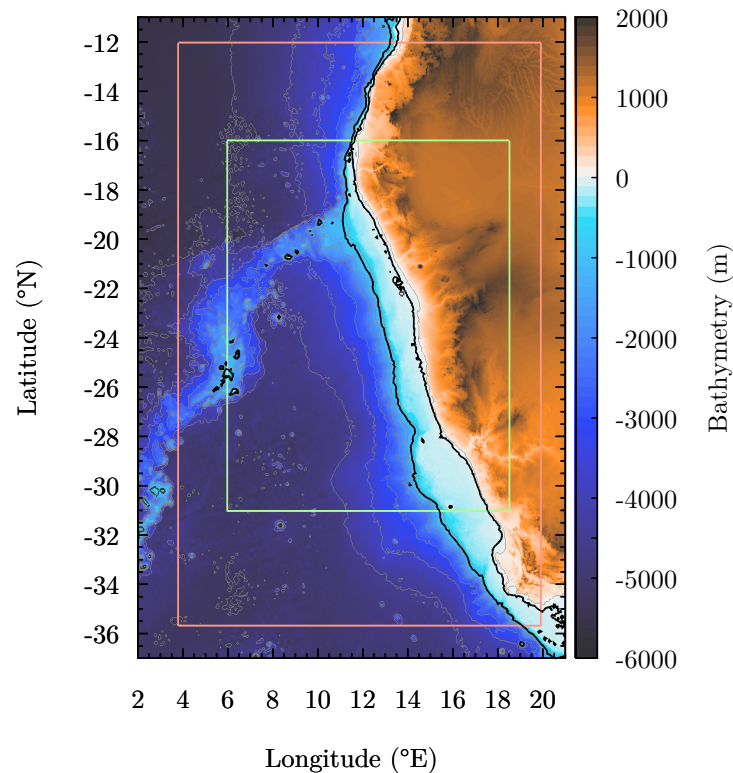


Figure 5.1: Map of the region of study. Color corresponds to bathymetry. The red rectangle is the region used for simulations of the ROMS model. The green rectangle is the region for the numerical experiments. Black lines represent 100 and 1000m depth, the particle releasing depth and the accumulation depth, respectively.

A three-dimensional model is used to simulate the vertical transport of biogenic particles produced in the euphotic zone and sedimenting to the deep sea. It is composed by the output velocity of a hydrodynamical model combined with a Lagrangian particle

tracking model. We next specify the area of study (the Benguela region), the velocity data, and the Lagrangian equations for the sinking dynamics.

5.2.1 Area of study and velocity data

The velocity data set used is the output of a regional ocean model (Regional Ocean Modelling System, ROMS) simulation of the Benguela region (Figure 5.1). Corresponds to the same model used in previous chapter.

5.2.2 Lagrangian tracking of sinking particles

We are interested in describing the sinking dynamics of particulate organic matter biologically generated close to the ocean surface, in the euphotic layer. Sizes of these particles or aggregates range between $1\mu\text{m}$ and more than 1 cm , and densities are between 1050 and 2700 kg/m^3 [114]. For sizes smaller than $200\ \mu\text{m}$, i.e. for the majority of particle types except the largest aggregates and zooplankton bodies (meso- and macro-zooplankton), particle inertia can be safely neglected [114] and the velocity of the particle, \mathbf{v} , is well approximated by the sum of the velocity field of the fluid \mathbf{u} and a vertical settling velocity \mathbf{v}_s [40]. This last quantity is the terminal velocity for sinking in a quiescent fluid, pointing vertically downwards. It depends on the physical properties of the particles as

$$\mathbf{v}_s = (1 - \beta)\mathbf{g}\frac{a^2}{3\beta\nu}, \quad \text{with} \quad \beta = \frac{3\rho_f}{2\rho_p + \rho_f}, \quad (5.1)$$

where a is the particle radius (particles are assumed to be spherical), \mathbf{g} is the gravitational acceleration, ρ_f is the fluid density, ρ_p is the particle density, and ν is the kinematic viscosity of the fluid. Values of the modulus of the settling velocity $v_s = |\mathbf{v}_s|$ for the biogenic particles under study are in the range 1 mm/day - 1 km/day , but we will concentrate here in the most common values which are 35 - 235 m/day (Table 5.1). The vertical fluid velocities in the mesoscale flow field we are considering are of the order of 10m/day at most; in particular, we will always have a strictly negative vertical velocity for the particles, $v_z < 0$, i.e. the particles will always be sinking. Constant size and contrast of density between particle and water are assumed for each particle along its downward path. This implies, as mentioned in the introduction, the neglect of biogeochemical and (dis)aggregation processes that may occur: our focus is on the role of transport. As a crude way to estimate the effect of small-scale motions that are unresolved by the hydrodynamical model, we add a white noise term to the particle velocity, with different intensities in the vertical and the horizontal directions. In summary, the model we use for the velocity of the sinking particles is the following stochastic equation [114]:

$$\begin{aligned}\frac{d\mathbf{R}}{dt} &= \mathbf{v}(\mathbf{R}, t), \\ \mathbf{v} &= \mathbf{u} + \mathbf{v}_s + \mathbf{W}.\end{aligned}\tag{5.2}$$

$\mathbf{R} = \mathbf{R}(\mathbf{r}_0, t)$ is the position at time t of the particle that was released at position \mathbf{r}_0 at the initial time t_0 . \mathbf{v}_s is the settling velocity discussed above, and $\mathbf{W}(t) \equiv \sqrt{2D_h}\mathbf{W}_h(t) + \sqrt{2D_v}\mathbf{W}_z(t)$, with $(\mathbf{W}_h, W_z) = (W_x(t), W_y(t), W_z(t))$ being a three-dimensional vector Gaussian white noise with zero mean and with correlations $\langle W_i(t)W_j(t') \rangle = \delta_{ij}\delta(t - t')$, $i, j = x, y, z$. We consider a horizontal eddy diffusivity, D_h , that depends on the resolution length scale l according to the Okubo formula [121, 154, 69]: $D_h(l) = 2.055 \times 10^{-4}l^{1.15}(\text{m}^2\text{s}^{-1})$. Thus, when taking $l \simeq 8\text{km} = 8000\text{m}$ (corresponding to $1/12^\circ$), we obtain a value that we approximate by $D_h = 10\text{m}^2\text{s}^{-1}$. In the vertical direction we use a constant value of $D_v = 10^{-5}\text{m}^2\text{s}^{-1}$ [149]. In the derivation of our analytic formulae, however, the particle velocity field is assumed to be a smooth function, which excludes the presence of the irregular noise term. In consequence, the noise term will be chosen to be zero for the evaluation of the geometrical formulae introduced in section 5.2.4. The results obtained from them will be however compared with the histograms obtained from direct sampling of densities from simulated particle trajectories in the presence of the noise term, representing small-scale unresolved fluctuations. Thus, differences between the analytical expressions and the computed histograms would give an idea of the relevance of unresolved flow features on the sedimentation process.

Three-dimensional Lagrangian particle trajectories are obtained by means of numerical integration of equation (5.2) using a second order Heun method with absorbing boundary condition (that is, the integration halts if the trajectory escapes the domain of the simulation (red rectangle in Fig. 5.1) or reaches the seabed outside the domain of the analysis (green rectangle in Fig. 5.1)). For the numerical integration of the trajectories without noise, a fourth-order Runge–Kutta scheme is used. We select 6 hours for the integration time step and linear interpolation in time and space to obtain the flow velocity \mathbf{u} at the location of the particle while it moves between ROMS grid points.

Parameter	Values
Settling velocity v_s	35, 40, 45, and then from 50 to 225m/day using steps of 25m/day
Coarse-graining radius R	from 10km to 100km using steps of 5km
Starting depth	−100m
Final depth	−1000m
Integration time step	6 hours
Starting date	20 August 2008

Table 5.1: Parameters used in the sedimentation simulations.

5.2.3 Numerical experiment and direct sampling of the accumulated density

We consider a situation in which particles are released with uniform density from a horizontal layer close to the surface, at an initial time t_0 , and study how the transport process results in an inhomogeneous distribution of particles when they are collected in a deeper layer. More explicitly, on 20 of August 2008 we initialize a large number of particles at a depth $z_0 = 100\text{m}$ equispaced in the zonal and meridional directions, which is conveniently achieved by using a sinusoidal projection [159]. Then each particle of this horizontal layer is evolved by equation (5.2) until it reaches the depth $z = 1000\text{m}$. The calculation is repeated using a range of settling velocities (see Table 5.1). Note that, according to equation (5.1), increasing the magnitude v_s of the settling velocity means considering heavier particles (or larger ones). The final positions are used to obtain the number $n_R^z(\mathbf{x})$ of particles that are accumulated within a circular sampling area of radius R around a horizontal position \mathbf{x} at this given depth z (we use the notation $\mathbf{r} = (\mathbf{x}, z)$ to distinguish between horizontal, \mathbf{x} , and vertical, z , components of a three-dimensional vector \mathbf{r}). The number density of accumulated particles in this circle is thus $\sigma_z^R(\mathbf{x}) = n_R^z(\mathbf{x})/(\pi R^2)$, where the subindex z indicates that we are measuring the accumulated density at a depth z . The range of the values for the *coarse-graining* radius R is shown in Table 5.1. We will describe our results in terms of the *density on the collecting surface* but this does not need to be an actual physical surface extending over the whole domain of interest, such as the bottom of the sea. For example sediment traps have a rather small collecting surface and are commonly suspended at some intermediate depth. The inhomogeneities we will describe on our virtual *collecting surface* would explain differences in number of captured particles between two traps at the same depth but at two distant horizontal positions [95]. We locate the centers \mathbf{x} of our sampling areas in the collecting surface on a regular grid in latitude and longitude, with a spacing of $1/20^\circ$ in each direction. As found in [114], and consistently with observations [95], the horizontal dependence of the accumulated density $\sigma_z^R(\mathbf{x})$ is highly inhomogeneous. The main purpose of this chapter is to explain the mechanisms leading to these inhomogeneities.

To quantify the inhomogeneity of the accumulated density in the final surface, we compute the density factor [40], i.e., the density relative to its value at the initial depth, σ_0 , i.e.:

$$\mathcal{F}_{\text{hist}}^R(\mathbf{x}) \equiv \frac{\sigma_z^R(\mathbf{x})}{\sigma_0} = \frac{n_R^z(\mathbf{x})}{n_R^0}, \quad (5.3)$$

where n_R^0 is the number of particles initialized in a circle of radius R in the release layer, which is related to the homogeneous release density σ_0 by $n_R^0 = \sigma_0 \pi R^2$. The subindex ‘hist’ in $\mathcal{F}_{\text{hist}}^R$ indicates that this quantity is computed from equation (5.3) that amounts to computing a histogram, and distinguishes it from the geometric quantity $\mathcal{F}_{\text{geo}}^R$ to be defined in the next section. In all our numerical experiments we fix $n_R^0 = 1000$ particles, so that the initial density depends on the choice of the sampling circles and is approximately $\sigma_0 = 1000/(\pi R^2)$. This number of particles proved to be high enough to

ensure the numerical independence of $\mathcal{F}_{\text{hist}}^R$ with respect to changes in the initial surface density.

Sampling circles near the coastline receive significantly less particles than those in the ocean interior due to the absorbing boundary condition. We avoid this effect by discarding circles for which more than 0.01% of their area is occupied by land. Furthermore, boundary effects are also present in sampling areas close to the model domain borders. We also discard sampling areas close to the borders of the hydrodynamical model, and only keep those whose centers are inside the rectangle 2 to 18°E and 31 to 16°S (green rectangle in Figure 5.1).

5.2.4 Geometrical computation of the accumulated density

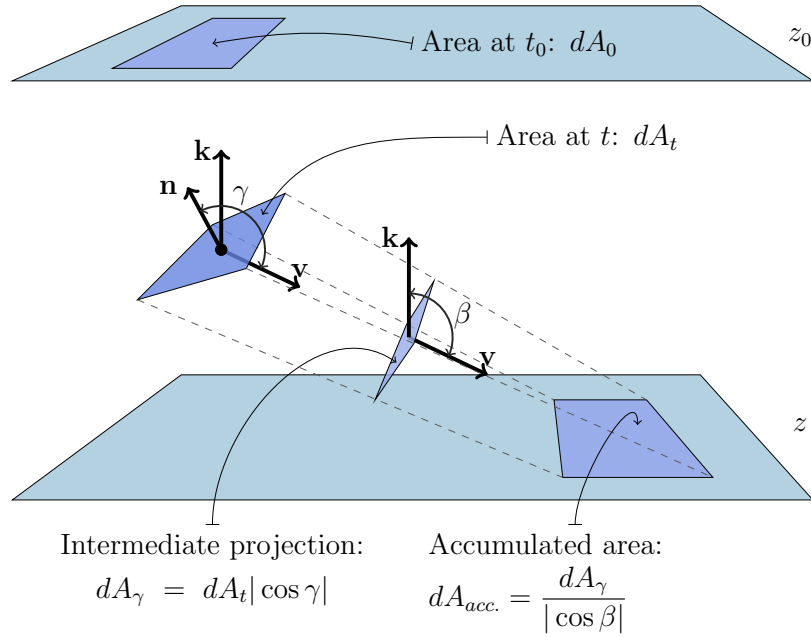


Figure 5.2: Schematic illustration of infinitesimal areas and angles involved in the geometrical computation of the density factor \mathcal{F}_{geo} . A small patch of particles of area dA_0 , located horizontally at depth z_0 at time t_0 , is advected by the velocity field \mathbf{v} . At time t the area of this patch is dA_t . The accumulated area is dA_{acc} , which corresponds to its projection parallel to the flow direction \mathbf{v} onto the horizontal plane. \mathbf{k} is the vertical unit vector, and \mathbf{n} is the unit vector normal to the patch at time t . Assuming mass conservation, the factors \mathcal{F}_{geo} , \mathcal{P} and \mathcal{S} are given by $\mathcal{F}_{\text{geo}} = \frac{dA_0}{dA_{\text{acc}}}$, $\mathcal{S} = \frac{dA_0}{dA_{t_z}}$ and $\mathcal{P} = \frac{dA_{t_z}}{dA_{\text{acc}}} = \left| \frac{\cos \beta}{\cos \gamma} \right|$, where t_z is the time of arrival of the infinitesimal area at the final surface at depth z .

Following [40] we next introduce a geometric approach to compute the density factor (which is equivalent, given σ_0 , to computing the accumulated density profile at the prescribed depth). For the derivations in this section, and for the numerical evaluation of the resulting formulae done in section 5.3, we use equation (5.2) without the noise term, i.e., with $D_h = D_v = 0$, since our mathematical manipulations are only well-defined for smooth velocity fields.

Let us consider (as illustrated in Figure (5.2)) the sinking of the initially horizontal particle layer that was at depth z_0 at time t_0 , and let us focus on the trajectory $\mathbf{R} = \mathbf{R}(\mathbf{r}_0, t)$ of a particle of the layer, which was at $\mathbf{r}_0 = (\mathbf{x}_0, z_0)$ (within the layer) at time t_0 . Let dA_0 be the area of an infinitesimal patch in the horizontal release layer around that particle, containing a number of particles $dn_0 = \sigma_0 dA_0$ (since we use a large number, we neglect the discrete nature of the particle number and approximate it by a continuous variable). Under the action of the flow, during the sinking process the area occupied by these particles will expand or shrink, taking values dA_t , until arriving (non-horizontally in general) to the collecting horizontal surface at depth z (reached at time t_z), where the particles will leave a horizontal footprint of area dA_{acc} . Since the number of particles is conserved, this would produce an accumulated density $\sigma_z = dn_0/dA_{\text{acc}}$. We define the geometric density factor \mathcal{F}_{geo} at the horizontal location \mathbf{x} where the particle that started at \mathbf{r}_0 reaches the layer at depth z as

$$\mathcal{F}_{\text{geo}} \equiv \frac{\sigma_z}{\sigma_0} = \frac{dA_0}{dA_{\text{acc}}} = \frac{dA_0}{dA_{t_z}} \frac{dA_{t_z}}{dA_{\text{acc}}} \equiv \mathcal{S} \mathcal{P}. \quad (5.4)$$

dA_{t_z} is the area of the falling patch at the time t_z when the focus particle reaches the depth z . We have introduced, following [40], the *stretching factor* $\mathcal{S} = dA_0/dA_{t_z}$ which gives the ratio between the initial area surrounding the focus particle and its value when reaching the collecting surface at depth z , and the *projection factor* $\mathcal{P} = dA_{t_z}/dA_{\text{acc}}$. This last quantity is the ratio between this final area of the falling patch (which in general would present a non-horizontal orientation) and its footprint on the horizontal collecting layer. Thus, it gives the geometric projection, parallel to the direction of the flow, of the moving patch (in the neighborhood of the considered particle) onto the horizontal accumulation plane (see Figure 5.2). One interest of the decomposition (equation (5.4)) of the density inhomogeneities into a stretching and a projection factor is that it allows to identify which are the dominant mechanisms producing the observed inhomogeneities in the sedimentation process under different settings and conditions. We will do so in section 5.3 for the case of particles sinking in the Benguela flow, giving special interest to the dependence on the settling velocity component of \mathbf{v} , which encodes the physical properties (density and size, see equation (5.1)) of the sinking particles.

A more detailed derivation of equation (5.4) was given in [40]. Also, several expressions for the explicit calculation of \mathcal{S} and \mathcal{P} were given there, of which we select the following ones (see Appendices J and K of [40]) as more convenient for application to

the oceanic flow:

$$\mathcal{S}(\mathbf{x}) = |\tau_x(t_z) \times \tau_y(t_z)|^{-1}, \quad (5.5)$$

$$\mathcal{P}(\mathbf{x}) = \left| \frac{v_z}{\mathbf{v} \cdot \mathbf{n}} \right| = \left| \frac{\cos \beta}{\cos \gamma} \right|. \quad (5.6)$$

At any time t , $\tau_x(t)$ and $\tau_y(t)$ are two vectors tangent to the falling surface, at the position of the focus particle, calculated as

$$\tau_x(t) = \frac{\partial \mathbf{R}(\mathbf{r}_0, t)}{\partial x_0}, \quad \tau_y(t) = \frac{\partial \mathbf{R}(\mathbf{r}_0, t)}{\partial y_0}, \quad (5.7)$$

where x_0 and y_0 are two orthogonal coordinates on the initial horizontal surface (we use zonal and meridional distances, see Appendices C.1 and C.2). In terms of these tangent vectors the unit vector \mathbf{n} normal to the falling surface at time t reads:

$$\mathbf{n} = \frac{\tau_x \times \tau_y}{|\tau_x \times \tau_y|}. \quad (5.8)$$

In the expression for the projection factor \mathcal{P} , equation (5.6), the vectors and angles involved are defined in Figure 5.2, namely

$$v_z = v \cos \beta, \quad (5.9)$$

$$\mathbf{v} \cdot \mathbf{n} = v \cos \gamma, \quad (5.10)$$

i.e, β is the angle between the vertical direction and the direction of the velocity of the particle at the final time t_z , and γ is the angle between the direction of the particle velocity and the normal to the layer (both at the final time as well). Stretching and projection factors at location \mathbf{x} are evaluated in terms of quantities defined at the final time, t_z , but they depend on the whole history of the falling particle through the initial-position derivatives defining τ_x , τ_y , and then \mathbf{n} .

Equation (5.6) is readily derived from the projection geometry in Figure 5.2. Equation (5.5) is a standard geometrical result for the ratio between the areas of an evolving infinitesimal surface at two times, but we give a short derivation of it in Appendix C.1. We also give an alternative expression and derive some simplifications valid in special cases. In Appendix C.2 we also give additional details on the numerical implementation of its computation.

5.2.5 Statistical analysis: relating direct sampling to the geometrical computation

Since the geometrical computation (section 5.2.4) gives the estimation of the density factor for an infinitesimal sampling area instead of a finite one of radius R as the direct

sampling or histogram method of section 5.2.3 does, we can compare the results from them only in the limit of zero sampling area, $\mathcal{F}_{\text{geo}} = \mathcal{F}_{\text{hist}}^{R \rightarrow 0}$. Estimating this limit is, however, unfeasible due to the finite number of particles used in the numerical implementation. We instead perform a coarse graining of the geometric results using the same circular sampling areas as in the direct sampling method. The coarse-grained value, referring to a circle of radius R around a location \mathbf{x} , of the density factor is computed by taking the harmonic mean of the geometrical density factors at the final locations \mathbf{x}_i of particle trajectories that end inside the sampling area of radius R centered at \mathbf{x} :

$$\mathcal{F}_{\text{geo}}^R(\mathbf{x}) = \frac{n_R(\mathbf{x})}{\sum_{i=1}^{n_R(\mathbf{x})} \frac{1}{\mathcal{F}_{\text{geo}}(\mathbf{x}_i)}}, \quad (5.11)$$

where $n_R(\mathbf{x})$ is the number of such trajectories (i.e., ending inside the circle of radius R). A simple arithmetic mean of the density factors is not appropriate since it will be biased towards high values: there will be more particles falling in regions of high density. See Appendix C.3 for the justification of the choice of the harmonic mean.

Similarly, we compute the coarse-grained version of stretching and projection factors by

$$\mathcal{S}^R(\mathbf{x}) \simeq \frac{n_R(\mathbf{x})}{\sum_{i=1}^{n_R(\mathbf{x})} \frac{1}{\mathcal{S}(\mathbf{x}_i)}} \quad \text{and} \quad \mathcal{P}^R(\mathbf{x}) \simeq \frac{n_R(\mathbf{x})}{\sum_{i=1}^{n_R(\mathbf{x})} \frac{1}{\mathcal{P}(\mathbf{x}_i)}}, \quad (5.12)$$

respectively. The coarse-grained version of the density factor $\mathcal{F}_{\text{geo}}^R$ is certainly not the product of the coarse-grained versions of stretching and projection as given by equations (5.12), but we use these last expressions as a qualitative estimation of the proportion of inhomogeneities arising from each of the two mechanisms.

We will compare the value of $\mathcal{F}_{\text{geo}}^R(\mathbf{x})$ obtained from (5.11) with the value $\mathcal{F}_{\text{hist}}^R(\mathbf{x})$ as obtained from equation (5.3) in the same configuration, for which we locate the sampling areas of radius R at the same locations as for the direct sampling estimation (i.e. in a grid of spacing $1/20^\circ$ in latitude and longitude).

\mathcal{F}_{geo} (as well as \mathcal{S} , \mathcal{P} and σ_z) is a property of each point \mathbf{x} on the collecting surface, in contrast with $\mathcal{F}_{\text{hist}}^R$ which is a property of a neighborhood of radius R around each point. But both characterize the same density inhomogeneities at the collecting surface and they should coincide after properly averaging (or coarse-graining) \mathcal{F}_{geo} in the same neighborhood of radius R , as described in the previous paragraph. Any remaining difference between the two quantities could only arise because the noise term, modeling small scales unresolved by the ROMS simulation, is included in the integration of the particle trajectories when computing $\mathcal{F}_{\text{hist}}^R$, but not when computing $\mathcal{F}_{\text{geo}}^R$. Consequently, our calculation of the geometric factor captures only the inhomogeneities in the accumulated density due to the mesoscales in the ocean flow, which are the resolved scales of the hydrodynamical model. Comparing such results with the histogram $\mathcal{F}_{\text{hist}}^R$ computed from noisy trajectories allows us to check how robust is the calculation of the density factor based on the mesoscale flow with respect to the addition of velocity components not included there, such as the noise term in (5.2).

A quantitative comparison of $\mathcal{F}_{\text{geo}}^R$ with $\mathcal{F}_{\text{hist}}^R$ is done via the Pearson correlation coefficient:

$$\rho(\mathcal{F}_{\text{hist}}^R, \mathcal{F}_{\text{geo}}^R) = \frac{\text{Cov}(\mathcal{F}_{\text{hist}}^R, \mathcal{F}_{\text{geo}}^R)}{\sigma_{\mathcal{F}_{\text{hist}}^R} \sigma_{\mathcal{F}_{\text{geo}}^R}}, \quad (5.13)$$

where $\sigma_{\mathcal{F}_{\text{hist}}^R}$ and $\sigma_{\mathcal{F}_{\text{geo}}^R}$ are the respective standard deviations. The averages needed to compute the covariance and standard deviations are over all the sampling points \mathbf{x} used. We analogously use the Pearson correlation coefficient to characterize the similarity with stretching and projection factors as well.

5.3 Numerical results

Maps of the density factor reveal the inhomogeneities of spatial patterns of sedimented particles produced by oceanic flows. The direct computation (see section 5.2.3) is shown in Figures 5.3a and 5.3c for two different settling velocities. Considerable inhomogeneities in the density of particles are evident: variations of the original density up to factors of 0.5 and 1.5 are common in Figure 5.3a. In general, inhomogeneities are stronger in the southern part of the domain, corresponding to the region of highest mesoscale activity [70]. Also, inhomogeneities are stronger for smaller settling velocity (note the different color scales for the density factor in the corresponding panels of Figure 5.3).

In Figures 5.3b and 5.3d we show the density factor obtained from the corresponding geometrical computation, properly coarse-grained (see section 5.2.5). A visual comparison with Figures 5.3a and 5.3c reveals almost identical patterns. Slightly more differences are noticeable for the larger values of the settling velocity. At high v_s and small R (not shown) we have noticed that the direct sampling estimation is more noisy than the geometrical approach.

The quantitative comparison between the coarse-grained geometrical estimation of the density factor and the direct sampling one, shown in Figure 5.4, gives positive values for $\rho(\mathcal{F}_{\text{hist}}^R, \mathcal{F}_{\text{geo}}^R)$, ranging from 0.5 to 0.9 for all settling velocities and coarse-graining radii tested. For the majority of these parameter values, the correlation coefficient is above 0.7, which indicates a relative insensitivity of the inhomogeneities to flow scales below the mesoscale, which we model here by the presence of the noise term in the calculation of $\mathcal{F}_{\text{hist}}^R$. Figure 5.4 also illustrates that the correlation is lower for the largest and smaller values of R . However, we find a wide range, from $R \approx 25$ to 75km, where high correlations between the two calculations occur for any settling velocity.

We study in Figure 5.5a the dependence of $\rho(\mathcal{F}_{\text{hist}}^R, \mathcal{F}_{\text{geo}}^R)$ on the settling velocity (purple symbols). We find that $\rho(\mathcal{F}_{\text{hist}}^R, \mathcal{F}_{\text{geo}}^R)$ is more affected by v_s than by R . That is, the nature (size and density, equation (5.1)) of the biogenic particles is what determines the difference between the two calculation methods, one restricted to mesoscales and another adding an extra term, which cannot be eliminated by an appropriate choice for the coarse-graining radius. $\rho(\mathcal{F}_{\text{hist}}^R, \mathcal{F}_{\text{geo}}^R)$ achieves its maximum for $v_s = 75\text{m/day}$,

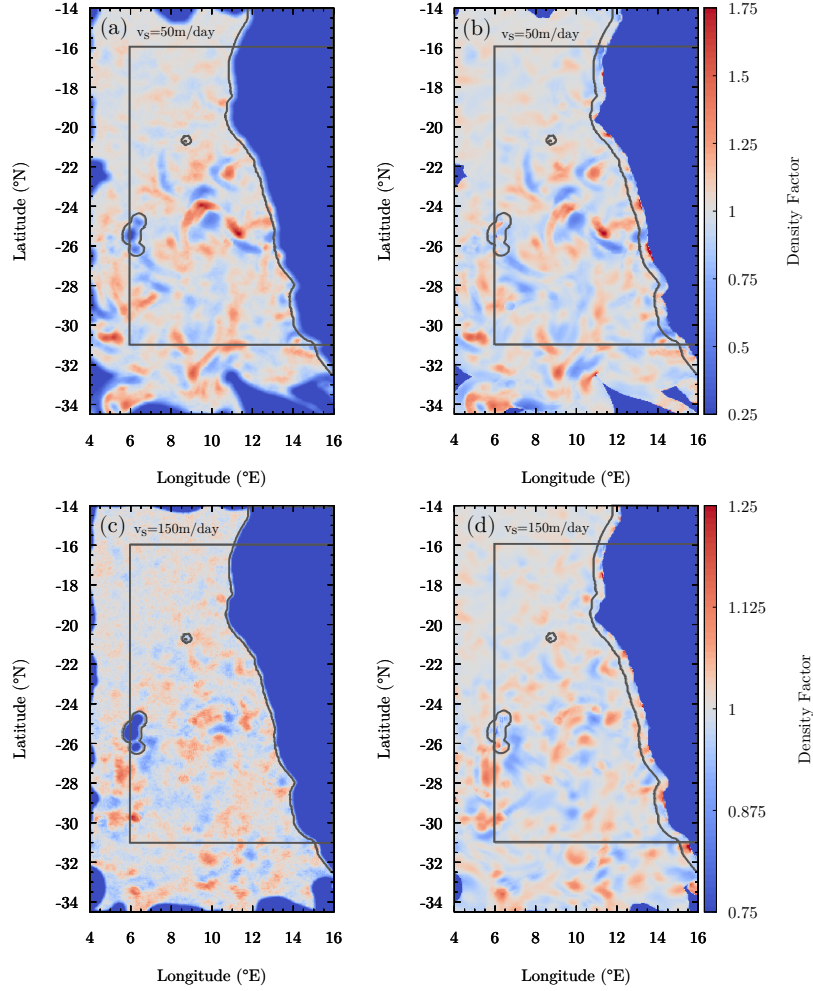


Figure 5.3: Results for the density factor estimation using direct sampling, $\mathcal{F}_{\text{hist}}^R$ from equation (5.3), panels (a) and (c); and using the geometrical approach, $\mathcal{F}_{\text{geo}}^R$ from equation (5.11), panels (b) and (d). Two different settling velocities, 50m/day, panels (a) and (b); and 150m/day, panels (c) and (d) are used (note the different color scale in the two cases). The radius of the circular area for sampling or coarse-graining is 25km in all panels. Further parameters are as in Table 5.1. The gray rectangle will be used in posterior statistical analyses. Thin gray lines bound the circular areas with land ratio less than 0.01%.

roughly independently of R , and decreases fast and slowly for smaller and larger values of v_s , respectively.

We next turn to analyzing the mechanisms from which the inhomogeneities originate. We do so by comparing the coarse-grained density factors $\mathcal{F}_{\text{hist}}^R$ and $\mathcal{F}_{\text{geo}}^R$ with the coarse-grained stretching (\mathcal{S}^R) and projection (\mathcal{P}^R) factors. Already Figure 5.5a makes clear that the stretching factor is correlated increasingly well with the density factor for

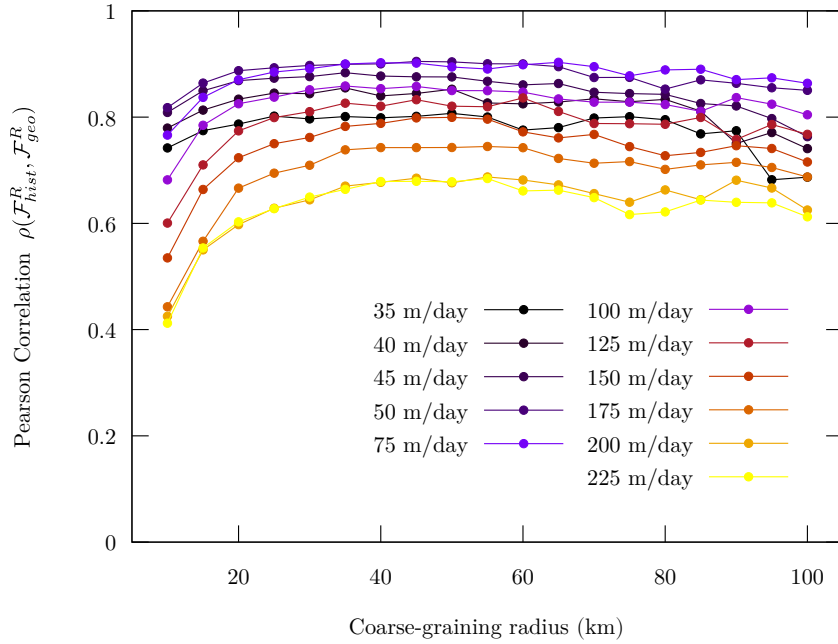


Figure 5.4: Pearson correlation coefficient between $\mathcal{F}_{\text{geo}}^R$ and $\mathcal{F}_{\text{hist}}^R$ as a function of the coarse-graining radius R . Color indicates different values of v_s .

increasing v_s . According to Figure 5.5b, $\rho(\mathcal{F}_{\text{geo}}^R, \mathcal{S}^R)$ approaches almost 1 for high values of v_s , i.e., stretching determines inhomogeneities almost alone for fast-sinking particles. The opposite occurs when lowering v_s , when $\rho(\mathcal{F}_{\text{geo}}^R, \mathcal{P}^R)$ becomes higher (Figure 5.5b), but the trend reverses again for very low values of the settling velocity. The dependence on v_s is quite robust against changing R .

Figure 5.6 characterizes the degree of inhomogeneity in terms of the spatial standard deviation of the coarse-grained density factor, as well as the quantities characterizing the two mechanisms involved, the stretching and projection coarse-grained factors, as a function of $t_f = \frac{|z-z_0|}{v_s}$. This quantity is proportional to the inverse of the settling velocity, and approximately corresponds to the mean arrival time of the particles to the accumulation depth. Using this quantity allows a more intuitive interpretation of the results. In the investigated domain, the degree of inhomogeneity in all factors grows with the time available for sinking, as shown in Figure 5.6. We find that the growth of the standard deviations of \mathcal{S}^R and \mathcal{P}^R with t_f is well described by power laws, t_f^α , with approximate exponents $\alpha \approx 1$ and $5/3$, respectively. Not surprisingly in view of figure 5.5, which indicates a dominance of stretching and of projection at large and at small values of $v_s \propto t_f^{-1}$, respectively, the total factor $\mathcal{F}_{\text{geo}}^R$ reflects the power-law of exponent 1 for short values of t_f and crossovers to the exponent $5/3$, associated to the projection factor, at larger t_f . The standard deviation of $\mathcal{F}_{\text{hist}}^R$ practically coincides with that of $\mathcal{F}_{\text{geo}}^R$ (Figure 5.6d), which means that the dependence on t_f as appearing in the direct sampling method can be traced back to a combination of the mentioned power laws corresponding to the two basic geometric mechanisms, and that only the mesoscales

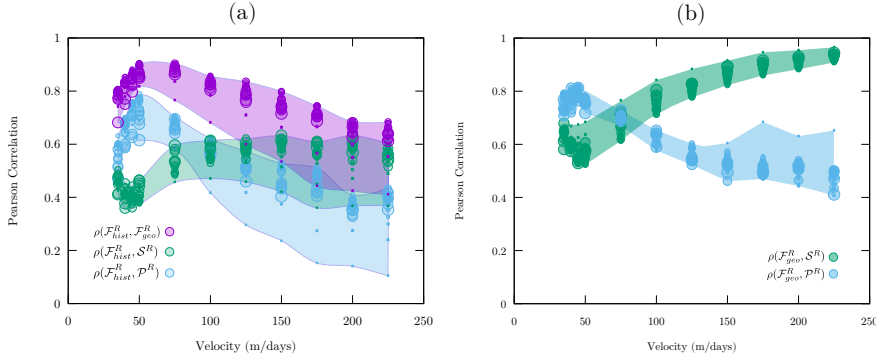


Figure 5.5: a) Pearson correlation between $\mathcal{F}_{\text{geo}}^R$ and $\mathcal{F}_{\text{hist}}^R$ (magenta circles), $\mathcal{F}_{\text{hist}}^R$ and \mathcal{S}^R (green circles) and $\mathcal{F}_{\text{hist}}^R$ and \mathcal{P}^R (blue circles) as a function of the settling velocity v_s . b) Pearson correlation between $\mathcal{F}_{\text{geo}}^R$ and \mathcal{S}^R (green circles) and $\mathcal{F}_{\text{geo}}^R$ and \mathcal{P}^R (blue circles) as a function of the settling velocity. Circle size corresponds to the coarse-graining sampling radius R . Shaded areas indicate the full range of values measured.

included in $\mathcal{F}_{\text{geo}}^R$ turn out to be relevant.

So far, we have investigated results obtained by coarse-graining, which smoothes out any extreme inhomogeneities if they are present. At the same time, the native calculation of the geometrical density factor, \mathcal{F}_{geo} , as defined by equation (5.4), does not involve coarse-graining, so that arbitrarily fine details can be visualized in principle. In Figure 5.7 we show the counterpart of Figure 5.3b (only for the gray rectangle) without coarse-graining. The main difference is the presence of extremely high values. They presumably correspond to projection factors being close to produce *projection caustics*, similar to those found in [40], which will be discussed in section 5.4.2. Both their spatial abundance and the numerical values of the density factor (and then of the density itself) increase as the settling velocity decreases (not shown). We note that the degree of inhomogeneity, including the abundance of extreme values, is larger in the southern part of the area. This difference is presumably related to the stronger turbulence in the southern upwelling region as documented in [70]. Stronger turbulence is associated to larger stretching and also more complex shapes (more tiltiness) for the layer of falling particles [55].

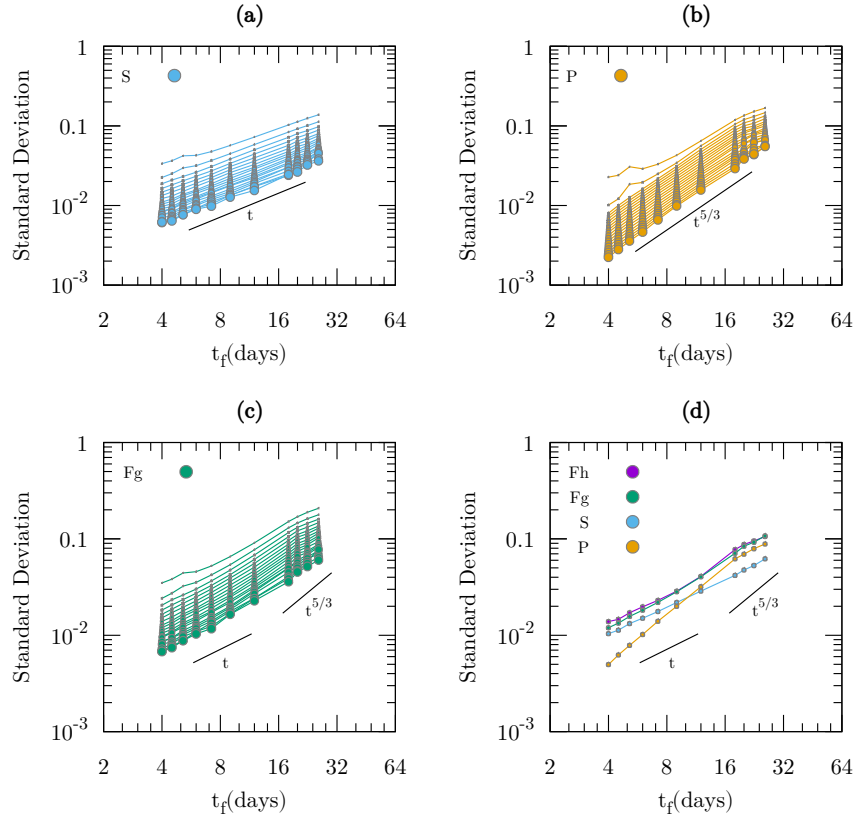


Figure 5.6: Spatial standard deviation of \mathcal{S}^R (a), \mathcal{P}^R (b) and $\mathcal{F}_{\text{geo}}^R$ (c) as a function of $t_f = |z - z_0|/v_s$, which approximately corresponds to the mean arrival time. The size of the circles represents the coarse-graining radius R . Panel (d) displays the spatial standard deviations of $\mathcal{F}_{\text{hist}}^R$, $\mathcal{F}_{\text{geo}}^R$, \mathcal{S}^R and \mathcal{P}^R for one coarse-graining resolution, $R = 50\text{km}$.

5.4 Discussion

5.4.1 The relative importance of stretching and projection in the density factor

We found that the correlations of \mathcal{S}^R and \mathcal{P}^R with $\mathcal{F}_{\text{geo}}^R$ behave differently as a function of v_s (see Figure 5.5): For increasing settling velocities or decreasing t_f , $\rho(\mathcal{F}_{\text{geo}}^R, \mathcal{S}^R)$ becomes higher and approaches 1, whereas $\rho(\mathcal{F}_{\text{geo}}^R, \mathcal{P}^R)$ decreases, implying that the stretching mechanism becomes dominant for fast sinking (and thus short settling time). For very low values of v_s , however, the trends reverse.

Note that the Pearson correlation coefficient carries information about co-occurrence of fluctuations around averages. As for our particular case, if the non-coarse-grained \mathcal{S}

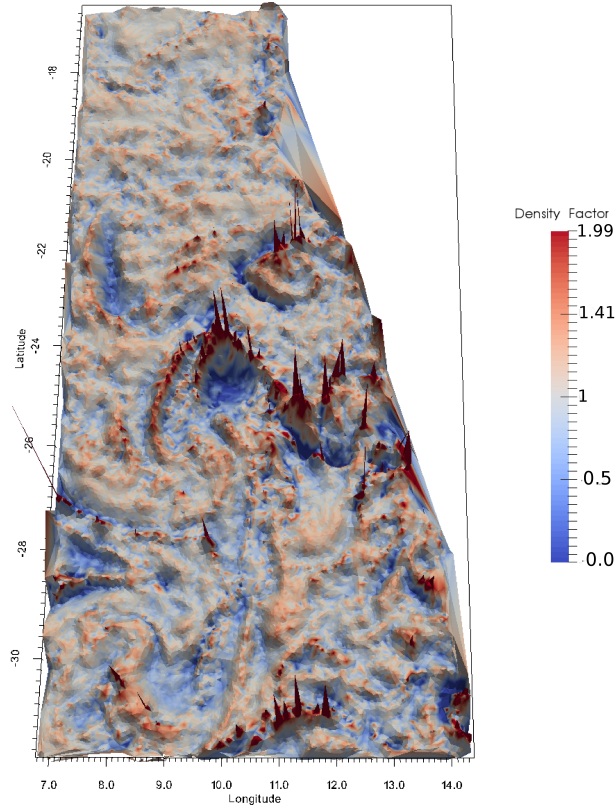


Figure 5.7: Results for the density factor \mathcal{F}_{geo} numerically estimated by the geometrical expression (5.4) for the particle locations within the accumulation level, for a settling velocity of 50m/day. Further parameters are as in Table 5.1. The surface was interpolated applying Delaunay triangulation to the values of density factor at the particles' ending positions. The color and the height of the surface corresponds to the value of the density factor. Note that there are some localized extreme values that are outside the range covered by the color bar.

and \mathcal{P} were uncorrelated, one would find $\rho(\mathcal{F}_{\text{geo}}, \mathcal{S}) = \frac{\sigma_{\mathcal{S}}}{\sigma_{\mathcal{F}_{\text{geo}}}} \langle \mathcal{P} \rangle$, where $\langle \mathcal{P} \rangle$ is the spatial mean of \mathcal{P} , and a similar formula for $\rho(\mathcal{F}_{\text{geo}}, \mathcal{P})$. Although the spatial fluctuations of \mathcal{S} and \mathcal{P} are actually not independent, the spatial means of \mathcal{S} and \mathcal{P} are not investigated, and Figure 5.5 presents coarse-grained quantities, the relationships between the Pearson correlation coefficients and the standard deviations might have some explanatory power in view of Figure 5.6: the linear and the 5/3-power scaling of the standard deviation of \mathcal{S} and \mathcal{P} with the inverse of the settling velocity v_s might make them dominate in these limits.

One should also note that short integration times, corresponding to high settling velocities, make the layer of particles arrive at the accumulation level approximately horizontally, i.e., tiltiness does not have time to develop. Therefore, the normal vector \mathbf{n}

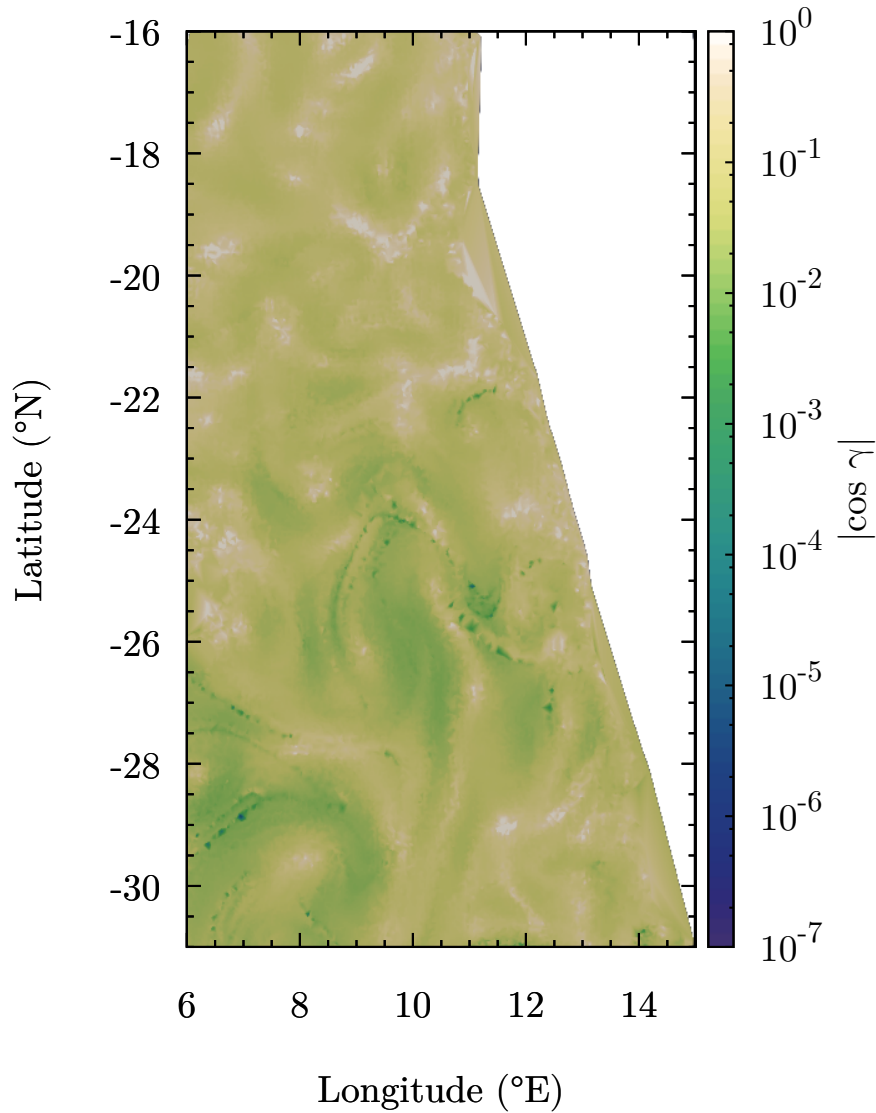


Figure 5.8: Results for the local value of $|\cos \gamma|$ for the same simulation and using the same Delaunay representation as in Figure 5.7. .

of the layer is pointing nearly vertically upwards, $\beta \approx \gamma$ and, from equation (5.6), $\mathcal{P} \approx 1$. Consequently, the (non-coarse-grained) density factor will satisfy $\mathcal{F}_{\text{geo}} \approx \mathcal{S}$. Additionally, in this or in any other situation in which the sinking layer remains nearly horizontal during all the settling process, the stretching factor can be approximated as (see equation (C.9)) $\exp\left(-\int_{t_0}^{t_z} \nabla_{\text{h}} \cdot \mathbf{v} dt'\right)$, where $\nabla_{\text{h}} \cdot \mathbf{v} = \partial_x v_x + \partial_y v_y$ is the horizontal divergence of the velocity field. This exponential expression for the density factor was proposed heuristically in [114] and found to be a reasonable approximation (see Section 4.5). Note that $\exp\left(-\int_{t_0}^{t_z} \nabla_{\text{h}} \cdot \mathbf{v} dt'\right)$ can be transformed to $\exp\left(\int_{t_0}^{t_z} \partial_z v_z dt'\right)$ by taking into account

incompressibility. This means that the stretching factor (and thus the complete density factor) can be obtained from the temporal average of the vertical shear felt by the falling particles when the falling sheet remains almost horizontal, e.g. for high settling velocities. Although $\mathcal{S} \approx 1$ as well in this case, our numerical experience indicates that \mathcal{S} tends to 1 slower than \mathcal{P} for increasing settling velocity, and the evaluation of the discussed exponential expression thus becomes sound

For small settling velocities, the trends of the curves in Figure 5.5 reverse: the importance of stretching increases again with respect to projection. This may be a consequence of the phenomenon observed by [40] in a simplified kinematic flow: effects due to tiltiness (which determines \mathcal{P}) saturate for long settling times or small settling velocities, whereas effects due to stretching can grow to arbitrarily large values. The power-law behavior of the standard deviation of \mathcal{P} identified in Fig. 5.6b could contradict this explanation, but the lines in this figure actually deviate downward from the power law for long settling times.

5.4.2 About the presence of extreme inhomogeneities and caustics

We found extremely large values of the geometric density factor, and thus of the accumulated density, in particular locations (see Figure 5.7) of the collecting surface. We associate them to configurations close to *projection caustics* [40]. These are locations where the direction of the velocity \mathbf{v} and the direction normal to the layer of particles, \mathbf{n} , become perpendicular so that

$$\cos \gamma \equiv \mathbf{n} \cdot \frac{\mathbf{v}}{v} = 0, \quad (5.14)$$

and then the projection factor \mathcal{P}_{geo} (equation (5.6)) becomes infinite. Geometrically, the condition in equation (5.14) occurs when the falling surface appears folded when projected on the collecting surface along the direction of motion.

Numerical values for $\cos \gamma = \mathbf{n} \cdot \mathbf{v}/v$ are shown in Figure 5.8 for the same simulation as in Figure 5.7. It becomes obvious that most of the high values of the density factor in Figure 5.7 arise where $\cos \gamma$ takes small values, i.e. a situation close to produce a projection caustic (i.e. diverging density values located where equation (5.14) is satisfied). In generic three-dimensional flows in which the falling surface folds while sinking, caustics will occur as one-dimensional curves on the collecting surface, across which the sign of $\cos \gamma$ would change. Figure 5.8, however, shows small but non-vanishing values of $\cos \gamma$, and sign reversal does not occur. In contrast with generic threedimensional flows, the setting in oceanic flows, at least at the mesoscales we are considering, has special properties. As mentioned, even an initially horizontal particle layer would become tilted, but gradients in the vertical velocity component are small in the ocean [91], so the tiltiness (the direction of the normal vector \mathbf{n}) cannot change very much (in other words, folds are strongly disfavored). Therefore, the particles must have nearly horizontal local velocity \mathbf{v} in order to have it perpendicular to \mathbf{n} and caustics to appear. Actually,

the vertical component of the velocity field of the fluid is orders of magnitude smaller than horizontal components in the ocean, even in the Benguela region, which contains upwelling cells [147] with enhanced vertical flows. The addition of the settling velocity \mathbf{v}_s increases the magnitude of the vertical component of the particle velocity \mathbf{v} , although it still remains much smaller than the horizontal components. Consequently, \mathbf{v} is close to horizontal (in other words, the approach angle to the accumulation depth is low [163, 20]). However, the sinking velocity $v_s = 50$ m/day used in Figures 5.7 and 5.8 is still large enough, so that the perpendicularity property required by equation (5.14) is not really achieved, although it is closely approached in particular locations of the collecting surface. We expect that locations with higher densities, and eventually true projection caustics, would appear if using smaller values of v_s . Additionally, one may suspect that a longer sinking time, which is implied by a smaller settling velocity, gives more opportunity to form foldings and to larger deviation of \mathbf{n} from vertical. The practical implication of this is that, as far of the effect of the projection factor \mathcal{P} is concerned, very small or light particles, which have small v_s , will present a much more irregular settling distribution than the ones falling faster. This is indeed the trend observed in Figures 5.3 and 5.6.

We note that, as shown in [40], the extremely high values involved in caustics are smoothed out if a full three-dimensional volume of particles is considered to sink instead of a thin layer. Also, any coarse-graining is expected to efficiently filter out extremely high density values, even for a small coarse-graining radius R , as our results in section 5.3 suggest. Thus, we can conclude that true projection caustics will not be readily observed in distributions of settling particles in ocean flows, but they will leave a trace of highly inhomogeneous distributions for the lighter and smaller types of particles.

5.4.3 Other aspects

Figure 5.5a shows that the agreement between our calculation of $\mathcal{F}_{\text{hist}}^R$ and $\mathcal{F}_{\text{geo}}^R$ deteriorates with increasing values of the settling velocity t_s (and also at very small values of it). Besides the technical differences arising from their definitions, the main physical difference between them is that $\mathcal{F}_{\text{geo}}^R$ has been computed using exclusively a mesoscale flow, whereas an additional noise term has been included in the calculation of $\mathcal{F}_{\text{hist}}^R$. This term is a crude way to introduce flow scales below mesoscales. In any case, a good agreement between $\mathcal{F}_{\text{hist}}^R$ and $\mathcal{F}_{\text{geo}}^R$ in Figures 5.4 and 5.5a should be interpreted as a confirmation of the insensitivity of the density factor to particular types of flow perturbations below mesoscale. In particular, from Figure 5.5a we see that the best agreement occurs for values of t_s for which the dominant source of inhomogeneity is the projection factor.

In general, we find larger density inhomogeneities (Figures (5.3) and (5.7)) in the southern part of the domain studied. This is presumably related to the stronger turbulence present in this southern part of the Benguela region as discussed in [70] for the horizontal circulation in the upper ocean layers, which would indicate that turbulence enhances the inhomogeneities in the settling process. This is not surprising since stronger turbulence would introduce more spatial variability in all relevant processes [55].

CHAPTER 6

Conclusions

We have used the Lagrangian Flow Network (LFN) framework to study the structure of marine populations through the computation of complementary connectivity metrics (Chapter 2). The LFN methodology also allows studying their spatio-temporal variability and discussing their relationships with both ecological and oceanographic processes. It permits depicting larval retention and exchange at multiple-scales, studying inter-relationships among connectivity metrics, informing the sampling strategy and interpretation of genetic datasets and appraising the implications of connectivity processes in the design of marine reserves and in the management of harvested populations.

We have analysed the global robustness and sensitivity of four connectivity metrics measuring the exchange and retention of larvae derived from the LFN framework (Chapter 3). The most important numerical and biophysical parameters were extensively tested over large ranges. Despite the fact that our proxies are sensitive at different degrees to all parameters, we evidenced general relationships that demonstrated the robustness and identified the limitations of such particle-tracking models. In particular, we found an optimum particle density that ensures the best ratio computational cost/information obtained. We assessed the impacts of the scale of discretization (node size) and we provided hints on how to select them adequately according to the study objectives. The consequences of uncertainties about the PLD and the modality of spawning were systematically explored and related to the spatio-temporal variability of the underlying velocity field. Such variability can be characterized by the Lagrangian correlation time: a measure of the time-scale at which fluid velocities become uncorrelated. We found that retention metrics are always more robust to the temporal variability of ocean currents than exchange metrics.

Our results help to designing suitable experiments with the LFNs, as well as with other offline particle-tracking model, to address specific ecological questions and they allow evaluating the reliability one may give to modelled connectivity estimates. These results, the methodologies we employed and more generally the LFN modelling framework are equally applicable to the study of other passively-transported materials (oils spills, micro-pastics...). Future perspectives are to relate the robustness of these Lagrangian metrics to physical quantities of the flow and to extend our analyses by including complex biological traits and larval behaviors.

We have studied the problem of sinking particles in a realistic oceanic flow, focussing on the range of sizes and densities appropriate for marine biogenic particles (Chapter 4). Starting from a modeling approach in terms of the MRG Eq. (1.50), our conclusion is that the simplest approximation given by Eq. (4.7) in which particles move passively

with the fluid flow with an added constant settling velocity in the vertical direction is an accurate framework to describe the sinking process in the types of flows and particles considered. A re-assessment of these assumptions may be required if more complex processes (such as aggregation/disaggregation) are included and when super-high resolution (submesoscale and below) mimicking the real ocean becomes available.

Corrections arising from the Coriolis force turn out to be about 100 times larger than the ones coming from inertial effects, in agreement with the results in [155] or in [13], but both of them are negligible when compared to the effects of passive transport by the fluid velocity plus the added gravity term, except for very slowly sinking particles at high latitudes.

If the fluid flow field $\mathbf{v}(\mathbf{r}, t)$ has vanishing divergence, then the same is true for the particle velocity field defined by the approximation in Eq. (4.7). Then, no three-dimensional clustering can occur within this approximation. Nevertheless, we have shown that two-dimensional cuts or projections of evolving three-dimensional particle clouds display horizontal clustering.

We have shown that common types of particles of biogenic origin, when sedimenting towards the deep ocean, do so in an inhomogeneous manner that we have characterized with the horizontal dependence of the accumulated density at a given depth, or equivalently with a density factor that expresses the ratio between this accumulated density and the density at the depth where they were initially released (Chapter 5). These inhomogeneities are present even if particles are produced in a completely homogeneous manner in the upper ocean layers, and they arise from the effects of the flow while the particles are sinking.

For the case of particles homogeneously initialized in a horizontal sheet close to the ocean surface, we have improved analytical expressions derived earlier [40] that allow to identify the mechanisms leading to the measured inhomogeneities: stretching of the falling sheet, and projection of it on a deep horizontal surface when the particles reach that depth. For large settling velocities, the stretching mechanism becomes dominant, and projection gains relevance for smaller settling velocities or, equivalently, for longer settling times. The degree of inhomogeneity grows as the settling time increases. We observe numerically that this growth follows specific power laws for each of the two mechanisms involved. Further work would try to find analytical explanations for them.

In a range of settling velocities, our results are robust to the introduction of noise-type flow perturbations which try to model small scale processes not included in the mesoscale flow in the Benguela region on which we have implemented our numerical experiments. Within a reasonable range, results are also robust to the size of the sampling size or the coarse-graining scale introduced to make consistent comparisons in our results.

The settling velocity has been one of the main parameters in terms of which we have presented our results, but we stress that changing the settling velocity is equivalent to considering different physical properties of the sinking particles (density and size), so that we are indeed scanning a variety of particle types. Faster sinking particles display weaker inhomogeneities in the accumulated density as compared to slowly sinking ones.

Our study has been limited to particles homogeneously initialized in a single horizontal sheet, but more general release configurations can be understood in terms of

this simplified setup [40]. A further limitation is posed by the biogeochemical and (dis)aggregation processes occurring during the sedimentation process, which are neglected in our framework and would need to be considered in future studies.

APPENDIX A

Coriolis Theorem and acceleration in non-inertial frames

Let consider two reference frames S and \hat{S} , with orthonormal vector basis $(\mathbf{e}_1, \mathbf{e}_2, \mathbf{e}_3)$ and $(\hat{\mathbf{e}}_1, \hat{\mathbf{e}}_2, \hat{\mathbf{e}}_3)$ respectively, and we assume, for simplicity, that they share the same origin O . By orthonormality condition we have

$$\mathbf{e}_i \cdot \mathbf{e}_j = \delta_{ij} = \hat{\mathbf{e}}_i \cdot \hat{\mathbf{e}}_j \quad (\text{A.1})$$

where δ_{ij} is the Kronecker delta¹. The following matrix $M_{ij} = \mathbf{e}_i \cdot \hat{\mathbf{e}}_j$ determines the relative orientation of the reference frames and allows to express the components of one vector basis of the other basis

$$\mathbf{e}_i = M_{ij} \hat{\mathbf{e}}_j, \quad (\text{A.2})$$

$$\hat{\mathbf{e}}_i = M_{ji} \mathbf{e}_j. \quad (\text{A.3})$$

The time derivative of a scalar quantity is independent of the reference frame, however take the derivative of a vector depend on relative motion of the reference frame. The relation of \mathbf{v} , the time derivative of a vector \mathbf{r} in reference frame S , with $\hat{\mathbf{v}}$, the time derivative of the same vector in \hat{S} , can be obtained applying transformation equations to the derivative definition [184]

$$\hat{\mathbf{v}} = \frac{d\hat{\mathbf{r}}}{dt} = \frac{d}{dt}(r_i \mathbf{e}_i) = \frac{d}{dt}(r_i M_{ij} \hat{\mathbf{e}}_j) = \mathbf{v} + H_{ik} r_i \mathbf{e}_k \quad (\text{A.4})$$

where we have defined

$$H_{ij} = \frac{dM_{ik}}{dt} M_{jk}.$$

This matrix \mathbf{H} is antisymmetric, this can be proved using the transformation equation (A.2) to rewrite orthonormality condition (A.1) in terms of \mathbf{M}

$$\delta_{ij} = M_{ik} M_{jk},$$

¹The Kronecker delta is defined by $\delta_{ij} = \begin{cases} 1 & i = j \\ 0 & i \neq j \end{cases}$.

and taking the time derivative

$$\frac{dM_{ik}}{dt}M_{jk} + M_{ik}\frac{dM_{jk}}{dt} = 0 \Rightarrow H_{ij} + H_{ji} = 0, \quad (\text{A.5})$$

we obtain that \mathbf{H} is indeed antisymmetric. This result (A.5) implies that \mathbf{H} has only three independent components, so that it can be expressed by

$$H_{ij} = \epsilon_{kij}\Omega_k \quad (\text{A.6})$$

where ϵ_{ijk} is the Levi-Civita symbol² and the vector $\mathbf{\Omega} = \Omega_i\mathbf{e}_i$ corresponds to the relative angular velocity of S respect to \hat{S} . Substituting the definition (A.6) on (A.4) we identify the last term with the vectorial product definition in Einstein notation³ which allow us to write the equation (A.4) in fully vectorial form

$$\hat{\mathbf{v}} = \mathbf{v} + \mathbf{\Omega} \times \mathbf{r} \quad (\text{A.7})$$

which corresponds to the Coriolis theorem. However, since \mathbf{r} is an arbitrary vector, the expression (A.7) is equivalent to the operator equation

$$\frac{\hat{d}}{dt} = \frac{d}{dt} + \mathbf{\Omega} \times, \quad (\text{A.8})$$

and applying (A.8) to \mathbf{r} twice, we obtain the equation that relates the acceleration measured in both reference frames

$$\hat{\mathbf{a}} = \frac{\hat{d}^2\mathbf{r}}{dt^2} = \left[\frac{d}{dt} + \mathbf{\Omega} \times \right] \mathbf{r} = \mathbf{a} + 2\mathbf{\Omega} \times \mathbf{v} + \mathbf{\Omega} \times \mathbf{\Omega} \times \mathbf{r} \quad (\text{A.9})$$

²The Levi-Civita symbol can be defined as the scalar triple product of unit vectors in a right-handed coordinate system $\epsilon_{ijk} = \mathbf{e}_i \cdot (\mathbf{e}_j \times \mathbf{e}_k)$

³The vectorial product of two vector \mathbf{a} and \mathbf{b} using Einstein notation is $\mathbf{a} \times \mathbf{b} = \epsilon_{ijk}a_ib_j\mathbf{e}_k$

APPENDIX B

Velocity and acceleration in spherical coordinates

The spherical coordinates (ϕ, θ, r) , where ϕ is the longitude (angular distance eastwards), θ is the latitude (angular distance polewards) and r is the radial distance from the origin (see figure B.1), are related to the Cartesian coordinates (x, y, z) by

$$\begin{aligned}x &= r \cos \theta \cos \phi, \\y &= r \cos \theta \sin \phi, \\z &= r \sin \theta.\end{aligned}$$

Lets consider a position vector \mathbf{R} , its infinitesimal displacement $d\mathbf{R}$ is expressed in spherical coordinates by

$$d\mathbf{R} = \frac{\partial \mathbf{R}}{\partial \phi} d\phi + \frac{\partial \mathbf{R}}{\partial \theta} d\theta + \frac{\partial \mathbf{R}}{\partial r} dr, \quad (\text{B.1})$$

these three partial derivatives $\partial_\phi \mathbf{R}$, $\partial_\theta \mathbf{R}$ and $\partial_r \mathbf{R}$ correspond to a vectors mutually perpendicular, hence it is the natural candidate to an orthogonal basis for the spherical coordinates. The corresponding orthonormal basis $(\mathbf{e}_\phi, \mathbf{e}_\theta, \mathbf{e}_r)$ is obtained by vector normalization

$$\mathbf{e}_\phi = \frac{\partial_\phi \mathbf{R}}{\|\partial_\phi \mathbf{R}\|} = \frac{\partial_\phi \mathbf{R}}{\sqrt{(\partial_\phi x)^2 + (\partial_\phi y)^2 + (\partial_\phi z)^2}} = \frac{\partial_\phi \mathbf{R}}{r \cos \theta} \quad (\text{B.2})$$

$$\mathbf{e}_\theta = \frac{\partial_\theta \mathbf{R}}{\|\partial_\theta \mathbf{R}\|} = \frac{\partial_\theta \mathbf{R}}{\sqrt{(\partial_\theta x)^2 + (\partial_\theta y)^2 + (\partial_\theta z)^2}} = \frac{\partial_\theta \mathbf{R}}{r}, \quad (\text{B.3})$$

$$\mathbf{e}_r = \frac{\partial_r \mathbf{R}}{\|\partial_r \mathbf{R}\|} = \frac{\partial_r \mathbf{R}}{\sqrt{(\partial_r x)^2 + (\partial_r y)^2 + (\partial_r z)^2}} = \partial_r \mathbf{R}. \quad (\text{B.4})$$

Using these unit vector definitions (B.2),(B.3) and (B.4), the infinitesimal displacement (B.1) is recast by

$$d\mathbf{R} = r \cos \theta \mathbf{e}_\phi d\phi + r \mathbf{e}_\theta d\theta + \mathbf{e}_r dr. \quad (\text{B.5})$$

The expression of velocity \mathbf{V} in spherical coordinates is the time derivative of previous equation (B.5)

$$\mathbf{V} = u \mathbf{e}_\phi + v \mathbf{e}_\theta + w \mathbf{e}_r, \quad (\text{B.6})$$

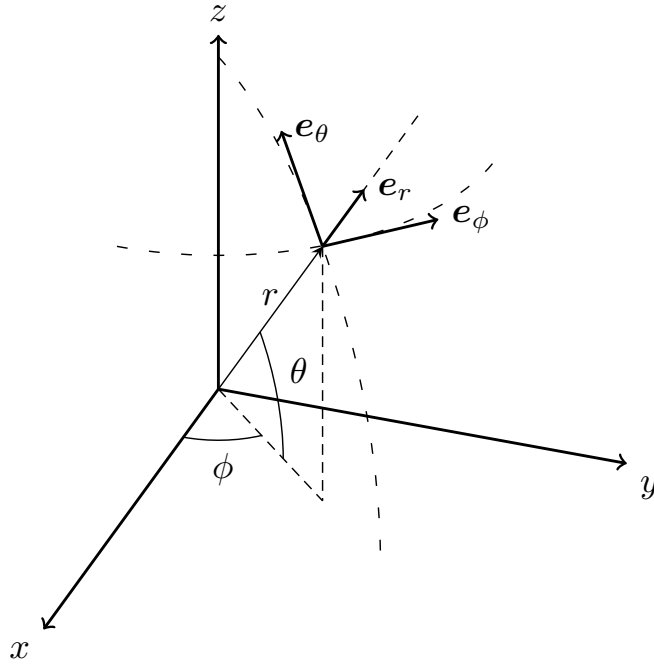


Figure B.1: The relation of Cartesian coordinates system (x, y, z) with spherical coordinate system (ϕ, θ, r) . The orthogonal unit vectors \mathbf{e}_ϕ , \mathbf{e}_θ and \mathbf{e}_r point in the direction of increasing longitude ϕ , latitude θ , and radial distance r , respectively.

where u is the zonal velocity, v is the meridional velocity and w is the vertical velocity. They are given by

$$u = r \cos \theta \frac{d\phi}{dt}, \quad v = r \frac{d\theta}{dt} \quad \text{and} \quad w = \frac{dr}{dt}. \quad (\text{B.7})$$

The acceleration is obtained differentiating again with respect to time expression (B.6)

$$\frac{d\mathbf{V}}{dt} = \frac{du}{dt} \mathbf{e}_\phi + \frac{dv}{dt} \mathbf{e}_\theta + \frac{dw}{dt} \mathbf{e}_r + u \frac{d\mathbf{e}_\phi}{dt} + v \frac{d\mathbf{e}_\theta}{dt} + w \frac{d\mathbf{e}_r}{dt}. \quad (\text{B.8})$$

We need to know the derivatives of the base vectors. The length of base vector is constant, but their orientation depends on basis location, therefore according to Coriolis theorem (A.7), their time derivatives may write by

$$\frac{d\mathbf{e}_\phi}{dt} = \mathbf{\Gamma} \times \mathbf{e}_\phi, \quad \frac{d\mathbf{e}_\theta}{dt} = \mathbf{\Gamma} \times \mathbf{e}_\theta \quad \text{and} \quad \frac{d\mathbf{e}_r}{dt} = \mathbf{\Gamma} \times \mathbf{e}_r, \quad (\text{B.9})$$

where $\mathbf{\Gamma}$ is the angular velocity of the vector basis. Substituting (B.9) on acceleration expression (B.8) results in

$$\frac{d\mathbf{V}}{dt} = \frac{du}{dt} \mathbf{e}_\phi + \frac{dv}{dt} \mathbf{e}_\theta + \frac{dw}{dt} \mathbf{e}_r + \mathbf{\Gamma} \times \mathbf{V}. \quad (\text{B.10})$$

The angular velocity $\mathbf{\Gamma}$ can be computed knowing how changes the orientation of the basis when varying each spherical coordinate separately. Changing r does not cause a rotation of the basis, while changing ϕ rotates about z axis and changing θ rotates about \mathbf{e}_ϕ , therefore the angular velocity of the vector basis $\mathbf{\Gamma}$ is given by

$$\mathbf{\Gamma} = -\frac{d\theta}{dt}\mathbf{e}_\phi + \frac{d\phi}{dt}\mathbf{k},$$

where \mathbf{k} is the unit vector on the z axis direction, which is expressed in the spherical vector basis

$$\mathbf{k} = \cos\theta\mathbf{e}_\theta + \sin\theta\mathbf{e}_r,$$

so that the angular velocity of the basis vector $\mathbf{\Gamma}$, taking into account (B.7), is

$$\mathbf{\Gamma} = -\frac{v}{r}\mathbf{e}_\phi + \frac{u}{r}\mathbf{e}_\theta + \frac{u \tan \theta}{r}\mathbf{e}_r, \quad (\text{B.11})$$

which allow to write the acceleration in spherical coordinates substituting (B.11) on (B.10)

$$\begin{aligned} \frac{d\mathbf{V}}{dt} &= \left(\frac{du}{dt} + \frac{uw}{r} - \frac{uw \tan \theta}{r} \right) \mathbf{e}_\phi \\ &+ \left(\frac{dv}{dt} + \frac{vw}{r} + \frac{u^2 \tan \phi}{r} \right) \mathbf{e}_\theta \\ &+ \left(\frac{dw}{dt} - \frac{u^2 + v^2}{r} \right) \mathbf{e}_r. \end{aligned} \quad (\text{B.12})$$

APPENDIX C

Density factor, geometrical approach

C.1 Stretching factor

Here we derive equation (5.5) for the stretching factor $\mathcal{S} \equiv dA_0/dA_{t_z}$, where dA_0 is an infinitesimal area element on the horizontal surface where the particle with trajectory $\mathbf{R} = \mathbf{R}(\mathbf{r}_0, t)$ was initialized at $t = t_0$, and dA_{t_z} is the area of that element after evolution until time t_z , when the particle reaches depth z . We denote the zonal, meridional and vertical components of the vectors involved as $\mathbf{R} = (X, Y, Z)$ and $\mathbf{r}_0 = (x_0, y_0, z_0)$.

Let $d_x \mathbf{R}(\mathbf{r}_0, t)$ be a vector giving the separation at all time of two particles that were initially separated by an infinitesimal distance dx_0 along the zonal direction on the initialization surface:

$$d_x \mathbf{R}(\mathbf{r}_0, t) \equiv \mathbf{R}(x_0 + dx_0, y_0, z_0, t) - \mathbf{R}(x_0, y_0, z_0, t) = \frac{\partial \mathbf{R}(\mathbf{r}_0, t)}{\partial x_0} dx_0 \equiv \boldsymbol{\tau}_x(t) dx_0, \quad (\text{C.1})$$

where we have introduced the vector $\boldsymbol{\tau}_x(t)$ as in equation (5.7). It is a vector tangent to the falling surface at any time. Since $\mathbf{R}(\mathbf{r}_0, t_0) = \mathbf{r}_0$, $\boldsymbol{\tau}_x(t_0)$ is a unit vector pointing in the zonal direction. Analogously we have

$$d_y \mathbf{R}(\mathbf{r}_0, t) \equiv \mathbf{R}(x_0, y_0 + dy_0, z_0, t) - \mathbf{R}(x_0, y_0, z_0, t) = \frac{\partial \mathbf{R}(\mathbf{r}_0, t)}{\partial y_0} dy_0 \equiv \boldsymbol{\tau}_y(t) dy_0. \quad (\text{C.2})$$

Let us choose as initial patch of area dA_0 in equation (5.4) the square spanned by the vectors $d_x \mathbf{R}(\mathbf{r}_0, t_0)$ and $d_y \mathbf{R}(\mathbf{r}_0, t_0)$, i.e., $dA_0 = dx_0 dy_0$. Since $d_x \mathbf{R}$ and $d_y \mathbf{R}$ are tangent to the falling patch at any time, their cross product $d_x \mathbf{R} \times d_y \mathbf{R}$ gives at any time a vector normal to it (i.e. in the direction of the unit normal vector \mathbf{n}), with modulus dA_t giving the area of the patch. Thus

$$\mathbf{n} dA_t = d_x \mathbf{R} \times d_y \mathbf{R} = (\boldsymbol{\tau}_x(t) \times \boldsymbol{\tau}_y(t)) dx_0 dy_0 = (\boldsymbol{\tau}_x(t) \times \boldsymbol{\tau}_y(t)) dA_0. \quad (\text{C.3})$$

Particularizing to the time t_z at which the trajectory $\mathbf{R}(\mathbf{r}_0, t)$ reaches the accumulation surface at depth z , we find $\mathcal{S} = dA_0/dA_{t_z} = |\boldsymbol{\tau}_x(t_z) \times \boldsymbol{\tau}_y(t_z)|^{-1}$, as in equation (5.5).

An interesting expression can be obtained in the particular situation in which the falling surface remains horizontal at all times. In this case, the vector $\boldsymbol{\tau}_x(t) \times \boldsymbol{\tau}_y(t)$ has only a vertical, z , component, which can be written in terms of a horizontal Jacobian determinant $|J_h|$:

$$\mathcal{S}^{-1} = (\boldsymbol{\tau}_x(t) \times \boldsymbol{\tau}_y(t))_z = |J_h| \equiv \left| \frac{\partial(X, Y)}{\partial(x_0, y_0)} \right| = \begin{vmatrix} \frac{\partial X}{\partial x_0} & \frac{\partial X}{\partial y_0} \\ \frac{\partial Y}{\partial x_0} & \frac{\partial Y}{\partial y_0} \end{vmatrix}. \quad (\text{C.4})$$

On the other hand, a standard equation for the time evolution of the three-dimensional Jacobian matrix $J_{ij} = \partial R_i / \partial x_{0j}$, $i, j = x, y, z$ can be obtained:

$$\frac{d}{dt} J_{ij} = \frac{d}{dt} \frac{\partial R_i}{\partial x_{0j}} = \frac{\partial v_i}{\partial x_{0j}} = \sum_{k=x,y,z} \frac{\partial v_i}{\partial R_k} \frac{\partial R_k}{\partial x_{0j}} = \sum_{k=x,y} \frac{\partial v_i}{\partial R_k} \frac{\partial R_k}{\partial x_{0j}} + \frac{\partial v_i}{\partial Z} \frac{\partial Z}{\partial x_{0j}}, \quad i, j = x, y, z. \quad (\text{C.5})$$

In the last equality we have separated the contribution from the vertical coordinate, and all derivatives there are taken at constant t . We recognize that the matrix J_h whose determinant appears in equation (C.4) has the components of J_{ij} with $i, j = x, y$. Thus:

$$\frac{d}{dt} (J_h)_{ij} = \sum_{k=x,y} \frac{\partial v_i}{\partial R_k} \frac{\partial R_k}{\partial x_{0j}} + \frac{\partial v_i}{\partial Z} \frac{\partial Z}{\partial x_{0j}}, \quad i, j = x, y. \quad (\text{C.6})$$

Under the assumption that the falling surface remains horizontal at all times, we have $\partial Z / \partial x_{0j} = 0$ for $j = x, y$ and then equation (C.6) can be written in matrix form as

$$\frac{d}{dt} J_h = (\nabla_h \mathbf{v}_h)^T J_h. \quad (\text{C.7})$$

$\nabla_h \mathbf{v}_h$ is the horizontal velocity gradient matrix containing the derivatives of the horizontal components of the velocity with respect to the horizontal coordinates. The superindex T indicates transpose.

From equation (C.7):

$$\frac{1}{|J_h|} \frac{d|J_h|}{dt} = \text{Tr} \left(\frac{dJ_h}{dt} J_h^{-1} \right) = \text{Tr} (\nabla_h \mathbf{v}_h) = \nabla_h \cdot \mathbf{v}_h, \quad (\text{C.8})$$

where we have used the Jacobi formula in the first equality ($\text{Tr}(M)$ means trace of the matrix M). $\nabla_h \cdot \mathbf{v}_h = \partial_x v_x + \partial_y v_y$ is the horizontal divergence of the particle velocity field, which is, since the settling velocity is constant, also the horizontal divergence of the fluid velocity field. Finally, combining (C.4) and (C.8), we obtain

$$\mathcal{S} = e^{-\int_{t_0}^t \nabla_h \cdot \mathbf{v}_h dt'}. \quad (\text{C.9})$$

Because of fluid incompressibility $\nabla_h \cdot \mathbf{v}_h = -\partial_z v_z$, one can also write

$$\mathcal{S} = e^{\int_{t_0}^t \partial_z v_z dt'}. \quad (\text{C.10})$$

Equations (C.9)-(C.10) give also the total density factor, $\mathcal{F} = \mathcal{S}$, since for a horizontal surface the projection factor \mathcal{P} is unity. They express stretching and the density factor for a horizontally falling surface in terms of the horizontal divergence and the vertical *shear* of the velocity field. Equation (C.9) was heuristically proposed in [114] and found to give a reasonable qualitative description of the density factor in the Benguela region. As a special case, (C.9) can also be obtained by assuming the projection factor tending to 1 faster than (C.9) itself when a parameter is changing (like \mathbf{v}_s as discussed in section 5.4.1). A more precise description, however, needs the use of the complete factor $\mathcal{F} = \mathcal{S}\mathcal{P}$ with stretching and projection given by equations (5.5) and (5.6).

As a generalization of equation (C.9) valid for arbitrary orientation of the falling surface, an expression alternative to equation (5.5) can be obtained manipulating equation (C.6). First we recognize that, for arbitrary orientation of the falling patch, $|J_h|$ gives the z component of the vector $\boldsymbol{\tau}_x(t) \times \boldsymbol{\tau}_y(t)$. Using equation (5.5) and the vertical component of equation (5.8) we have

$$n_z = |J_h|\mathcal{S}. \quad (\text{C.11})$$

Now, using the full form of equation (C.6), equation (C.8) is replaced by

$$\frac{1}{|J_h|} \frac{d|J_h|}{dt} = Tr \left(\frac{dJ_h}{dt} J_h^{-1} \right) = \nabla_h \cdot \mathbf{v}_h + \nabla_h Z \cdot \partial_z \mathbf{v}_h, \quad (\text{C.12})$$

where $z = Z(x, y; t)$ gives the time-dependent depth of the falling surface in terms of the horizontal coordinates. In the last term we have used the chain rule involving $(J_h^{-1})_{ij} = \partial x_{0i} / \partial R_j$ for $i, j = x, y$. This expression is true if x_{0i} is expressed as a function of X and Y , with z_0 a parameter which is kept constant. From equations (C.11) and (C.12) we get

$$\mathcal{S} = n_z e^{-\int_{t_0}^t (\nabla_h \cdot \mathbf{v}_h + \nabla_h Z \cdot \partial_z \mathbf{v}_h) dt'}. \quad (\text{C.13})$$

We note that the integrand in the exponent of this last expression is $\partial_x v_x(x, y, Z(x, y; t); t) + \partial_y v_y(x, y, Z(x, y; t); t)$. Equation (C.13) reduces to (C.9) for a horizontal surface ($\nabla_h Z = 0$ and $n_z = 1$).

C.2 Numerical computation of the geometrical density factor

In the setup of our numerical experiment, the density inhomogeneities arise during the sedimentation of a particle layer initialized horizontally at a depth of 100m. The numerical evaluation of the density factor is applied separately for every particle trajectory tracked, so that it is obtained at each horizontal location \mathbf{x} where the particle tracked reaches the collecting surface.

The tracked particle, which started at position \mathbf{r}_0 in the initial layer at time t_0 , has trajectory $\mathbf{R}(\mathbf{r}_0, t)$. In order to numerically compute the density factor $\mathcal{F}(\mathbf{x})$ at its ending location at a depth of 1000m, we initialize four auxiliary particle trajectories, with initial positions modified in the zonal and meridional direction. These auxiliary trajectories are given by $\mathbf{R}(\mathbf{r}_0 \pm \boldsymbol{\delta}_x, t)$ and $\mathbf{R}(\mathbf{r}_0 \pm \boldsymbol{\delta}_y, t)$. The initial zonal and meridional distances $|\boldsymbol{\delta}_x|$ and $|\boldsymbol{\delta}_y|$ are chosen to be $\delta = 10$ km in the numerical experiments (zonal and meridional distances are expressed in terms of longitude ϕ and latitude θ in radians by $x = \mathcal{R}\phi \cos \theta$ and $y = \mathcal{R}\theta$, where \mathcal{R} is the radius of the Earth). Thanks to these auxiliary particle trajectories we compute the two tangent vectors of the particle layer using finite differences

$$\begin{aligned}\boldsymbol{\tau}_x &\simeq \frac{\mathbf{R}(\mathbf{r}_0 + \boldsymbol{\delta}_x, t) - \mathbf{R}(\mathbf{r}_0 - \boldsymbol{\delta}_x, t)}{2\delta}, \\ \boldsymbol{\tau}_y &\simeq \frac{\mathbf{R}(\mathbf{r}_0 + \boldsymbol{\delta}_y, t) - \mathbf{R}(\mathbf{r}_0 - \boldsymbol{\delta}_y, t)}{2\delta}.\end{aligned}\quad (\text{C.14})$$

These tangent vectors $\boldsymbol{\tau}_x$, $\boldsymbol{\tau}_y$ and the velocity \mathbf{v} of the reference trajectory at its ending position are used to compute the stretching factor \mathcal{S} from equation (5.5) and the projection factor \mathcal{P} from equation (5.6).

However, long integration times t result in inaccurate estimations of the tangent vectors $\boldsymbol{\tau}_x$ and $\boldsymbol{\tau}_y$, because auxiliary particle trajectories move away excessively from the reference trajectory and leave the region where the estimation in equations (C.14) remains valid. We solve this issue by resetting the distance, with respect to the reference trajectory, and the orientation of the auxiliary trajectories to their initial configuration after each time interval of $\Delta t = 1.5$ days using

$$\begin{aligned}\mathbf{R}(\mathbf{r}_0 \pm \boldsymbol{\delta}_x, t) &\rightarrow \mathbf{R}(\mathbf{r}_0, t) \pm \delta \frac{\boldsymbol{\tau}_x}{|\boldsymbol{\tau}_x|}, \\ \mathbf{R}(\mathbf{r}_0 \pm \boldsymbol{\delta}_y, t) &\rightarrow \mathbf{R}(\mathbf{r}_0, t) \pm \delta \frac{\boldsymbol{\tau}_y}{|\boldsymbol{\tau}_y|} \times \mathbf{n}.\end{aligned}$$

This renormalization procedure requires to store the value of the stretching factor \mathcal{S} after every time interval Δt , with

$$\mathcal{S}(t_0 + k\Delta t) = |\boldsymbol{\tau}_x(t_0 + k\Delta t) \times \boldsymbol{\tau}_y(t_0 + k\Delta t)|^{-1}. \quad (\text{C.15})$$

The total stretching factor at the ending position (after n time steps) is obtained as the product of the intermediate values:

$$\mathcal{S} = \prod_{k=1}^n \mathcal{S}(t_0 + k\Delta t). \quad (\text{C.16})$$

Once the stretching factor \mathcal{S} and the projection factor \mathcal{P} are numerically computed, their product gives the estimation of $\mathcal{F}_{\text{geo}}(\mathbf{x})$, the density factor at the arrival point in the collecting surface, based on geometrical considerations.

C.3 Coarse-graining of the geometrical density factor

The geometrical computation of the density factor obtains the value of $\mathcal{F}_{\text{geo}}(\mathbf{x}_i)$ at the endpoint \mathbf{x}_i of each of the particles tracked until the collecting surface. The direct sampling calculation, however, gives a value $\mathcal{F}_{\text{hist}}^R(\mathbf{x})$ associated to circles of radius R around the sampling locations \mathbf{x} . In order to compare the two quantities we have to make some average or coarse-graining of the values of $\mathcal{F}_{\text{geo}}(\mathbf{x}_i)$ falling inside each of the sampling circles. But a simple arithmetic mean will have a bias to high values, because more particles fall in regions with higher density.

The appropriate approach is as follows: The coarse-grained value of the geometric density factor, $\mathcal{F}_{\text{geo}}^R$, should be given by the ratio between the value of the accumulated density σ_z^R on the lower surface, measured in one of the sampling circles of radius R , and the initial density σ_0 . In the lower surface we have $\sigma_z^R = n_R/A_{\text{acc}}^R$, where $A_{\text{acc}}^R = \pi R^2$ is the area of one of the sampling circles and n_R is the number of particles landing there. If we track back in time the trajectories of all points in this final area we will get an initial area A_0 containing the same number of particles n_R at the initial time. Thus,

$$\mathcal{F}_{\text{geo}}^R \equiv \frac{\sigma_z^R}{\sigma_0} = \frac{A_0}{A_{\text{acc}}^R}. \quad (\text{C.17})$$

Section 5.2.4 contains expressions for the evaluation of the ratio of areas in equation (C.17) when they are infinitesimal patches. But in general A_0 and A_{acc}^R will be too large to apply such expressions. We can solve this issue by noticing that we initialize the particles in the upper layer in a regular grid in zonal and meridional distances, so that we can associate the same small area a_0 (for example that of the unit cell of the grid or of the Voronoi cell) to each of the particles in the initial surface. Then, we can approximate the initial area A_0 by summing up all the small areas a_0 corresponding to each of the n_R particles that will reach the sampling circle in the lower surface:

$$A_0 \simeq n_R a_0. \quad (\text{C.18})$$

If we use many particles so that they are initially very closely spaced, a_0 will be very small, and we can use the expression valid for the ratio of infinitesimal patches:

$$a_{\text{acc},i} \simeq \frac{1}{\mathcal{F}_{\text{geo}}(\mathbf{x}_i)} a_0, \quad (\text{C.19})$$

where $a_{\text{acc},i}$ is the area of the footprint left around the final location \mathbf{x}_i by the settling of the small patch of initial area a_0 . The final area A_{acc}^R will be now covered by the areas $a_{\text{acc},i}$:

$$A_{\text{acc}}^R \simeq \sum_i^{n_R} a_{\text{acc},i}. \quad (\text{C.20})$$

The combination of equations (C.17)-(C.20) gives

$$\mathcal{F}_{\text{geo}}^R \simeq \frac{n_R}{\sum_{i=1}^{n_R} \frac{1}{\mathcal{F}_{\text{geo}}(\mathbf{x}_i)}}. \quad (\text{C.21})$$

That is, the proper estimation of the density factor in a finite area corresponds to the harmonic mean of the geometrical density factors of the trajectories involved, equation (5.11). Note that exact equalities hold for infinitely many particles.

Bibliography

- ¹M. R. Allshouse and T. Peacock, “Lagrangian based methods for coherent structure detection”, *Chaos: An Interdisciplinary Journal of Nonlinear Science* **25**, 097617 (2015) (cit. on p. 15).
- ²D. Alvarez-Berastegui, L. Ciannelli, A. Aparicio-Gonzalez, P. Reglero, M. Hidalgo, J. L. López-Jurado, J. Tintoré, and F. Alemany, “Spatial scales, means and gradients of hydrographic variables define pelagic seascapes of bluefin and bullet tuna spawning distribution”, *PLoS ONE* **9**, e109338 (2014) (cit. on p. 48).
- ³M. Andrello, D. Mouillot, J. Beuvier, C. Albouy, W. Thuiller, and S. Manel, “Low connectivity between mediterranean marine protected areas: a biophysical modeling approach for the dusky grouper *Epinephelus marginatus*”, *PLoS ONE* **8**, e68564 (2013) (cit. on pp. 27, 38).
- ⁴C. D. Argyropoulos and N. C. Markatos, “Recent advances on the numerical modelling of turbulent flows”, *Applied Mathematical Modelling* **39**, 693–732 (2015) (cit. on p. 9).
- ⁵T. R. Auton, J. C. R. Hunt, and M. Prud’Homme, “The force exerted on a body in inviscid unsteady non-uniform rotational flow”, *Journal of Fluid Mech.* **197**, 241–257 (1988) (cit. on pp. 20, 21).
- ⁶K. Azetsu-Scott and U. Passow, “Ascending marine particles: significance of transparent exopolymer particles (TEP) in the upper ocean”, *Limnology and Oceanography* **49**, 741–748 (2004) (cit. on p. 66).
- ⁷R. Balbín, J. López-Jurado, M. Flexas, P. Reglero, P. Vélez-Velchí, C. González-Pola, J. Rodríguez, A. García, and F. Alemany, “Interannual variability of the early summer circulation around the Balearic Islands: driving factors and potential effects on the marine ecosystem”, *Journal of Marine Systems* (2013) (cit. on pp. 35, 36).
- ⁸W. M. Balch, B. C. Bowler, D. T. Drapeau, A. J. Poulton, and P. M. Holligan, “Biominerals and the vertical flux of particulate organic carbon from the surface ocean”, *Geophysical Research Letters* **37**, L22605 (2010) (cit. on p. 64).
- ⁹E. Balkovsky, G. Falkovich, and A. Fouxon, “Intermittent distribution of inertial particles in turbulent flows”, *Phys. Rev. Lett.* **86**, 2790–2793 (2001) (cit. on pp. 22, 66, 68, 75).
- ¹⁰J. Bec, “Fractal clustering of inertial particles in random flows”, *Physics of Fluids* **15**, 81–84 (2003) (cit. on p. 69).

- ¹¹J. Bec, L. Biferale, M. Cencini, A. Lanotte, S. Musacchio, and F. Toschi, “Heavy particle concentration in turbulence at dissipative and inertial scales”, *Phys. Rev. Lett.* **98**, 084502 (2007) (cit. on p. 69).
- ¹²J. Bec, H. Homann, and S. S. Ray, “Gravity-driven enhancement of heavy particle clustering in turbulent flow”, *Phys. Rev. Lett.* **112**, 184501 (2014) (cit. on pp. 69, 72).
- ¹³F. J. Beron-Vera, M. J. Olascoaga, G. Haller, M. Farazmand, J. Triñanes, and Y. Wang, “Dissipative inertial transport patterns near coherent Lagrangian eddies in the ocean”, *Chaos* **25**, 087412 (2015) (cit. on pp. 69, 100).
- ¹⁴S. Berti, F. Alves Dos Santos, G. Lacorata, and A. Vulpiani, “Lagrangian drifter dispersion in the Southwestern Atlantic Ocean”, *Journal of Physical Oceanography* **41**, 1659–1672 (2011) (cit. on p. 52).
- ¹⁵J. H. Bettencourt, C. López, and E. Hernández-García, “Oceanic three-dimensional Lagrangian coherent structures: A study of a mesoscale eddy in the Benguela upwelling region”, *Ocean Modelling* **51**, 73–83 (2012) (cit. on p. 73).
- ¹⁶L. Biferale, F. Bonaccorso, I. M. Mazzitelli, M. A. T. van Hinsberg, A. S. Lanotte, S. Musacchio, P. Perlekar, and F. Toschi, “Coherent structures and extreme events in rotating multiphase flows”, *Phys. Rev. X* **6**, 041036 (2016) (cit. on p. 67).
- ¹⁷L. Bostford, J. White, M. Coffroth, C. Paris, S. Planes, T. Shearer, S. Thorrold, and G. Jones, “Connectivity and resilience of coral reef metapopulations in marine protected areas: matching empirical efforts to predictive needs”, *Coral Reefs* **28**, 327–337 (2009) (cit. on p. 35).
- ¹⁸D. Brickman and P. C. Smith, “Lagrangian stochastic modeling in coastal oceanography”, *J. Atmos. Oceanic Technol.* **19**, 83–99 (2002) (cit. on p. 70).
- ¹⁹T. Brochier, C. Lett, and P. Fréon, “Investigating the northern Humboldt paradox from model comparisons of small pelagic fish reproductive strategies in Eastern Boundary Upwelling ecosystems”, *Fish and Fisheries* **12**, 94–109 (2011) (cit. on pp. 47, 52, 59).
- ²⁰K. O. Buesseler et al., “An assessment of the use of sediment traps for estimating upper ocean particle fluxes”, *J. Marine Res.* **65**, 345–416 (2007) (cit. on pp. 62, 74, 79, 97).
- ²¹S. C. Burgess, K. J. Nickols, C. D. Griesemer, L. A. K. Barnett, A. G. Dedrick, E. V. Satterthwaite, L. Yamane, S. G. Morgan, J. W. White, and L. W. Botsford, “Beyond connectivity: how empirical methods can quantify population persistence to improve marine protected-area design”, *Ecological Applications* **24**, 257–270 (2014) (cit. on p. 28).
- ²²S. Cadrin and D. Secor, *Accounting for spatial population structure in stock assessment: past, present, and future*. (Springer, 2019) (cit. on p. 35).

- ²³A. Calò, F. C. Félix-Hackradt, J. Garcia, C. W. Hackradt, D. Rocklin, J. Treviño Otón, and J. A. García-Charton, “A review of methods to assess connectivity and dispersal between fish populations in the Mediterranean Sea”, *Advances in Oceanography and Limnology* **4**, 150–175 (2013) (cit. on pp. 26, 37, 38).
- ²⁴X. Capet, J. C. McWilliams, M. J. Molemaker, and S. F., “Mesoscale to submesoscale transition in the California current system. Part I: flow structure, eddy flux, and observational tests”, *Journal of Physical Oceanography* **38**, 29–43 (2008) (cit. on p. 26).
- ²⁵M. H. Carr, J. E. Neigel, J. A. Estes, S. Andelman, R. R. Warner, and J. L. Largier, “Comparing marine and terrestrial ecosystems: implications for the design of coastal marine reserves”, *Ecological Applications* **13**, 90–107 (2003) (cit. on p. 26).
- ²⁶J. H. E. Cartwright, U. Feudel, G. Károlyi, A. de Moura, O. Piro, and T. Tél, “Dynamics of finite-size particles in chaotic fluid flows”, in *Nonlinear dynamics and chaos: advances and perspectives*, edited by M. Thiel, J. Kurths, M. C. Romano, G. Károlyi, and A. Moura (Springer Berlin Heidelberg, Berlin, Heidelberg, 2010), pp. 51–87 (cit. on pp. 21, 22, 62, 66, 69).
- ²⁷M. Cencini, F. Cecconi, and A. Vulpiani, *Chaos* (World Scientific, 2009) (cit. on pp. 4, 23).
- ²⁸D. B. Chelton, M. G. Schlax, and R. M. Samelson, “Global observations of nonlinear mesoscale eddies”, *Progress in Oceanography* **91**, 167–216 (2011) (cit. on p. 4).
- ²⁹S. W. Chisholm, “Stirring times in the Southern Ocean”, *Nature* **407**, 685–687 (2000) (cit. on p. 14).
- ³⁰P. Ciais et al., “Carbon and other biogeochemical cycles”, in *Climate change 2013: the physical science basis. contribution of working group I to the fifth assessment report of the intergovernmental panel on climate change*, edited by T. Stocker, D. Qin, G. Plattner, M. Tignor, S. Allen, J. Boschung, A. Nauels, Y. Xia, V. Bex, and P. Midgley (Cambridge University Press, 2013) (cit. on pp. 12, 13).
- ³¹S. Clayton, S. Dutkiewicz, O. Jahn, and M. J. Follows, “Dispersal, eddies, and the diversity of marine phytoplankton”, *Limnology and Oceanography: Fluids and Environments* **3**, 182–197 (2013) (cit. on p. 26).
- ³²H. Corell, P. O. Moksnes, A. Engqvist, K. Doos, and P. Jonsson, “Depth distribution of larvae critically affects their dispersal and the efficiency of marine protected areas”, *Marine Ecology Progress Series* **467**, 29–46 (2012) (cit. on pp. 39, 58).
- ³³R. K. Cowen and S. Sponaugle, “Larval dispersal and marine population connectivity”, *Annual Review of Marine Science* **1**, 443–466 (2009) (cit. on pp. 26, 27).
- ³⁴M. Cuif, D. M. Kaplan, J. Lefèvre, V. M. Faure, M. Caillaud, P. Verley, L. Vigliola, and C. Lett, “Wind-induced variability in larval retention in a coral reef system: a biophysical modelling study in the South-West Lagoon of New Caledonia”, *Progress in Oceanography* **122**, 105–115 (2014) (cit. on pp. 38, 39, 56).

- ³⁵B. Cushman-Roisin and J. M. Beckers, eds., *Introduction to geophysical fluid dynamics. Physical and numerical aspects* (Elsevier, 2011) (cit. on p. 8).
- ³⁶A. Daitche and T. Tél, “Memory effects are relevant for chaotic advection of inertial particles”, *Phys. Rev. Lett.* **107**, 244501 (2011) (cit. on pp. 22, 67).
- ³⁷C. L. De La Rocha and U. Passow, “Factors influencing the sinking of POC and the efficiency of the biological carbon pump”, *Deep Sea Research Part II: Topical Studies in Oceanography* **54**, 639–658 (2007) (cit. on pp. 63, 79).
- ³⁸T. DeVries, P. F., and C. Deutsch, “The sequestration efficiency of the biological pump”, *Geophys. Res. Lett.* **39**, L13601 (2012) (cit. on p. 62).
- ³⁹W. G. Deuser, F. E. Muller-Karger, R. H. Evans, O. B. Brown, W. E. Esaias, and G. C. Feldman, “Surface-ocean color and deep-ocean carbon flux: how close a connection?”, *Deep Sea Research Part A. Oceanographic Research Papers* **37**, 1331–1343 (1990) (cit. on p. 80).
- ⁴⁰G. Drótos, P. Monroy, E. Hernández-García, and C. López, “Inhomogeneities and caustics in passive particle sedimentation in incompressible flows”, *Chaos* **29**, 013115 (1–25) (2019) (cit. on pp. 80, 82, 84, 86, 92, 96, 97, 100, 101).
- ⁴¹M. Drévillon et al., “The GODAE/Mercator-Ocean global ocean forecasting system: results, applications and prospects”, *Journal of Operational Oceanography* **1**, 51–57 (2008) (cit. on p. 11).
- ⁴²M. Dubois, V. Rossi, E. Ser-Giacomi, S. Arnaud-Haond, C. López, and E. Hernández-García, “Linking basin-scale connectivity, oceanography and population dynamics for the conservation and management of marine ecosystems”, *Global Ecology and Biogeography* **25**, 503–515 (2016) (cit. on pp. 26, 28, 30, 39, 43, 56).
- ⁴³A. Duputie and F. Massol, “An empiricist’s guide to theoretical predictions on the evolution of dispersal”, *Interface Focus* **3**, 20130028 (2013) (cit. on p. 26).
- ⁴⁴D. Elhmaidi, H. Nefzi, X. Carton, and T. Lili, “Particle dispersion in the Western Mediterranean Basin”, *The Open Oceanography Journal* **4**, 137–143 (2010) (cit. on p. 52).
- ⁴⁵T. Elperin, N. Kleeorin, and I. Rogachevskii, “Dynamics of particles advected by fast rotating turbulent fluid flows: fluctuations and large-scale structures”, *Phys. Rev. Lett.* **81**, 2898–2901 (2002) (cit. on p. 67).
- ⁴⁶G. Falkovich and M. G. Fouxon I. Stepanov, “Acceleration of rain initiation by cloud turbulence”, *Nature* **419**, 151–154 (2002) (cit. on p. 61).
- ⁴⁷H. Faxén, “Der Widerstand gegen die Bewegung einer starren Kugel in einer zähen Flüssigkeit, die zwischen zwei parallelen ebenen Wänden eingeschlossen ist”, *Annalen der Physik* **373**, 89–119 (1922) (cit. on pp. 20, 21).
- ⁴⁸R. Ferrari and C. Wunsch, “Ocean circulation kinetic energy: reservoirs, sources, and sinks”, *Annual Review of Fluid Mechanics* **41**, 253–282 (2009) (cit. on p. 14).
- ⁴⁹I. Fouxon, “Distribution of particles and bubbles in turbulence at a small Stokes number”, *Phys. Rev. Lett.* **108**, 134502 (2012) (cit. on p. 23).

- ⁵⁰G. Froyland, N. Santitissadeekorn, and A. Monahan, “Transport in time-dependent dynamical systems: finite-time coherent sets”, *Chaos: An Interdisciplinary Journal of Nonlinear Science* **20**, 043116 (2010) (cit. on p. 19).
- ⁵¹A. Garavelli L. Grüss, B. Grote, N. Chang, M. Smith, P. Verley, E. K. Stenevik, D. M. Kaplan, and C. Lett, “Modeling the dispersal of Cape hake ichthyoplankton”, *Journal of Plankton Research* **34**, 655–669 (2012) (cit. on p. 59).
- ⁵²L. Garavelli, F. Colas, P. Verley, D. M. Kaplan, B. Yannicelli, and C. Lett, “Influence of biological factors on connectivity patterns for *Concholepas concholepas* (loco) in Chile”, *PloS ONE* **11**, 1–22 (2016) (cit. on p. 59).
- ⁵³L. Garavelli, D. Kaplan, F. Colas, W. Stotz, B. Yannicelli, and C. Lett, “Identifying appropriate spatial scales for marine conservation and management using a larval dispersal model: the case of *Concholepas concholepas* (loco) in Chile”, *Progress in Oceanography* **124**, 42–53 (2014) (cit. on pp. 26, 38, 56, 58).
- ⁵⁴R. Gatignol, “The Faxén formulae for a rigid particle in an unsteady non-uniform Stokes flow”, *J. Mec. Theor. Appl.* **990**, 143–160 (1983) (cit. on pp. 21, 62, 66).
- ⁵⁵S. Goto and S. Kida, “Reynolds-number dependence of line and surface stretching in turbulence: folding effects”, *Journal of Fluid Mechanics* **586**, 59–81 (2007) (cit. on pp. 92, 97).
- ⁵⁶L. Guidi, G. A. Jackson, L. Stemmann, J. C. Miquel, M. Picheral, and G. Gorsky, “Relationship between particle size distribution and flux in the mesopelagic zone”, *Deep-Sea Research I* **55**, 1364–1374 (2008) (cit. on p. 63).
- ⁵⁷K. Guizien, M. Belharet, P. Marsaleix, and J. M. Guarini, “Using larval dispersal simulations for marine protected area design: application to the Gulf of Lions (Northwest Mediterranean)”, *Limnology and Oceanography* **57**, 1099 (2012) (cit. on pp. 26, 27).
- ⁵⁸K. Guseva, U. Feudel, A. Daitche, and T. Tél, “History effects in the sedimentation of light aerosols in turbulence: the case of marine snow”, *Phys. Rev. Fluids* **1**, 074203 (2016) (cit. on p. 22).
- ⁵⁹K. Guseva, U. Feudel, and T. Tél, “Influence of the history force on inertial particle advection: gravitational effects and horizontal diffusion”, *Phys. Rev. E* **88**, 042909 (2013) (cit. on pp. 22, 67, 69).
- ⁶⁰K. Gustavsson, S. Vajedi, and B. Mehlig, “Clustering of particles falling in a turbulent flow”, *Phys. Rev. Lett.* **112**, 214501 (2014) (cit. on p. 69).
- ⁶¹E. Gutknecht et al., “Coupled physical/biogeochemical modeling including O₂-dependent processes in the Eastern Boundary Upwelling Systems: application in the Benguela”, *Biogeosciences* **10**, 3559–3591 (2013) (cit. on p. 69).
- ⁶²D. B. Haidvogel et al., “Ocean forecasting in terrain-following coordinates: formulation and skill assessment of the regional ocean modeling system”, *Journal of Computational Physics* **227**, 3595–3624 (2008) (cit. on p. 11).
- ⁶³G. Haller, “Lagrangian coherent structures”, *Annual Review of Fluid Mechanics* **47**, 137–162 (2015) (cit. on pp. 15, 16).

- ⁶⁴G. Haller and T. Sapsis, “Where do inertial particles go in fluid flows?”, *Physica D: Nonlinear Phenomena* **237**, 573–583 (2008) (cit. on pp. 21, 23, 68).
- ⁶⁵G. Haller and G. Yuan, “Lagrangian coherent structures and mixing in two-dimensional turbulence”, *Physica D: Nonlinear Phenomena* **147**, 352–370 (2000) (cit. on p. 15).
- ⁶⁶C. S. Harrison, D. A. Siegel, and S. Mitarai, “Filamentation and eddy–eddy interactions in marine larval accumulation and transport”, *Marine Ecology Progress Series* **472**, 27–44 (2013) (cit. on p. 26).
- ⁶⁷J. I. Hedges, *Biogeochemistry of Marine Dissolved Organic Matter* (Elsevier, 2002), pp. 1–33 (cit. on p. 63).
- ⁶⁸S. A. Henson, R. Sanders, and E. Madsen, “Global patterns in efficiency of particulate organic carbon export and transfer to the deep ocean”, *Global Biogeochem. Cycles* **26**, GB1028 (2012) (cit. on p. 61).
- ⁶⁹I. Hernández-Carrasco, C. López, E. Hernández-García, and A. Turiel, “How reliable are finite-size Lyapunov exponents for the assessment of ocean dynamics?”, *Ocean Modelling* **36**, 208–218 (2011) (cit. on pp. 47, 58, 70, 83).
- ⁷⁰I. Hernández-Carrasco, V. Rossi, E. Hernández-García, V. Garçon, and C. López, “The reduction of plankton biomass induced by mesoscale stirring: a modeling study in the Benguela upwelling”, *Deep Sea Research Part I: Oceanographic Research Papers* **83**, 65–80 (2014) (cit. on pp. 89, 92, 97).
- ⁷¹M. Hidalgo, J. Tomas, J. Moranta, and B. Morales-Nin, “Intra-annual recruitment events of a shelf species around an island system in the NW Mediterranean”, *Estuarine Coastal and Shelf Science* **83**, 227–238 (2009) (cit. on pp. 33, 35).
- ⁷²M. Hidalgo et al., “Diffusion limit for the random walk metropolis algorithm out of stationarity”, to appear (cit. on p. 33).
- ⁷³M. A. Hixon, S. W. Pacala, and S. A. Sandin, “Population regulation: historical context and contemporary challenges of open vs. closed systems”, *Ecology* **83**, 1490–1508 (2002) (cit. on pp. 27, 35).
- ⁷⁴J. D. Hogan, R. J. Thiessen, P. F. Sale, and D. D. Heath, “Local retention, dispersal and fluctuating connectivity among populations of a coral reef fish”, *Oecologia* **168**, 61–71 (2012) (cit. on p. 28).
- ⁷⁵S. Honjo, “Biological pump and particle fluxes”, *Encyclopedia of Ocean Sciences*, 371–375 (2010) (cit. on p. 13).
- ⁷⁶J. Huggett, P. Freon, C. Mullon, and P. Penven, “Modelling the transport success of anchovy *Engraulis encrasicolus* eggs and larvae in the Southern Benguela: The effect of spatio-temporal spawning patterns”, *Marine Ecology-Progress Series* **250**, 247–262 (2003) (cit. on pp. 38, 55).
- ⁷⁷H. S. Huntley, B. L. Lipphardt, G. Jacobs, and A. D. Kirwan, “Clusters, deformation, and dilation: diagnostics for material accumulation regions”, *Journal of Geophysical Research: Oceans* **120**, 6622–6636 (2015) (cit. on p. 77).

- ⁷⁸M. Huret, P. Petitgas, and M. Woillez, “Dispersal kernels and their drivers captured with a hydrodynamic model and spatial indices: a case study on anchovy (*Engraulis encrasicolus*) early life stages in the Bay of Biscay”, *Progress In Oceanography* **87**, 6–17 (2010) (cit. on p. 38).
- ⁷⁹G. A. Jackson, “Effect of coagulation on a model planktonic food web”, *Deep Sea Research Part I: Oceanographic Research Papers* **48**, 95–123 (2001) (cit. on pp. 63, 65).
- ⁸⁰G. A. Jacobs, H. S. Huntley, A. D. Kirwan, B. L. Lipphardt, T. Campbell, T. Smith, K. Edwards, and B. Bartels, “Ocean processes underlying surface clustering”, *Journal of Geophysical Research: Oceans* **121**, 180–197 (2016) (cit. on p. 77).
- ⁸¹J. Jimenez, “Ocean turbulence at millimeter scales”, *Scientia Marina* **61**, 47–56 (1997) (cit. on pp. 4, 66).
- ⁸²G. P. Jones, M. Srinivasan, and G. R. Almany, “Population connectivity and conservation of marine biodiversity”, *Oceanography* **20**, 42–53 (2007) (cit. on p. 26).
- ⁸³A. N. Kolmogorov, “The local structure of turbulence in incompressible viscous fluid for very large Reynolds numbers”, *Proceedings of the Royal Society of London Series A* **434**, 9–13 (1991) (cit. on p. 4).
- ⁸⁴A. N. Kolmogorov, V. Levin, J. C. R. Hunt, O. M. Phillips, and D. Williams, “Dissipation of energy in the locally isotropic turbulence”, *Proceedings of the Royal Society of London. Series A: Mathematical and Physical Sciences* **434**, 15–17 (1991) (cit. on p. 4).
- ⁸⁵P. D. Komar, A. P. Morse, L. F. Small, and S. W. Fowler, “An analysis of sinking rates of natural copepod and euphausiid fecal pellets”, *Limnology and Oceanography* **26**, 172–180 (1981) (cit. on pp. 63, 64).
- ⁸⁶J. T. Kool, A. Moilanen, and E. A. Treml, “Population connectivity: recent advances and new perspectives”, *Landscape Ecology* **28**, 165–185 (2013) (cit. on p. 28).
- ⁸⁷J. T. Kool and S. L. Nichol, “Four-dimensional connectivity modelling with application to Australia’s north and northwest marine environments”, *Environmental Modelling & Software* **65**, 67–78 (2015) (cit. on pp. 38, 59).
- ⁸⁸J. T. Kool, C. B. Paris, P. H. Barber, and R. K. Cowen, “Connectivity and the development of population genetic structure in Indo-West Pacific coral reef communities”, *Global Ecology and Biogeography* **20**, 695–706 (2011) (cit. on p. 27).
- ⁸⁹A. S. Kough and C. B. Paris, “The influence of spawning periodicity on population connectivity”, *Coral Reefs* **34**, 753–757 (2015) (cit. on pp. 38, 39, 54).
- ⁹⁰D. E.S.S. T. Kyushu Univ., *Fluid dynamics for global environmental studies* (Springer, 2017) (cit. on p. 8).
- ⁹¹J. H. LaCasce and A. Bower, “Relative dispersion in the subsurface north Atlantic”, *Journal of Marine Research* **58**, 863–894 (2000) (cit. on p. 96).

- ⁹²G. Lacorata, E. Aurell, and A. Vulpiani, “Drifter dispersion in the adriatic sea: Lagrangian data and chaotic model”, *Annales Geophysicae* **19**, 121–129 (2001) (cit. on p. 17).
- ⁹³L. D. Landau and E. M. Lifshitz, *Fluid mechanics (second edition)* (Elsevier, 1987) (cit. on p. 20).
- ⁹⁴C. Lett, P. Verley, C. Mullon, C. Parada, T. Brochier, P. Penven, and B. Blanke, “A Lagrangian tool for modelling ichthyoplankton dynamics”, *Environmental Modelling & Software* **23**, 1210–1214 (2008) (cit. on p. 59).
- ⁹⁵G. Liu, A. Bracco, and U. Passow, “The influence of mesoscale and submesoscale circulation on sinking particles in the Northern Gulf of Mexico”, *Elementa, Science of the Anthropocene* **6**, 36 (2018) (cit. on pp. 79, 80, 84).
- ⁹⁶B. E. Logan and D. B. Wilkinson, “Fractal geometry of marine snow and other biological aggregates”, *Limnology and Oceanography* **35** (1990) (cit. on pp. 62, 74).
- ⁹⁷W. H. Lowe and F. W. Allendorf, “What can genetics tell us about population connectivity?”, *Molecular Ecology* **19**, 3038–3051 (2010) (cit. on p. 26).
- ⁹⁸E. MacPherson and N. Raventós, “Relationship between pelagic larval duration and geographic distribution in Mediterranean littoral fishes.”, *Marine Ecology Progress Series* **327**, 257–265 (2006) (cit. on p. 39).
- ⁹⁹F. Maggi, “The settling velocity of mineral, biomineral, and biological particles and aggregates in water”, *Journal of Geophysical Research: Oceans* **118**, 2118–2132 (2013) (cit. on p. 64).
- ¹⁰⁰F. Maggi and F. H. M. Tang, “Analysis of the effect of organic matter content on the architecture and sinking of sediment aggregates”, *Marine Geology* **363**, 102–111 (2015) (cit. on p. 64).
- ¹⁰¹A. Mahadevan, “Eddy effects on biogeochemistry”, *Nature* **506**, 168–169 (2014) (cit. on p. 26).
- ¹⁰²A. Mahadevan, J. Oliger, and R. Street, “A nonhydrostatic mesoscale ocean model. Part I: well-posedness and scaling”, *Journal of Physical Oceanography* **26**, 1868–1880 (1996) (cit. on p. 9).
- ¹⁰³A. Mancho, E. Hernandez-Garcia, D. Small, S. Wiggins, and V. Fernandez, “Lagrangian transport through an ocean front in the North-Western Mediterranean sea”, *Journal of Physical Oceanography* **38**, 1222–1237 (2008) (cit. on p. 26).
- ¹⁰⁴P. Mariani, B. R. MacKenzie, D. Iudicone, and A. Bozec, “Modelling retention and dispersion mechanisms of bluefin tuna eggs and larvae in the northwest Mediterranean sea”, *Progress in Oceanography* **86**, 45–58 (2010) (cit. on pp. 26, 58).
- ¹⁰⁵E. Massutí, S. Monserrat, P. Oliver, J. Moranta, J. López-Jurado, M. Marcos, M. Hidalgo, B. Guijarro, A. Carbonell, and P. Pereda, “The influence of oceanographic scenarios on the population dynamics of demersal resources in the Western Mediterranean: hypothesis for hake and red shrimp off Balearic Islands”, *Journal of Marine Systems*, 421–438 (2008) (cit. on p. 36).

- ¹⁰⁶M. R. Maxey, “The gravitational settling of aerosol particles in homogeneous turbulence and random flow fields”, **174**, 441–465 (1987) (cit. on pp. 20, 69, 72).
- ¹⁰⁷M. R. Maxey and J. J. Riley, “Equation of motion for a small rigid sphere in a nonuniform flow”, *Physics of Fluids* **26**, 883–889 (1983) (cit. on pp. 21, 22, 62, 66).
- ¹⁰⁸B. C. Mbaye, T. Brochier, V. Echevin, A. Lazar, M. Lévy, E. Mason, A. T. Gaye, and E. Machu, “Do *Sardinella aurita* spawning seasons match local retention patterns in the Senegalese Mauritanian upwelling region?”, *Fisheries Oceanography* **24**, 69–89 (2015) (cit. on pp. 26, 47, 49).
- ¹⁰⁹A. M. P. McDonnell and K. O. Buesseler, “Variability in the average sinking velocity of marine particles”, *Limnology and Oceanography* **55**, 2085–2096 (2010) (cit. on pp. 63, 65).
- ¹¹⁰V. L. Meccia, S. Simoncelli, and S. Sparnocchia, “Decadal variability of the Turner Angle in the Mediterranean Sea and its implications for double diffusion”, *Deep Sea Research Part I: Oceanographic Research Papers* **114**, 64–77 (2016) (cit. on p. 11).
- ¹¹¹E. E. Michaelides, “Hydrodynamic force and heat/mass transfer from particles, bubbles, and drops”, *Journal of Fluids Engineering* **125**, 209–238 (1997) (cit. on pp. 21, 22, 61, 62, 66, 69).
- ¹¹²S. Mitarai, D. Siegel, J. R. Watson, C. Dong, and J. C. McWilliams, “Quantifying connectivity in the coastal ocean with application to the Southern California Bight”, *Journal of Geophysical Research - Oceans* **114** (2009) (cit. on pp. 27, 38).
- ¹¹³J. G. Mitchell, H. H. Yamazaki, L. L. Seuront, F. Wolk, and H. Li, “Phytoplankton patch patterns: seascape anatomy in a turbulent ocean”, *Journal of Marine Systems* **69**, 247–253 (2008) (cit. on pp. 62, 74).
- ¹¹⁴P. Monroy, E. Hernández-García, R. V., and L. C., “Modeling the dynamical sinking of biogenic particles in oceanic flow”, *Nonlin. Processes Geophys.*, 293–305 (2017) (cit. on pp. 82, 84, 95, 111).
- ¹¹⁵S. Monserrat, J. L. Lopez-Jurado, and M. Marcos, “A mesoscale index to describe the regional circulation around the Balearic Islands”, *Journal of Marine Systems* **71**, 413–420 (2008) (cit. on pp. 33, 34).
- ¹¹⁶J. K. Moore and T. A. Villareal, “Size-ascent rate relationships in positively buoyant marine diatoms.”, *Limnology and Oceanography* **41** (1996) (cit. on p. 66).
- ¹¹⁷T. Nagata, H. Fukuda, R. Fukuda, and I. Koike, “Bacterioplankton distribution and production in deep Pacific waters: large scale geographic variations and possible coupling with sinking particle fluxes”, *Limnology and Oceanography* **45**, 426–435 (2000) (cit. on p. 79).
- ¹¹⁸Z. Neufeld and E. Hernández-García, *Chemical and biological processes in fluid flows* (Imperial College Press, 2009) (cit. on p. 1).
- ¹¹⁹M. E. J. Newman, *Networks: an introduction* (Oxford Univ. Press, 2010) (cit. on p. 30).

- ¹²⁰P. Oddo, M. Adani, N. Pinardi, C. Fratianni, M. Tonani, and D. Pettenuzzo, “A nested Atlantic-Mediterranean Sea general circulation model for operational forecasting”, *Ocean Science Discussions* **6**, 1093–1127 (2009) (cit. on p. 39).
- ¹²¹A. Okubo, “Oceanic diffusion diagram”, *Deep-Sea Research* **18**, 789–802 (1971) (cit. on pp. 66, 70, 83).
- ¹²²M. P. Olivar, G. Quilez, and M. Emelianov, “Spatial and temporal distribution and abundance of European hake, *Merluccius merluccius*, eggs and larvae in the Catalan Coast (NW Mediterranean)”, *Fish Research* **60**, 321–331 (2003) (cit. on p. 33).
- ¹²³S. Olivieri, F. Picano, G. Sardina, D. Iudicone, and L. Brandt, “The effect of the Basset history force on particle clustering in homogeneous and isotropic turbulence”, *Phys. Fluids* **26**, 041704 (2014) (cit. on p. 22).
- ¹²⁴V. I. Oseledets, “A multiplicative ergodic theorem. characteristic lypunov, exponents of dynamical systems”, *Transactions of the Moscow Mathematical Society* **19**, 197–231 (1968) (cit. on p. 17).
- ¹²⁵R. C. Pacanowski and S. G. H. Philander, “Parameterization of vertical mixing in numerical models of tropical oceans”, *Journal of Physical Oceanography* **11**, 1443–1451 (1981) (cit. on p. 11).
- ¹²⁶L. Palatella, F. Bignami, F. Falcini, G. Lacorata, S. A. Lanotte, and R. Santoleri, “Lagrangian simulations and the interannual variability of anchovy egg and larva dispersal in the Sicily Channel”, *J. Geophys. Res. Oceans* **119**, 1306–1323 (2014) (cit. on p. 70).
- ¹²⁷S. R. Palumbi, “Population genetics, demographic connectivity, and the design of marine reserves”, *Ecological Applications* **13**, 146–158 (2003) (cit. on p. 26).
- ¹²⁸C. Parada, C. van der Lingen, C. Mullon, and P. Penven, “Modelling the effect of buoyancy on the transport of anchovy (*Engraulis capensis*) eggs from spawning to nursery grounds in the southern Benguela: an IBM approach”, *Fisheries Oceanography* **12**, 170–184 (2003) (cit. on pp. 38, 59).
- ¹²⁹C. B. Paris, L. M. Chérubin, and R. K. Cowen, “Surfing, spinning, or diving from reef to reef: effects on population connectivity.”, *Marine Ecology Progress Series* **347**, 285–300 (2007) (cit. on p. 38).
- ¹³⁰C. B. Paris, J. Helgers, E. van Sebille, and A. Srinivasan, “Connectivity modeling system: a probabilistic modeling tool for the multi-scale tracking of biotic and abiotic variability in the ocean”, *Environmental Modelling and Software* **42**, 47–54 (2013) (cit. on p. 59).
- ¹³¹D. Pauli and V. Christensen, “Primary production required to sustain global fisheries”, *Nature* **374**, 255–257 (1995) (cit. on p. 12).
- ¹³²M. L. Pinsky, S. R. Palumbi, S. Andréfouët, and S. J. Purkis, “Open and closed seascapes: where does habitat patchiness create populations with high fractions of self-recruitment?”, *Ecological Applications* **22**, 1257–1267 (2012) (cit. on p. 27).

- ¹³³S. Planes, G. P. Jones, and S. R. Thorrold, “Larval dispersal connects fish populations in a network of marine protected areas”, *Proceedings of the National Academy of Sciences* **106**, 5693–5697 (2009) (cit. on p. 28).
- ¹³⁴P. M. Poulain and E. Zambianchi, “Surface circulation in the Central Mediterranean Sea as deduced from Lagrangian drifters in the 1990s”, *Continental Shelf Research* **27**, 981–1001 (2007) (cit. on p. 52).
- ¹³⁵A. Provenzale, “Transport by coherent barotropic vortices”, *Annual Review of Fluid Mechanics* **31**, 55–93 (1999) (cit. on pp. 62, 67).
- ¹³⁶H. R. Pulliam, “Sources, sinks, and population regulation”, *American Naturalist*, 652–661 (1988) (cit. on p. 27).
- ¹³⁷N. Putman and R. He, “Tracking the long-distance dispersal of marine organisms: sensitivity to ocean model resolution”, *Journal of the Royal Society Interface* **10** (2013) (cit. on pp. 38, 47, 58).
- ¹³⁸H. Qian, Y. Li, R. He, and D. B. Eggleston, “Connectivity in the intra-american seas and implications for potential larval transport”, *Coral Reefs* **34**, 403–417 (2015) (cit. on pp. 38, 49, 54).
- ¹³⁹X. Qin, E. van Sebille, and A. Sen Gupta, “Quantification of errors induced by temporal resolution on Lagrangian particles in an eddy-resolving model”, *Ocean Modelling* **76**, 20–30 (2014) (cit. on p. 58).
- ¹⁴⁰Z. Qiu, A. Doglioli, and F. Carlotti, “Using a Lagrangian model to estimate source regions of particles in sediment traps”, *Science China: Earth Sciences* **57**, 2447–2456 (2014) (cit. on p. 62).
- ¹⁴¹H. Queiroga, A. Dos-Santos, J. Dubert, I. Gonzalez-Gordillo, J. Paula, A. Peliz, and A. M. P. Santos, “Oceanographic and behavioural processes affecting invertebrate larval dispersal and supply in the Western Iberia Upwelling Ecosystem”, *Progress in Oceanography* **74**, 174–191 (2007) (cit. on pp. 38, 59).
- ¹⁴²P. Reglero, L. Ciannelli, D. Alvarez-Berastegui, R. Balbín, J. L. López-Jurado, and F. Alemany, “Geographically and environmentally driven spawning distributions of tuna species in the Western Mediterranean Sea”, *Marine Ecology Progress Series* **463**, 273–284 (2012) (cit. on p. 26).
- ¹⁴³O. Reynolds, “An experimental investigation of the circumstances which determine whether the motion of water shall be direct or sinuous, and of the law of resistance in parallel channels”, *Philosophical Transactions of the Royal Society of London* **174**, 935–982 (1883) (cit. on p. 2).
- ¹⁴⁴O. Reynolds, “IV. On the dynamical theory of incompressible viscous fluids and the determination of the criterion”, *Philosophical Transactions of the Royal Society of London. (A.)* **186**, 123–164 (1895) (cit. on p. 6).
- ¹⁴⁵L. F. Richardson, *Weather prediction by numerical process* (Cambridge University Press, 1922) (cit. on p. 4).

- ¹⁴⁶A. R. Robinson, J. J. McCarthy, and B. J. Rothschild, *The sea, biological-physical interactions in the sea (volume 12)* (Wiley, 2002) (cit. on p. 8).
- ¹⁴⁷V. Rossi, C. López, J. Sudre, Hernández-García, and V. Garçon, “Comparative study of mixing and biological activity of the Benguela and Canary upwelling systems”, *Geo. Phys. Let.* **35**, L11602 (2008) (cit. on pp. 26, 97).
- ¹⁴⁸V. Rossi, E. Ser-Giacomi, C. López, and E. Hernández-García, “Hydrodynamic provinces and oceanic connectivity from a transport network help designing marine reserves”, *Geophysical Research Letters* **41**, 2883–2891 (2014) (cit. on pp. 26–28, 30, 39, 43, 56).
- ¹⁴⁹V. Rossi, E. Van Sebille, E. Sen Gupta, V. Garçon, and M. H. England, “Multi-decadal projections of the surface and interior pathways of the Fukushima Cesium-137 radioactive plume”, *Deep Sea-Research I* **80**, 37–46 (2013) (cit. on pp. 26, 70, 83).
- ¹⁵⁰F. Roullier, L. Berline, L. Guidi, X. Durrieu De Madron, M. Picheral, A. Sciandra, S. Pesant, and L. Stemmann, “Particle size distribution and estimated carbon flux across the Arabian Sea oxygen minimum zone”, *Biogeosciences* **11**, 4541–4557 (2014) (cit. on pp. 62, 74).
- ¹⁵¹J. Ruiz, D. Macias, and F. Peters, “Turbulence increases the average settling velocity of phytoplankton cells”, *Proceedings of the National Academy of Sciences* **101**, 17720–17724 (2004) (cit. on p. 72).
- ¹⁵²C. L. Sabine et al., “The oceanic sink for anthropogenic CO₂”, *Science* **305**, 367–371 (2004) (cit. on pp. 61, 79).
- ¹⁵³R. Salmon, *Lectures on geophysical fluid dynamics* (Oxford University Press, 1998) (cit. on p. 2).
- ¹⁵⁴M. Sandulescu, E. Hernández-García, C. López, and U. Feudel, “Kinematic studies of transport across an island wake, with application to the Canary Islands”, *Tellus A: Dynamic Meteorology and Oceanography* **58**, 605–615 (2006) (cit. on p. 83).
- ¹⁵⁵T. Sapsis and G. Haller, “Inertial particle dynamics in a hurricane”, *Journal of the Atmospheric Sciences* **66**, 2481–2492 (2009) (cit. on pp. 67, 100).
- ¹⁵⁶E. van Sebille, P. Scussolini, J. V. Durgadoo, F. Peeters, A. Biastoch, W. Weijer, C. S. M. Turney, C. B. Paris, and R. Zahn, “Ocean currents generate large footprints in marine palaeoclimate proxies”, *Nature communications* **6**, 6521 (2015) (cit. on pp. 62, 79).
- ¹⁵⁷E. Ser-Giacomi, “A complex network theory approach to oceanic and atmospheric transport phenomena”, PhD thesis (2015) (cit. on p. 19).
- ¹⁵⁸E. Ser-Giacomi, V. Rossi, C. Lopez, and E. Hernandez-Garcia, “Flow networks: a characterization of geophysical fluid transport”, *Chaos* **25**, 036404 (2015) (cit. on pp. 28, 29, 39, 40, 47, 58).
- ¹⁵⁹E. Ser-Giacomi, V. Rossi, C. López, and E. Hernández-García, “Flow networks: a characterization of geophysical fluid transport”, *Chaos: An Interdisciplinary Journal of Nonlinear Science* **25**, 036404 (2015) (cit. on pp. 18, 30, 84).

- ¹⁶⁰S. C. Shadden, F. Lekien, and J. E. Marsden, “Definition and properties of Lagrangian coherent structures from finite-time Lyapunov exponents in two-dimensional aperiodic flows”, *Physica D: Nonlinear Phenomena* **212**, 271–304 (2005) (cit. on p. 17).
- ¹⁶¹A. L. Shanks, “Pelagic larval duration and dispersal distance revisited”, *The Biological Bulletin* **216**, 373–385 (2009) (cit. on p. 43).
- ¹⁶²A. F. Shchepetkin and J. C. C. McWilliams, “The regional oceanic modeling system (ROMS): a split-explicit, free-surface, topography-following-coordinate ocean model”, *Ocean Modelling* **9**, 347–404 (2005) (cit. on p. 11).
- ¹⁶³D. A. Siegel and W. G. Deuser, “Trajectories of sinking particles in the Sargasso Sea: modeling of statistical funnels above deep-ocean sediment traps”, *Deep-Sea Research Part I-Oceanographic Research Papers* **44**, 1519–1541 (1997) (cit. on pp. 62, 69, 74, 79, 97).
- ¹⁶⁴D. A. Siegel, E. Fields, and K. O. Buesseler, “A bottom-up view of the biological pump: modeling source funnels above ocean sediment traps”, *Deep-Sea Research I* **55**, 108–127 (2008) (cit. on pp. 62, 74).
- ¹⁶⁵M. Simon, H. Grossart, B. Schweitzer, and H. Ploug, “Microbial ecology of organic aggregates in aquatic ecosystems”, *Aquatic Microbial Ecology* **28**, 175–211 (2002) (cit. on pp. 64, 65).
- ¹⁶⁶R. D. Simons, D. A. Siegel, and K. S. Brown, “Model sensitivity and robustness in the estimation of larval transport: a study of particle tracking parameters”, *Journal of Marine Systems* **119–120**, 19–29 (2013) (cit. on pp. 38, 39, 42, 46, 57, 58).
- ¹⁶⁷R. E. Snyder, C. B. Paris, and A. C. Vaz, “How much do marine connectivity fluctuations matter?”, *The American Naturalist* **184**, 523–530 (2014) (cit. on p. 55).
- ¹⁶⁸A. Sozza, F. De Lillo, S. Musacchio, and G. Boffetta, “Large-scale confinement and small-scale clustering of floating particles in stratified turbulence”, *Phys. Rev. Fluids* **1**, 05240 (2016) (cit. on p. 66).
- ¹⁶⁹K. D. Squires and J. K. Eaton, “Preferential concentration of particles by turbulence”, *Physics of Fluids A* **3**, 1169–1178 (1991) (cit. on pp. 62, 69, 75).
- ¹⁷⁰L. Stemmann and E. Boss, “Plankton and particle size and packaging: from determining optical properties to driving the biological pump”, *Annual Review of Marine Science* **4**, 263–90 (2012) (cit. on pp. 63, 65).
- ¹⁷¹S. Sundby and T. Kristiansen, “The principles of buoyancy in marine fish eggs and their vertical distributions across the world oceans”, *PLoS ONE* **10**, e0138821 (2015) (cit. on p. 58).
- ¹⁷²W. Tang, B. Knutson, A. Mahalov, and R. Dimitrova, “The geometry of inertial particle mixing in urban flows, from deterministic and random displacement models”, *Physics of Fluids* **24** (2012) (cit. on p. 70).
- ¹⁷³P. Tanga, A. Babiano, B. Dubrulle, and A. Provenzale, “Forming Planetesimals in Vortices”, *Icarus* **121**, 158–170 (1996) (cit. on pp. 67, 69).

- ¹⁷⁴G. I. Taylor, “Diffusion continuous movements”, Proceedings of The London Mathematical Society **20**, 196–212 (1922) (cit. on p. 51).
- ¹⁷⁵R. Toral and P. Colet, *Stochastic numerical methods: an introduction for students and scientists* (John Wiley & Sons, 2014) (cit. on p. 70).
- ¹⁷⁶A. P. Torres, P. Reglero, R. Balbin, A. Urtizberea, and F. Alemany, “Coexistence of larvae of tuna species and other fish in the surface mixed layer in the NW Mediterranean”, Journal of Plankton Research **33**, 1793–1812 (2011) (cit. on p. 58).
- ¹⁷⁷E. A. Treml, J. J. Roberts, Y. Chao, P. N. Halpin, H. P. Possingham, and C. Riginos, “Reproductive output and duration of the pelagic larval stage determine seascape-wide connectivity of marine populations”, Integrative and Comparative Biology **52**, 525–537 (2012) (cit. on pp. 27, 38).
- ¹⁷⁸G. K. Vallis, *Atmospheric and oceanic fluid dynamics: fundamentals and large-scale circulation*, first edition (Cambridge University Press, 2006) (cit. on pp. 2, 8, 11).
- ¹⁷⁹A. Vaz, K. Richards, Y. Jia, and C. Paris, “Mesoscale flow variability and its impact on connectivity for the island of Hawaii”, Geophysical Research Letters **40**, 332–337 (2013) (cit. on p. 26).
- ¹⁸⁰L. Wang and M. R. Maxey, “Settling velocity and concentration distribution of heavy particles in homogeneous isotropic turbulence”, Journal of Fluid Mechanics **256**, 27–68 (1993) (cit. on p. 72).
- ¹⁸¹J. Waniek, W. Koeve, and R. D. Prien, “Trajectories of sinking particles and the catchment areas above sediment traps in the northeast Atlantic”, Journal of Marine Research **58**, 983–1006 (2000) (cit. on p. 79).
- ¹⁸²S. Wiggins, *Chaotic transport in dynamical systems* (Springer, 1992) (cit. on p. 15).
- ¹⁸³S. Wood, C. Paris, A. Ridgwell, and E. J. Hendy, “Modelling dispersal and connectivity of broadcast spawning corals at the global scale”, Global Ecology and Biogeography **23**, 1–11 (2014) (cit. on pp. 27, 38).
- ¹⁸⁴N. M. J. Woodhouse, *Introduction to analytical dynamics* (Oxford University Press, 1987) (cit. on p. 103).
- ¹⁸⁵F. d’Ortenzio and M. R. d’Alcalá, “On the trophic regimes of the Mediterranean Sea: a satellite analysis”, Biogeosciences **6**, 1–10 (2009) (cit. on p. 26).
- ¹⁸⁶F. d’Ortenzio, D. Iudicone, C. de Boyer Montegut, P. Testor, D. Antoine, S. Marullo, R. Santoleri, and G. Madec, “Seasonal variability of the mixed layer depth in the Mediterranean Sea as derived from in situ profiles”, Geophysical Research Letters **32**, L12605 (2005) (cit. on p. 58).